A 2D ACROSS-THE-CHANNEL MODEL OF A POLYMER ELECTROLYTE MEMBRANE FUEL CELL: WATER TRANSPORT AND POWER CONSUMPTION IN THE MEMBRANE

A Thesis Submitted to the

College of Graduate Studies and Research

in Partial Fulfillment of the Requirements for the Degree of

Master of Science

in the

Department of Chemical Engineering

University of Saskatchewan

Saskatoon, Canada

By

Venkateshwar Rao Devulapalli

PERMISSION TO USE

In presenting this thesis in partial fulfillment of the requirements for a Post graduate degree from the University of Saskatchewan, I agree that the Libraries of this University may make it freely available for inspection. I further agree that permission for copying of this thesis in any manner, in whole or in part, for scholarly purposes may be granted by the professor or professors who supervised my thesis work or, in their absence, by the Head of the Department or the Dean of the College in which my thesis work was done. It is understood that any copying, publication, or use of this thesis or parts thereof for financial gain shall not be allowed with out my written permission. It is also understood that due recognition shall be given to me and to the University of Saskatchewan in any scholarly use which may be made of any material in my thesis.

Requests for permission to copy or to make other use of material in this thesis in whole or part should be addressed to:

Head of the Department of Chemical Engineering

University of Saskatchewan

Saskatoon, Saskatchewan S7N 5A9

Canada

ABSTRACT

The anisotropic mass transport issues inside a fuel cell membrane have been studied in this thesis using computer modelling. The polymer electrolyte membrane (PEM) conductivity of a PEM fuel cell (PEMFC) depends on the hydration state of the hydrophilic charged sites distributed in the pores of the membrane. Water humidification of these charged sites is crucial for sustaining the membrane conductivity and reducing concerning voltage losses of the cell. During the operation of a PEMFC, the transport of humidified inlet gases (fuel/oxidant) is influenced by external design factors such as flow field plate geometry of the gas circulating channels. As a result, there arises a distribution in the mass transport of water inside the membrane electrode assembly. A two-dimensional, cross-the-channel, fuel cell membrane layer mass transport model, developed in this work, helps the study of the impact of factors causing the distribution in the membrane ionic conductivity on ohmic losses.

The governing equations of the membrane mathematical model stem from the multicomponent framework of concentrated solution theory. All mass transport driving forces within the vapour and/or liquid equilibrated phases have been accounted in this research. A computational model, based on the finite control volume method, has been implemented using a line-by-line approach for solving the dependent variables of the mass transport equations in the two-dimensional membrane domain. The required boundary conditions for performing the anisotropic mass transport analysis have been obtained from a detailed agglomerate model of the cathode catalyst layer available in the literature.

The results obtained using boundary conditions with various flow field plate channel-land configurations revealed that the anisotropic water transport in the cathode half-cell severely affects the ohmic losses within the membrane. A partially humidified vapour equilibrated membrane simulation results show that a smaller channel-land ratio (1:1) sustains a better membrane performance compared to that with a larger one (2:1 or 4:1). Resistance calculations using the computer model revealed that ohmic losses across the membrane also depend on its physical parameters such as thickness. It was observed that the resistance offered by a thinner membrane towards vapour phase mass transport is comparatively lower than that offered by a thicker membrane. A further analysis accounting the practical aspects such as membrane swelling constraints, imposed by design limitations of a fuel cell, revealed that the membrane water content and ionic conductivity are altered with an increase in the compression constraint effects acting upon a free swelling membrane.

ACKNOWLEDGEMENTS

I would like to express my appreciation and sincere gratitude to my supervisor, Dr. Aaron Phoenix, for his guidance, support and encouragement throughout my graduate programme. I am grateful to him for the opportunity given to work in the field of fuel cells. His time and help in writing this thesis are also greatly appreciated.

I would like to thank my advisory committee members Dr. Richard Evitts and Dr. Mehdi Nemati for their valuable suggestions and inputs.

I thank Dr. Kunal Karan and Wei Sun of Queen's-RMC Fuel cell research centre for providing some necessary data required in this work.

I take this opportunity to thank my friends, colleagues and non academic staff at the Department of Chemical Engineering, the University of Saskatchewan for making my stay, a very good experience.

Additionally, I thank Dr. Phoenix and NSERC Canada for providing the financial support for this work.

Dedicated to my parents and brother

For their guidance, support and motivation.

Also, to my dachshund, *Marshall*.

TABLE OF CONTENTS

LIST OF FIGURES

LIST OF TABLES

LIST OF SYMBOLS

Roman Letters

a	Activity of water vapour
A	Area of the active surface [cm^2]
c_i	Concentration of species i (H_2, O_2 & H_2O) [mol/cm^3]
$\mathscr{D}_{ij}$	The binary diffusion interaction coefficient in the PEM phase [cm^2/s]
D_{μ_o}	Diffusion coefficient of water in membrane [cm^2/s]
d_i	Driving force for transport of species i [J/cm^4]
$E^*_{o,k}$	The binary interaction parameter between water and species k [g/mol]
EW	Equivalent weight of the membrane [g/equiv]
f	Water volume fraction of the membrane
F	Faraday constant, 96487 [C/mol]
h	Channel width [cm]
$\mathbf{i}$	Protonic current density [A/cm^2]
k	Effective permeability [cm^2]
k_{sat}	Membrane absolute permeability [cm^2]
K_{ij}	Frictional coefficient of interaction [$J \cdot s/cm^5$]
K	Bulk modulus [bar]
K_e	Equilibrium constant
l	Membrane thickness [cm]
L_{ij}	Inverted frictional coefficient of interaction [$cm^5/J \cdot s$]
M_m	Equivalent weight of the membrane [g/mol]
m_k	Molality of species k in the membrane [mol/g]
$\mathbf{N}_i$	Molar flux of species i [$mol/cm^2 \cdot s$]
n_i	Number of species in phase i
p	Pressure [bar]

p_0^{vap} Vapour pressure of water [bar]

p_L Hydraulic pressure of liquid water [bar]

r Membrane resistivity (1/conductivity) [$\Omega \cdot \text{cm}$]

r_c Critical radius of pore [nm]

r_V The ratio of molar volumes of polymer and solvent

R Universal gas constant, 8.314 [J/mol·K]

R_i Homogeneous rate of reaction [mol/cm^3·s]

R_m Membrane resistance [$\Omega \cdot \text{cm}^2$]

S Fraction of expanded channels

t Time [s]

T Temperature [° K]

T_{ref} Reference temperature, 303.15 [° K]

v_i Velocity of species *i* [cm/s]

V Volume of membrane [cm^3]

$\overline{V_i}$ Partial molar volume of species *i* [cm^3/mol]

x_i Mole fraction of species *i*

Y Young's modulus [bar]

Greek Letters

α Transport coefficient [mol^2/J·cm·s]

β Net water flux per proton flux

γ Surface tension [N/cm]

χ Magnitude of constraint

χ_F Flory interaction parameter

κ Membrane ionic conductivity [S/cm]

ξ Electro-osmotic drag coefficient

θ Contact angle in degrees

ϕ_2 The volume fraction of the membrane-water system

λ Membrane water content [dimensionless]

λ_c The bound water content in the hydronium ion complex

λ_L Membrane water content of a liquid saturated membrane

$\lambda_{V,act=1}$ Membrane water vapour content at unit activity

$\hat{\lambda}$ Average water content

μ Viscosity [bar·s]

μ_0 Electrochemical potential of species *i* [J/mol]

μ_o^* A combination of reference states and constants

ρ_m Density of dry membrane/water system [g/cm^3]

ρ Density of species [g/cm^3]

τ Dilatation stress parameter [bar]

Φ Protonic potential in the PEM phase [V]

Φ_s Electric Potential in the solid phase [V]

Subscripts

a Anode

c Cathode

g Gas phase

m Membrane

L Liquid equilibrated membrane

V Vapour equilibrated membrane

0 Water

+ Proton

Matrices

L Matrix of inverted frictional coefficients

M Matrix of frictional coefficients

LIST OF ABBREVIATIONS

PEMFC: Proton Exchange/Polymer Electrolyte Membrane Fuel Cell

PEM: Polymer Electrolyte Membrane

PFSA: Perfluorosulfonic acid

PTL: Porous Transport Layer

CCM: Catalyst Coated Membrane

MEA: Membrane Electrode Assembly

HOR: Hydrogen Oxidation Reaction

ORR: Oxygen Reduction Reaction

CL: Catalyst Layer

PTFE: Poly-Tetra-Fluoro-Ethlylene

EW: Equivalent Weight

NCO: Nominal Cathode Overpotential

RHS: Right Hand Side

LHS: Left Hand Side

1. INTRODUCTION

1.1 Background

The significant rise in the emission levels of greenhouse gases and air pollutants can be attributed to the inefficiencies of and the growing number of power generating systems. It is estimated that one-fourth of the world's human generated green house gases are emitted from gasoline combustion in transportation applications (Thomas *et al.*, 1999). These gases change the composition of the stratosphere which may lead to global warming. Further, the increasing global energy consumption rate and the depleting natural reserves of fossil fuels are escalating the cost of fuels. These factors have urged the development of efficient, non-conventional and zero emission energy conversion systems. One such technological breakthrough, promising the green energy features, was the emergence of a hydrogen-oxygen proton exchange membrane fuel cell (PEMFC).

A fuel cell is an electrochemical device that converts chemical energy into electrical energy by combining fuel and oxidant. Although, the first fuel cell was invented by Sir William Grove in 1839, the first fuel cell application was found in NASA's Gemini space flights in the 1960s. Since then, fuel cells have undergone a series of developments and have evolved into different types, which mainly serve as electrical power generators. It is only recently that fuel cells have gained the interest of energy firms and automobile giants as a feasible energy source and they are

believed to have a great potential for successfully replacing the conventional fossil fuel driven internal combustion engines for futures automobiles and stationary power generators (Perry *et al.*, 2002).

Based on the type of electrolyte and the fuel used, fuel cells are characterised into different types. In principal, the operating conditions also vary widely between different fuel cells types. These devices are primarily designated for use in a specific type of application such as vehicular transportation, stationary power generation, space application and mobile electronic power source. Table 1.1 classifies different types of fuel cells based on their characteristics. Though the zero-emission nature of PEMFCs strictly holds true from a fuel cell operational perspective, the fuel cell systems integrated with applications are entirely not emission-free; there will always be some emissions that arise during fuel production such as steam reforming of natural gas. Irrespective of emissions from fuel production techniques, PEMFCs are still favoured for their compactness and simple architecture of energy conversion (by fuel oxidation and oxidant reduction) and are proclaimed to be a best available alternative to fossil fuel driven internal combustion engines for automobiles (Fontes *et al.*, 2001). The essential reasons behind the success of PEMFCs as an energy provider are their ability to start quickly at low temperatures, simplicity, and good efficiency under normal operating conditions.

Table 1.1: Types of fuel cells (Wendt *et al.*, 1999; Carrette *et al.*, 2001; Spakovsky *et al.*, 2002; Laughton, 2002)

Fuel Cell Type	Electrolyte	Fuel	Charge Carrier	Operating Temperature (°C)	Realised Power (kW)	Electrical Efficiency* (%)	Start-Up Time
Alkaline (AFC)	KOH	Pure H_2	OH^-	60-120	5-150	35-55	min
Proton Exchange Membrane (PEMFC)	Solid Polymer†	Pure H_2 (Tolerates CO_2)	H^+	70-100	5-250	40-45	sec-min
Direct Methanol (DMFC)	Solid Polymer†	CH_3OH, H_2O	H^+	~ 90	5	30-35	
Solid Oxide (SOFC)	Solid Oxide	H_2, CO, CH_4 (Tolerates CO_2)	O^{2-}	~ 1000	100-250	50-60	hrs
Molten Carbonate(MCFC)	Lithium and Potassium Carbonate	H_2, CO, CH_4 (Tolerates CO_2)	CO_3^{2-}	600-700	100-2000	50-60	
Phosphoric Acid (PAFC)	Phosphoric Acid	Pure H_2 (Tolerates CO_2, approx 1 % CO)	H^+	150-220	50-11000	40-45	

* Electrical Efficiency, $\eta_{eff} = \frac{\text{max. electrical work done}}{\text{enthalpy of formation}} = \frac{W_{elec,\max}}{\Delta H_f} \times 100$

† Hydrated during the cell operation

1.2 Design and Operation of a PEM Fuel Cell

The PEM fuel cell is made up of an anode catalyst layer and a cathode catalyst layer that are separated by a polymer electrolyte membrane (PEM), often made of a perfluorosulfonic acid (PFSA) polymer such as Nafion® or Aciplex®. The membrane is a good conductor of protons when it is in a hydrated state. The catalyst coated membrane (CCM) is sandwiched between two porous transport layers (PTLs) to form the membrane electrode assembly (MEA). The PTLs are often carbon based paper or fabric doped with a hydrophobic polymer. Each of the individual components of the MEA plays a vital role in the operation of a PEMFC. The MEA is enclosed on either side by the flow field plates that help in the circulation of inlet gases (fuel and oxidant), and electron conduction and product removal.

In a PEMFC, the anode half-cell reaction is the hydrogen oxidation reaction (HOR) and the cathode half-cell reaction is the oxygen reduction reaction (ORR):

Anode half-cell (HOR): $H_2 \rightleftharpoons 2H^+ + 2e^-$ (1.1)

Cathode half-cell (ORR): $\frac{1}{2}O_2 + 2H^+ + 2e^- \rightleftharpoons H_2O$ (1.2)

Overall reaction: $H_2 + \frac{1}{2}O_2 \rightleftharpoons H_2O$ (1.3)

The anode and cathode half-cell reactions occur on the active catalyst active layers. The catalyst layers at the membrane - PTL interfaces in Figure 1.1 consists of dispersed polymer electrolyte coated spherical agglomerates. Each of these agglomerates is composed of a cluster of carbon particles that are embedded with

platinum on their surface (Sun *et al.*, 2005a). Such a type of catalyst structure provides proper conduction of both protons (on the polymer electrolyte coating) and electrons (on carbon particles). Platinum loadings on the surface of the carbon particles equal 0.4 mg/cm^2 or lower (Costamagna *et al.*, 2001).

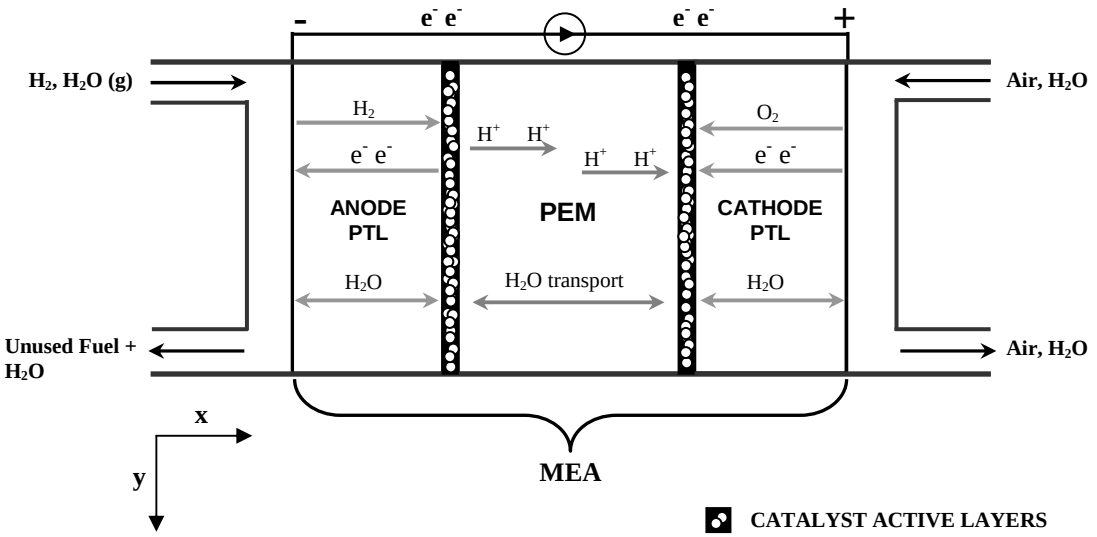

Figure 1.1: Description of a PEM fuel cell

A typical PEMFC operates in the range of 70-100°C. Figure 1.1 shows an operating fuel cell where humidified gases (hydrogen and oxygen) are supplied to the electrodes on either sides of the PEM through gas channels. Hydrogen flows through the anode gas channel to the anode porous transport layer (PTL) where it diffuses toward the platinum catalyst layer (CL). Platinum in the anode catalyst active layer promotes hydrogen separation into protons and electrons. Because of the uniform distribution of negatively charged sites in the PEM, it only allows protons to flow through it and acts as a separator of protons and electrons. On the opposite side of the PEM, air flows through the cathode gas channel to the cathode PTL where oxygen

from the air diffuses towards cathode active layer. Based the protonic potential gradient between the cathode and anode and the hydration state of the PEM, protons travel through the PEM (from anode CL) to the cathode active layer and react with oxygen molecules and electrons returning from the external circuit. Meanwhile, electrons flowing through the external circuit from anode to cathode are essentially captured as current at required voltage. The main product of ORR at the cathode CL is water, whereas electricity and heat can be called utility-products of the overall electrochemical reaction inside the PEMFC (Larminie *et al.*, 2000; Costamagna *et al.*, 2001).

1.3 Thermodynamics of a PEMFC

The theoretical cell voltage can be calculated based on the number of moles of charge transferred and the change in Gibbs free energy of formation for the overall electrochemical reaction. The standard reduction potential E^0 of the ORR based on the change in Gibbs free energy of formation (Larminie *et al.* 2000) can be expressed in terms of electric potential as

$$\Delta G_f^0 = -nFE^0, \tag{1.4}$$

where

G_f^0 = Gibbs free energy of formation [J/mol] at reference conditions,

n = number of moles of charge dissociated,

F = Faraday constant, 96487 [C/mol], and

E^0 = the standard reversible potential of ORR reaction [V].

The change in Gibbs free energy of formation varies with the inlet feed activities, temperature and the form of product water (vapour or liquid). Considering these factors, the reversible potential of a fuel cell E_R at given activities of the reactant and product can be calculated using Nernst's equation which expresses the electric potential in terms of the standard reduction potential of the ORR at the cathode active layer and the logarithmic of the ratio of the activities of the reactants to the products. Utilizing equation (1.4), the ORR reduction potential at a desired inlet reactant activity and temperature can be expressed as

$$E_R = E^0 + \frac{RT}{2F}\ln\left[\frac{a_{H_2} a_{O_2}^{1/2}}{a_{H_2O}}\right], \qquad (1.5)$$

where

E_R = the reversible cell voltage [V],

R = universal gas constant [J/mol],

T = the cell temperature [K], and

a_i = activity of species $i = \dfrac{\text{partial pressure of species } i}{\text{standard pressure}} = \dfrac{p_i}{P^0}$.

1.4 Voltage Deviations across a PEMFC

During the operation of a PEM fuel cell, several factors contribute to the total voltage deviation from the reversible cell potential. The voltage loss leads to the polarization of the fuel cell performance. The deviation in the cell potential from reversible cell potential is called overpotential. As a whole, the losses in fuel cell voltage occur across the layers of the MEA and are categorized as activation, ohmic and concentration overpotentials (Berger, 1968; Hoogers, 2003). The operating fuel

cell voltage can be obtained by subtracting these voltage losses from the reversible cell potential given in equation (1.5).

The activation overpotential is a result of electrochemical reaction kinetic limitations at the catalyst active layers. As the hydrogen oxidation reaction (HOR) at the anode active layer is sufficiently fast, it contributes less towards the total cell potential deviation (Hoogers, 2003). It is clear from Figure 1.2 that cathode activation potential results in a major voltage deviation, the significance of which can be attributed to the sluggish kinetics of oxygen reduction reaction (ORR). Nonetheless, the activation overpotential is not the focus of this thesis but further details of which can be found in Berger, (1968) and Newman *et al.* (2004).

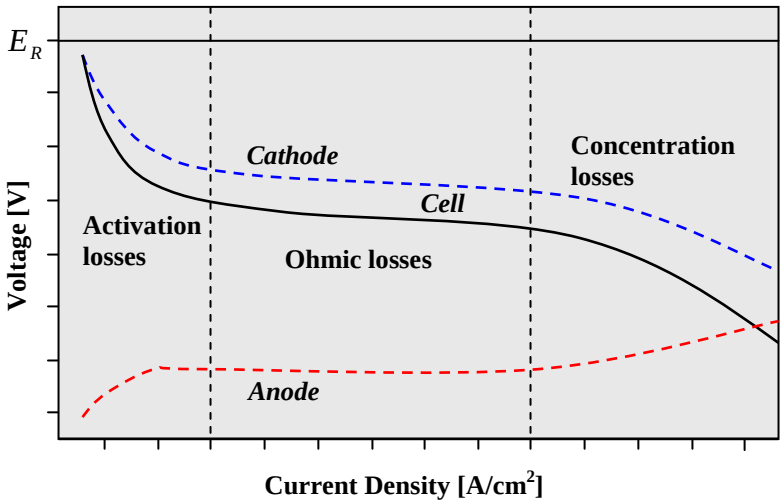

Figure 1.2: Schematic of fuel cell polarization curve (Carrette *et al.*, 2001)

Ohmic overpotential occurs because of the resistive nature of the charge conducting media of a fuel cell, this is represented by mid portion of the cell polarization curve in Figure 1.2. These resistances, in-part, can be attributed to the improper design of the MEA components. A poor design of the flow field plates could

increase the contact resistances towards electron conduction at the electrodes. On the other had, the losses across the membrane arise from the inherent resistive nature towards proton conduction. These depend on the thickness of the membrane (Berger, 1968) and the extent of humidification of the hydrophilic charged sites. The iR drop across the fuel cell is shown using Ohm's law in equation (1.7).

$$\eta_{ohmic} = \mathbf{i}R_{cell} \tag{1.7}$$

The concentration (or mass transfer) losses result because of the inefficient transport of reactants towards the active layers. The critical factors influencing these losses are the insufficient humidification of the PEM and water flooding at the cathode active layer. The insufficient hydration of the PEM leads to the loss of proton conduction and hampers the net charge concentration at the surface of the active layer. The higher liquid water concentrations at the PEM-cathode PTL block the oxygen diffusion towards the reactive surface. Accounting these voltage losses is also crucial for estimating the performance of a fuel cell. Further details of the theory associated with predicting these losses can be found in Larminie *et al.* (2000).

1.5 General Factors Governing the Functioning of PEMFCs

Though PEMFCs are proclaimed to be on the edge of becoming promising sources for achieving future's power requirements and green energy goals, there are still some technological constraints that are restraining these energy converters from becoming a commercial success. The kinetics of the cathode half-cell reaction limits the performance of the cell. The factors relating to PEM water and thermal

management critically affect for cell functioning. These factors, in essence, affect the efficiency and durability of the PEMFC.

Effective water management in the MEA is vital in achieving the desired cell efficiency. The ion transportation paths in the PEM are hydrophilic and their effectiveness is highly dependent on wetting by humidifying agents. Hence, during the operation of a fuel cell, the reactant gases are humidified so as to reduce the local resistances toward ion transport in the membrane. The ion conductive resistances, which if not reduced, will inhibit the protonic transport across the membrane and hamper the overall performance of the fuel cell. Also at high current densities, the proton induced water drag from anode to cathode could exceed the back diffusion or convection of water from the cathode to the anode. This process leads to the dehydration of the membrane (Fuller *et al.*, 1992), which leads to severe losses in proton conductivity. The water balance across the membrane also plays critical role in efficient operation of the cell. A high net water flux across the membrane blocks the flow of reactant at the cathode active layer and this leads to mass transfer losses. This should be avoided by balancing the water fluxes induced by various driving forces of mass transport (such as proton induced water drag, diffusion or convection).

Another factor that could significantly affect the mass transport is the architecture of the MEA in a fuel cell. It can be seen in Figure 1.3 that channel to land (area of PTL under the land) variations of the flow field plates do not allow for the uniform distribution of inlet gases and cause the anisotropy in water distribution at the membrane-cathode PTL interface. At the same time, water discharge from the concentrated portions under the land becomes critical. These effects of anisotropy in

mass transport lead to deviations in the local reaction profile along the membrane-catalyst layer interfaces and also affect the water dependent membrane transport properties such as ionic conductivity in the PEM phase (West *et al.*, 1996; Sun *et al.*, 2005b).

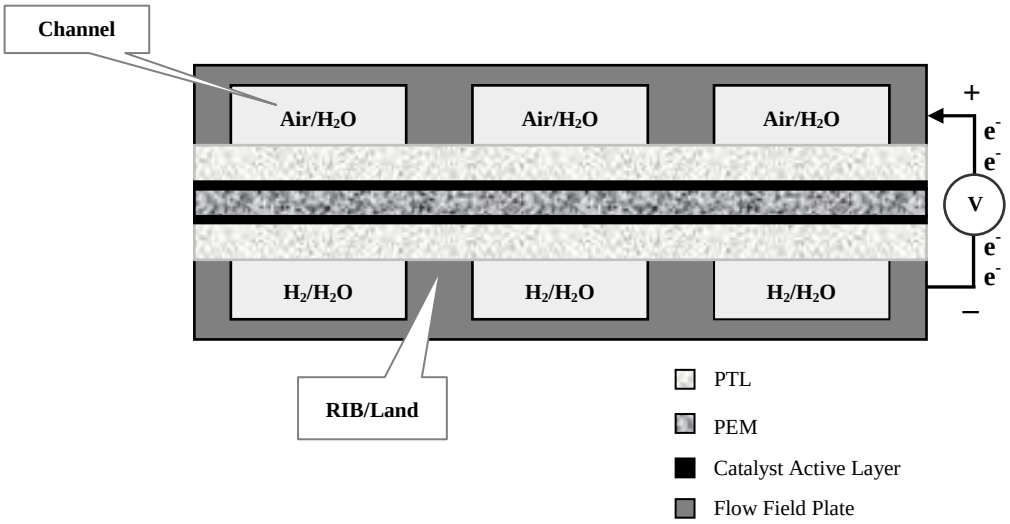

Figure 1.3: A cross-section of a unit cell

The physico-chemical properties of the MEA also influence the mass transport. Water dependent membrane transport properties, which vary with the hydration state and temperature, play a crucial role in driving the transport of protons and water across the membrane. The ion conducting nature of the PEM varies widely between a membrane hydrated with water vapour and the one with liquid water. This can be ascribed to the membrane structural evolution in the presence of polar solvent and the innate proton transfer mechanisms. Assessing these factors properly is important for achieving a desired cell performance because in reality PEMFCs are operated with gases that are humidified between the extremes of dry and liquid saturated states (Mathias *et al.*, 2005).

From a reliability point of view, aspects of the membrane hydration and dehydration cycles (during the cell start-up and termination) lead to its swelling and contraction and vice versa. It was pointed out in the literature that this issue affects the membrane durability (Weber *et al.*, 2004c; Mathias *et al.*, 2005). Also, due to the mechanical stresses of the membrane adjacent layers, swelling of the membrane with water uptake is partially constrained (Weber *et al.*, 2004c). This could decrease the membrane water uptake and correspondingly affect its ionic conductivity and the performance.

From the fuel cell systems perspective, the availability of the fuel is very important for an uninterrupted cell operation. The hydrogen production techniques for fuelling PEMFCs are gaining momentum but are also criticized for their dependence on the conventional fossil fuels such as in the case of hydrogen production from steam reforming of natural gas (separation of hydrogen from hydrocarbons). As conventional fossil fuels are expensive and being depleted, the need for competitive hydrogen production techniques (such as PEM-water electrolysis using renewable energies) has to be addressed before the fuel cell technology becomes commercially viable (Bossel, 2005). However, this issue is not the focus of this thesis and will not be elaborated on further.

1.6 Purpose

Modeling is required for the effective design of a PEMFC. It helps in assessing and optimizing the complex performance related issues that are experimentally cumbersome and costly. Estimating the factors such as the membrane water distribution, the influence of channel to land ratios on the anisotropy in mass transport

and the other geometrical effects such as the stress effects of the membrane adjacent layers on the PEM swelling is impractical in day to day lab-scale operations. The corresponding experimental costs to perform these complex studies are also very high.

1.6.1 Thesis Objectives

The objectives of the current project are as follows:

- To develop a reliable and robust two-dimensional numerical/computational approach for solving the PEM fuel cell membrane layer mass (proton and water) transport equations using a finite volume method.
- To analyze the effect of anisotropy in mass transport near the membrane - cathode active layer boundary on the membrane water distribution and local ionic current densities and examine the relevant implications on water dependent membrane transport properties such as the ionic conductivity and the corresponding local ohmic losses.

1.6.2 General Approach for Modelling

The general mathematical approach for the membrane layer model is based on concentrated solution theory of Newman *et al.* (2004). The frictional coefficients of interaction between the individual species have been expressed in terms of the membrane transport properties (Fuller *et al.*, 1992). The framework of Weber *et al.* (2004a) has been adopted for calculating membrane layer mass transport with wide-ranging humidifying conditions (vapour or liquid humidified).

The model for studying the anisotropic mass transport effects at the membrane-cathode PTL interface is a cross-the-channel, two-dimensional domain of a PEM bonded to a cathode. The computational approach does not include the regions of

catalyst layer, PTL, and the flow field plate but the corresponding boundary condition data for investigating the relevant effects of PTL induced anisotropic mass transport has been obtained from the literature (Sun *et al.*, 2005a-c). The two-dimensional membrane layer mass transport model has been implemented using an in-house numerical algorithm developed based on a finite volume method (Patankar, 1980; Versteeg *et al.*, 1995).

1.6.3 Scope and Limitations of the Thesis

The model explains the underlying principles of the PEM phase mass transport from both physical and mathematical perspectives. It sets up a computational framework that considers all the driving forces, which are significantly responsible for the proton and water transport in both vapour and liquid phases across the PEM. The model allows calculating the membrane water profile with wide-ranging humidification schemes (vapour and liquid equilibrated PEMs) at the membrane-electrode boundaries and for different Nafion® membranes (112, 115 and 117). Simulating transport across membranes with different thicknesses could give better idea of ohmic resistances.

More importantly, the model helps in researching and identifying the factors causing distributions in transport properties and ohmic losses across the membrane. The analysis resulting from such study can throw light on how the PEM phase transport properties are affected by the anisotropy in the mass transport. A two-dimensional membrane model developed in this work also allows for studying the deviations in local current densities near the cathode side of the PEM and can be

helpful in optimizing for a better flow field plate pattern improving the performance of the membrane.

From a practical point of view, the geometrical/mechanical constraints of the MEA does not allow for the PEM swelling (Weber *et al.*, 2004c), this is because the membrane is hot-pressed between the porous transport layers and any membrane swelling will be suppressed by the mechanical forces at the membrane - PTL interfaces. Hence, the swelling studies might not support the actual PEM phase mass transport. In order to predict the effects of swelling constraint on the PEM, the model has been modified to account for the variations in membrane water content with the swelling constraint. An improved model accounting for the membrane swelling constraint aspects, based on Weber *et al.* (2004c) approach, helps identify the relevant implications on mass transport.

A limitation with the PEM layer transport model is that it cannot be fully validated unless it is embedded in a complete fuel cell model that describes the transport in all the layers of the fuel cell. This is because of the continuity of fluxes between various layers of the MEA. Therefore the transport in the porous transport layers has to be simulated before computing the membrane phase transport. It also has to be mentioned that the membrane model developed in this work does not account for any gas crossover across the membrane (from porous transport layers) and neglects the corresponding performance related aspects, which become a limitation from the modeling perspective. The numerical model assumes an isothermal operation, which neglects the temperature fluctuations arising inside the membrane because of ohmic heating and enthalpies of reaction. This may be a significant limitation because

thermal gradients can drastically alter water activities. The phenomena such as gas fuel and oxidant crossover into the fuel cell membrane were also neglected. The impact of these issues might not significantly alter the profiles of membrane variables of water and charge transport. Hence, not accounting these factors in the numerical model may not be a significant limitation.

As the current work aims investigating the anisotropic effects near the membrane - cathode PTL half-cell, it assumes that the protonic potential (PEM phase) and water distribution along the anode-membrane interface remains constant throughout. In reality, these assumptions may not hold well because the current density at the anode-membrane interface may vary due to mass transfer losses and the inherent conductive resistances at the PTL - catalyst interfaces. Nevertheless, the assumptions holding for conditions at anode PTL-membrane interface can lead to good approximations of the details focusing on the influence of the anisotropic transport issues at the membrane-cathode PTL interface on the membrane performance.

1.7 Thesis Outline

Chapter two discusses the membrane phase mass transport based on the concept of percolation, which supports the mathematical framework presented in Chapter three. Chapter three presents the mathematical model of the mass transport inside a free-swelling membrane in both vapour and liquid phases. It also describes the relevant importance of the membrane transport properties in the mathematical model and the impact of constraining the membrane swelling on its conductivity. The computational algorithm for solving the model is described in Chapter four. The preliminary results of the simulation model, presented in Chapter four, attempt to

validate the computational procedure developed to simulate the membrane model. Chapter four also discusses an overview of computational aspects and limitations associated with the computational algorithm. Chapter five addresses the key issues relating the model results showing the effect of anisotropic boundary conditions on the performance of the membrane. It mainly identifies the membrane performance affecting factors influenced by the cathode side conditions and external flow field plate design aspects. It also presents a parametric study revealing the effect of membrane physical properties on the conductive losses. A further part of the chapter includes discussion on the effect of constraining the membrane swelling on water retention and ionic conductivity. Chapter six concludes the thesis by summarizing the main observations based on the results discussed in preceding chapters and recommending critical development issues for enhancing the applicability of the mathematical model.

2. LITERATURE REVIEW

2.1 Introduction

The technology of proton exchange membrane fuel cells (PEMFCs) has taken several strides towards achieving the performance that matches the power requirements of commercial applications. The critical aspect restraining the PEMFC from being used widely in commercial applications is its cost; improving the cell performance reduces the number of fuel cells required in a stack and thereby cuts down the costs. Several theories (Springer *et al.*, 1991; Bernardi *et al.*, 1992; Fuller *et al.*, 1993; West *et al.*, 1996; Weber *et al.*, 2004a-c) have indicated that the performance of the cell depends on numerous factors such as efficient water and thermal management in the PEM, reaction kinetics and the structure and durability of the MEA. Considering the importance of the PEM in a fuel cell, an extensive literature survey was done to understand the principles involved in the transport of protons and water across the membrane from both physical and mathematical point of views. The influence of the external design factors (such as channel-land configurations of the flow field plates) on the anisotropy in the mass transport has also been reviewed. The purpose of this chapter is to present the underlying physical concepts that are associated with the conductivity of protons through the ionic conducting pathways across the PEM and to discuss the mathematical models used to compute the mass transport.

2.2 Structure and Ion Conducting Nature of a Polymer Electrolyte Membrane

Nafion® membranes are commercially produced by DuPont® and are generally used as ion conducting PEMs in fuel cells. Other PEMs that are popular and available commercially are Aciplex® by Asahi Chemical and Flemion® by Asahi Glass (Smitha *et al.*, 2005). These membranes differ in their physical characteristics such as equivalent weights (*EW*) and thicknesses. Equivalent weight of a PEM can be defined as the mass of membrane in grams per equivalent of sulfonic acid groups. The physical properties such as PEM equivalent weight and thickness affect the transport of protons and water. Hydrated Nafion® 1100 *EW* membranes (acid and expanded form) are known to show better ionic conducting nature and mechanical stability at fuel cell operating temperatures (Costamagna *et al.*, 2001). Also, their physical characteristic data and transport parameters are widely researched and available in the literature. Hence, these membranes have been chosen and are studied here from a modelling perspective.

2.2.1 Structure of a Polymer Electrolyte Membrane

A Nafion® membrane is a perfluorosulfonic-acid (PFSA) polymer structure, made up of polytretrafluoroethylene (PTFE) groups having oxygen atoms, CF_2 and SO_3H groups linked as side chains. Figure 2.1 illustrates the structure of a Nafion membrane. The sulfonic acid (SO_3H) groups terminating the side chains are the hydrophilic regions in which the protons are co-valently bonded to the sulfonate groups. Nafion® exhibits a hydrophilic nature near to the sulfonic acids in side chains and a hydrophobic nature near to the PTFE in the main chains. The charge conduction capability of the PEM depends on its hydration state. Hydrophilic regions of the

sulfonic acid groups allow Nafion to absorb water and exhibit an ion conducting property.

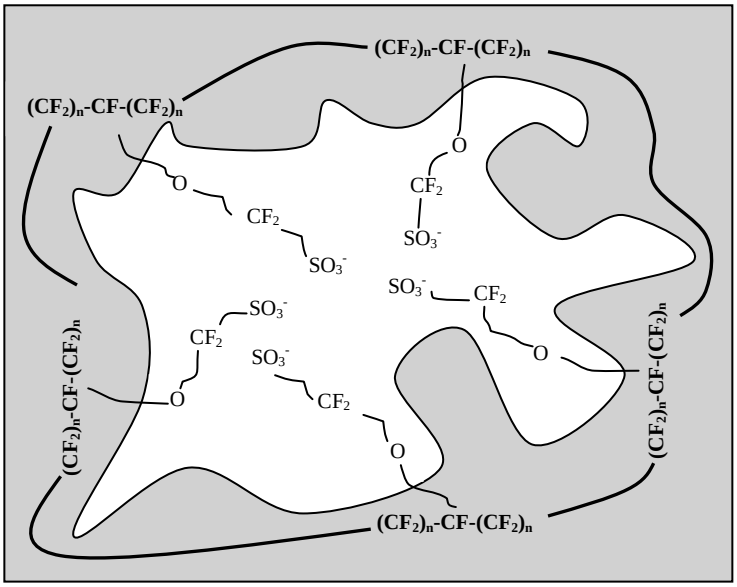

Figure 2.1: Structure of a Nafion® Membrane (Carrette *et al.*, 2001)

Apart from the hydration state, the structure and the conductivity of Nafion also depend on the glass transition temperatures. Beyond the glass transition temperature, the structure of Nafion® no longer remains but becomes viscous and is not favourable for protonic transport. The glass transition temperature of dry Nafion in the acid form is $T_g = 383\,\mathrm{K}$ (Yeo *et al.*, 1977). The glass transition temperature increases with the number of ions present in the structure. Yeo *et al.* (1977) have shown that the glass transition temperature increases with the presence of charged sites in the molecule. It has been shown by Boyle *et al.* (1983) that the fluorocarbon backbone (PTFE) rearranges itself at temperatures above the glass transition ($T \geq 393\,\mathrm{K}$) and its motion is constrained in the presence of the ionic clusters in the vicinity.

As illustrated in Figure 2.2, during the operation of a PEMFC, the hydrophilic areas of the Nafion® attract water molecules along with protons that move from one negatively charged site (sulfonate groups) to another progressing towards the cathode. The potential gradient across the membrane becomes the primary driving force for protonic flux through the PEM that has been hydrated with water (Verbrugge *et al.*, 1990). Figure 2.2 presents a general illustration of ionic transport from a macroscopic point of view and does not necessarily represent the actual proton transport with water complexes.

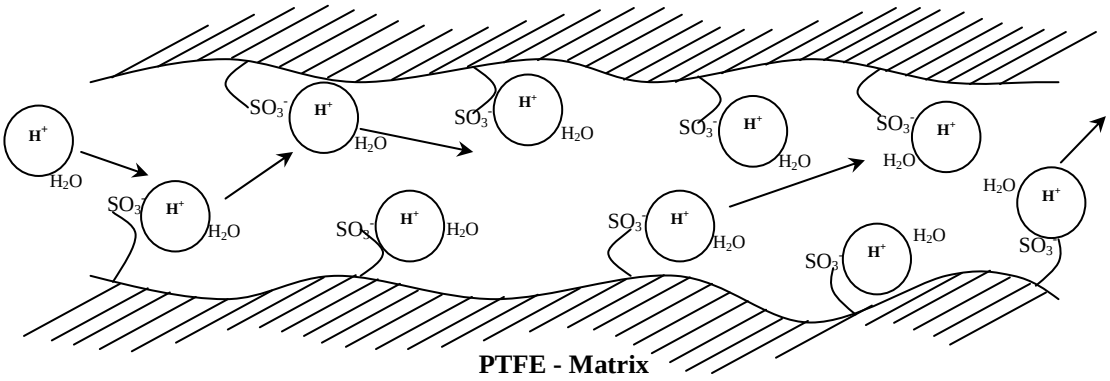

Figure 2.2: Movement of protons and water molecules in a Nafion® membrane

2.2.2 Ion Conductivity across the PEM: A Physical Perspective

The micro structure and hydration state of a PEM are important factors that affect its ion conducting nature (Hsu *et al.*, 1980). It has to be mentioned that the mechanism of proton transport in the vapour phase is fundamentally not the same as that in the liquid saturated PEM. Several studies (Yeo *et al.*, 1977; Yeager *et al.*, 1981; Hsu *et al.*, 1982; Yeo, 1983; Weber *et al.*, 2003) have aimed at understanding the actual mode of proton transport through ion conducting (Nafion) membranes. Yeo *et al.* (1977) have identified, using small angle x-ray scattering (SAXS), that ions

cluster inside the Nafion® membranes. Falk (1980) has shown that hydrated Nafion membrane structure has two phases: one with hydrated ionic clusters and another with a fluorocarbon backbone.

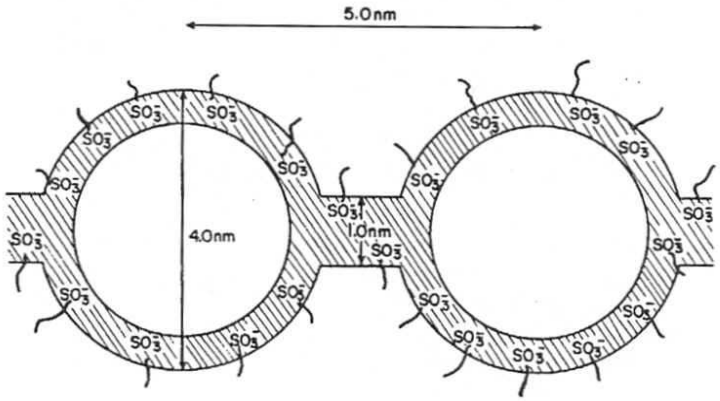

Figure 2.3: Cluster-Network Model (Hsu *et al.*, 1983)

Hsu and Gierke (1982) first set the physical framework for the PEM phase ion clustering and motion. They explained the percolative process of ion transport using a (spherical) cluster-network model. The cluster-network model, based on elastic theory, describes the cluster diameter as a function of cation form, equivalent weight and water uptake by electrolyte. Figure 2.3 illustrates the cluster network model, according to which a spherical cluster 4.0 nm in diameter is connected by an ion conductive channel 1.0 nm in thickness. The distance between two adjacent clusters in an ion conductive domain is 5.0 nm. According to percolation theory, at the threshold volume fraction of water, the formation of sufficient ion conducting pathways allows Nafion to inhibit its insulating properties and conduct ions. Conductivity beyond the percolation threshold depends on the extent of the network of the ionic pathways (or channels) that connect the hydrophilic ionic clusters. This network of ionic pathways

helps ionic movement from one cluster to the other. Below the threshold water content, ionic pathways cease to exist and Nafion behaves as an insulator.

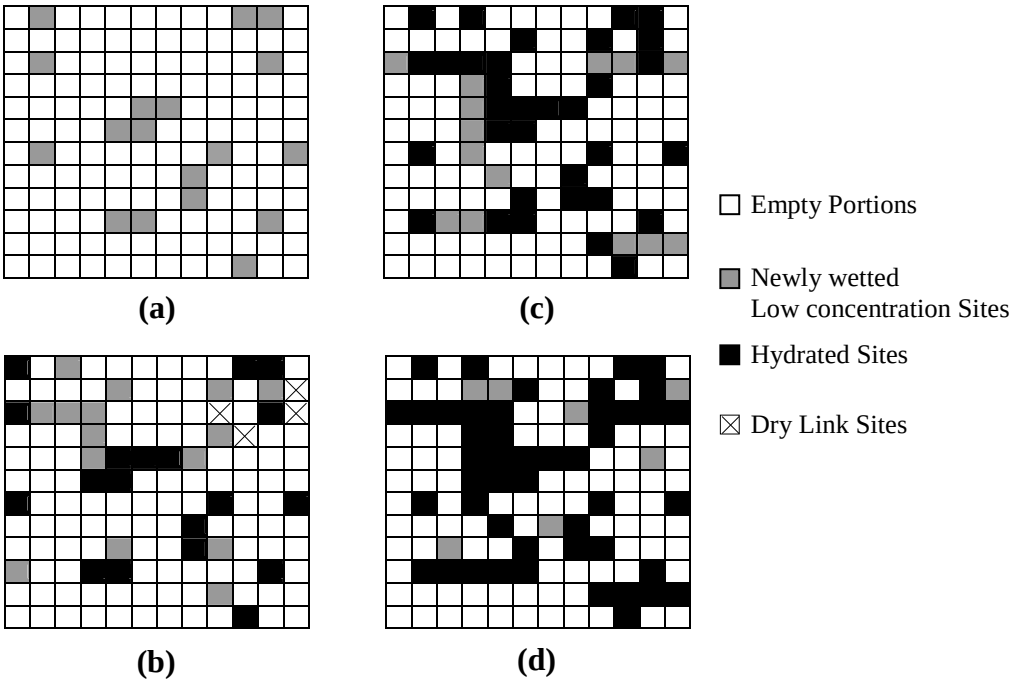

Figure 2.4: Two-dimensional illustration of percolation theory (Hsu *et al.*, 1983)

Figure 2.4 illustrates the theory of percolation proposed by Hsu *et al.* (1980). The gray boxes in Figure 2.4(a) indicate the clusters of hydrophilic sulfonic acid sites that are located randomly across the PEM and are surrounded by the hydrophobic PTFE back bone. As the water uptake by the PEM increases, these clusters absorb water molecules and expand. At this stage, the cluster diameter of each site tends to grow and the clusters adopt a shape of inverted micelle. These are represented by black boxes in Figure 2.4(b). Simultaneously, some newly wetted sites are formed that are represented by grey boxes. The clusters are connected to each other by narrow channels, which act as ionic pathways for conduction. While in this state, there will also be some dry regions between the clusters, which inhibit the ionic flow across the PEM. These regions are represented by hatched portions.

Figure 2.4(c) shows the membrane where water uptake reaches the threshold volume fraction. The dry portions become wet and the ionic pathways tend to connect the clusters that are wetted by water, but there will still be some isolated regions that hamper the ionic conductivity. Finally, as water uptake by membrane increases beyond the threshold volume fraction, all the hydrophilic regions of the membrane become wet and are connected by interfacial channels that are collapsed (narrow ion conducting pathways). These channels allow for ionic transport across the PEM that is equilibrated with water vapour. This phase of the membrane is shown in Figure 2.4(d). A percolation type mechanism explains the vapour phase membrane ionic conductivity but it does not support the liquid phase ionic transport, where proton-water complexes permeate through the channels that are sufficiently expanded to accommodate the liquid water (Weber *et al.*, 2004).

Weber *et al.* (2003) addressed both vapour and liquid phase transport mechanisms in the PEM. Though the underlying principles of vapour phase ionic transport remain the same as the one by Hsu *et al.* (1983), it has been shown that vapour phase ionic transport occurs through the collapsed channels (ionic pathways) that resist the predominant hydrophobic nature of surrounding PTFE matrix. The proton conductivity and the proton drag induced (electro-osmotic drag) water movement in the vapour phase occur in the form of hydronium ion complex. Protons of this complex diffuse by hopping from one charged site to the other and proceed towards the cathode side (Thampan *et al.*, 2000). The ionic transport may also occur by the *Grotthuss* mechanism in which protons of the hydronium ion complex move with covalently bonded water molecules from one charged site to the other (Ren *et al.*,

2001). These proton transport mechanisms are hypothetical. In the vapour hydrated PEM, the chemical potential gradient of the water becomes a fundamental driving force behind non electro-osmotic drag of water.

In the case of the PEM that is equilibrated with liquid water, the hydraulic forces exceed the elastic forces of PTFE and expand the collapsed channels. Thus, water flow occurs because of the hydraulic permeability and through the expanded channels that connect the clusters and form the continuous pathways for both ionic and water transport. The ionic conductivity in liquid saturated membranes occurs with proton hopping and electro-osmotic drag of water occurs in the form of a *Vehicle* mechanism, which can be described as bulk phase proton transport (rather than surface hopping from one site to the other) along with water molecules through the liquid infiltrated pores or channels. The proton transport mechanisms also depend on the surrounding temperatures. At high temperatures, the liquid phase proton transport occurs predominantly by the *Vehicle mechanism* (Ren *et al.*, 2001; Weber *et al.*, 2004a).

Figure 2.5 shows Weber's (2003) approach of classifying the modes of mass transport across the PEM. The dry membrane with a water content $\lambda = 0$ (λ is the ratio of number of water molecules to the sulfonic acid sites), corresponds to the dark spots in Figure 2.5. The hydrophilic sulfonic acid sites are located randomly throughout the PEM and are surrounded by the hydrophobic PTFE back bone (grey background). The state of the PEM below the percolation threshold at $\lambda < 2$ shows that hydrated clusters of charged sites are distributed randomly but are not connected with the surrounding sites to conduct ions. Next, the illustration at $\lambda = 14$ in Figure

2.5 shows that the water uptake has increased beyond the threshold volume fraction and the membrane has been saturated completely with water vapour. At this stage, all the hydrophilic regions of the membrane become wetted and are connected by interfacial channels that are collapsed (ionic pathways). The network of ion conducting pathways between the clusters can be observed.

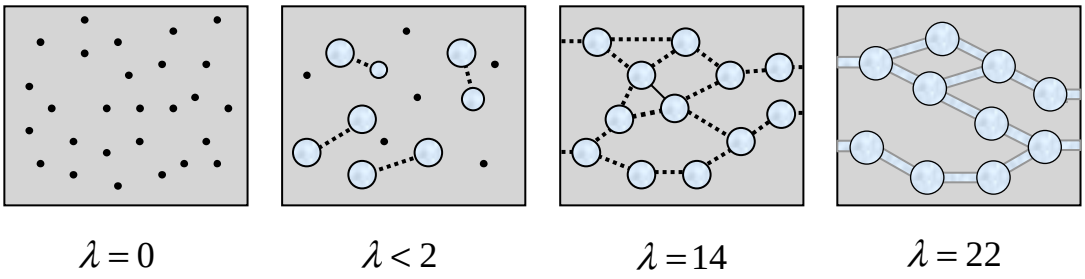

Figure 2.5: Schematic of mass transport in the PEM (Weber *et al.*, 2003)

When the PEM is completely hydrated with liquid water at $\lambda = 22$, the hydraulic pressure of liquid water expands the ionic pathways that are suppressed by hydrophobic PTFE backbone. In this phase, the movement of protons occurs mainly through the channels that are filled with bulk phase of liquid water (the *Vehicle* mechanism). For a situation where both vapour and liquid phases exist simultaneously across the membrane, the mass transport occurs as a separate process in both vapour and liquid equilibrated portions of the PEM and it can be calculated based on the fraction of expanded channels and the fraction of collapsed channels. This concept explains the PEM water uptake ranging between $\lambda = 14$ and $\lambda = 22$.

In summary, the physical framework describes both vapour and liquid phase transport across the PEM. Percolation theory suggests expressing the PEM proton conductivity based on the amount of water vapour it has absorbed. The capillary

concept by Weber *et al.* (2003) suggests that the proton conduction in the liquid phase occurs through the channels that are expanded by the hydraulic flux. More importantly, the concept of the capillary phenomenon in liquid equilibrated PEM explains Schroeder's paradox, a behaviour exhibited by polymers that can be described as a difference in the amount of water uptake by the PEM equilibrated with water vapour to that of a membrane saturated with liquid water (Zawodzinski *et al.*, 1993b; Futerko *et al.*, 1999; Choi *et al.*, 2003; Weber *et al.*, 2003). This has long been a mystifying behaviour shown by polymers, which was originally coined by Schroeder (1903).

2.2.3 Swelling of a Nafion Membrane

Another phenomenon that can be observed in an unconstrained membrane is that it swells upon absorbing water. Hence, the change in the PEM dimensions has to be accounted for when modelling. Swelling in both the in-plane thickness and transverse directions can be considered to be equal according to the experimental work of Gebel *et al.* (1987). The volume of a fully swollen membrane with water uptake of, $\lambda = 22$, increases by 74% of above that of a dry membrane. Gebel *et al.* (1987) and Hsu *et al.* (2003) showed that the swelling along the manufactured length of Nafion® 117 (1100 *EW* and 7 mils thickness) is more than that in the directions of thickness and width, and the experimental evidence showed that swelling was isotropic in the directions other than the manufactured direction (along the length). Figure 2.6 shows the length, width and thickness of the membrane, and the aspect ratio of channel to land is 2:1. The increase of the membrane volume causes variations in the geometry and dimensions of the PEM which affect the driving forces of the mass transport.

PEM swelling increases the water uptake but in reality the PEM is constrained by the mechanical forces exerted on the MEA by flow field plates. Therefore the mass transport inside a free-swelling PEM does not necessarily represent the realistic phenomena.

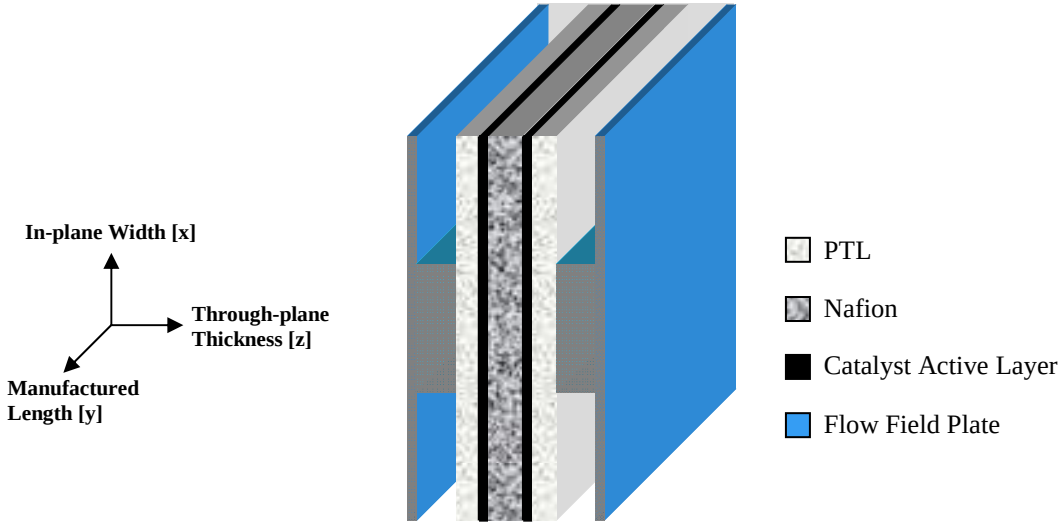

Figure 2.6: A schematic of a Nafion® embedded in the MEA

2.3 Mass Transport across a Polymer Electrolyte Membrane in the MEA

2.3.1 Phase Potential Distribution across a PEM

Proton migration across the PEM depends upon the hydration state of the charged sites. Improper humidification of these sites can lead to significant voltage losses. Protons are produced by hydrogen oxidation reaction at the anode active layer, driven across the PEM by a protonic potential gradient, and consumed at the cathode active layer by oxygen reduction reaction. The voltage drop across the membrane can be measured with impedance measurements (Slade *et al.*, 2002) and can be determined with numerical modelling also (Weber *et al.*, 2004c). The resistance of the membrane remains constant under well humidified conditions giving a linear potential drop but

the resistance can increase when the membrane becomes dehydrated (Springer *et al.*, 1991; Bernardi *et al.*, 1992) or is not sufficiently humidified. At higher current densities, the chances of the membrane becoming dehydrated are more, the reason for which can be attributed to an imbalance between a greater proton driven electro-osmotic drag flux of water from anode to cathode (Fuller *et al.*, 1993) and a slower back diffusion of water from cathode to anode. The protonic potential drop across the membrane can be used to calculate its resistance and the relation for which can be expressed using Ohm's law as given by equation (2.1).

$$\Delta\Phi = \mathbf{i}R_m, \tag{2.1}$$

where

Φ = protonic potential in the PEM phase [V],

$\mathbf{i}$ = ionic current density [A/cm^2], and

R_m = resistance of the ion conducting membrane [$\Omega \cdot \mathrm{cm}^2$].

Further, in a fuel cell with insignificant conductive losses at electrodes, the ohmic drop across the membrane can be expressed using a fuel cell polarization equation as following:

$$E_{cell} = E_{oc} - \eta_a - \eta_c - \mathbf{i}R_m, \tag{2.2}$$

where

E_{cell} = operating fuel cell voltage [V],

E_{oc} = the open circuit potential (at zero current) [V], and

η = activation overpotential [V].

2.3.2 An Overview of Mass Transport Modelling

Traditionally, PEM fuel cell modelling was based on identifying and investigating the critical issues of MEA water and thermal management. The mathematical models available in the literature can often be classified based on the approaches followed for describing the intricate physico-chemical processes across the layers of the MEA. The models that are based on describing the vapour phase mass transport across the MEA are called diffusion-type models (Springer *et al.*, 1991; Fuller *et al.*, 1993), and the ones that are based on liquid phase transport are termed as hydraulic-type models (Bernardi *et al.*, 1992; Gurau *et al.*, 1998). The physical specifications of the modelling domain are also important in evaluating the dimensional and geometrical factors affecting the fuel cell performance. Based on the computational domains of interest, the macroscopic models can extend from one to three dimensions. One-dimensional models always study the mass transport and performance issues in the through-plane (z) direction (refer to Figure 2.6) of the MEA sandwich. Two-dimensional models study mass transport in both through-plane and along-the-channel (y) or in-plane directions (x). Three dimensional models are usually complex and involve in computing the transport phenomena in all three dimensions of the MEA.

During the operation of a PEMFC, the mass transport across the PEM can be expressed, in part, in terms of relevant driving forces that act on hydrogen ions and water molecules. The significant driving force behind the protonic flux through a PEM is the protonic potential gradient across the membrane. The drag forces arising out of such a flux will also induce the electro-osmotic drag of water from the anode to

the cathode. It can be observed in Figure 2.7 that a portion of water transport through the PEM can also occur in the form of diffusion or hydraulic convection, the driving forces for which are dependent on both the extent of inlet gas humidification and the amount of water produced at the cathode catalyst layer. Water vapour diffusion is based on the gradient in chemical potential across the membrane. If pressure gradients exist across the membrane, a hydraulic flux will also contribute to the net water flux.

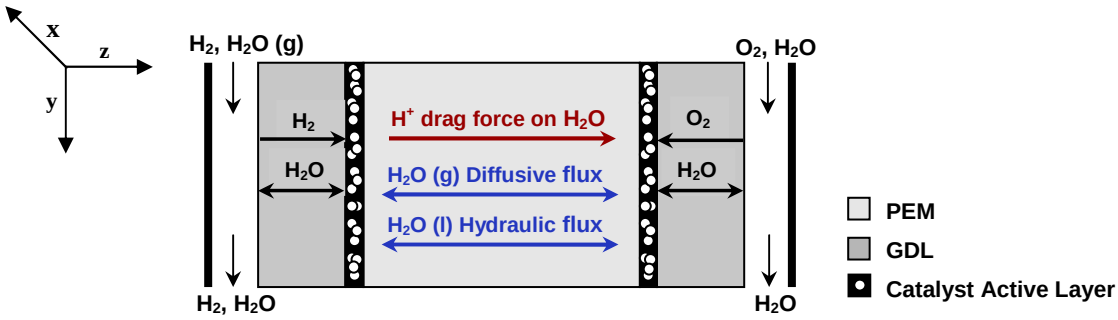

Figure 2.7: A schematic of driving forces of mass transport across the PEM in the through-plane direction

An effective PEMFC humidification scheme maintains a balance between the electro-osmotic drag and non-electro osmotic flow of water, which is critical to avoiding ohmic or mass transfer losses. In essence, the electro-osmotic flux of water from anode to cathode should be balanced by the back water flux (from diffusion or convection) from cathode to anode. In a way, that maintaining the net flux of water near to zero, helps in maintaining the membrane hydration and avoiding the excess water flooding at cathode that blocks the reactant flow towards the active sites of the catalyst layer (Springer *et al.*, 1991; Weber *et al.*, 2004b).

An extensive literature survey was done to understand the principles involved in the transport of hydrogen ions and water through a PEM. It is crucial that a

membrane model for simulating proton and water transport should account for both vapour phase and liquid phase transport, thereby allowing for the observed variations in the membrane transport properties (such as the membrane ionic conductivity) with the corresponding transport mode (vapour or liquid phase). The following review focuses on some of the recent prominent models available in the literature.

- ***Springer, T. E., Zawodzinski, T. A. and Gottesfeld, S., (1991)*** presented a steady state, one-dimensional, isothermal, diffusion-type model of mass transport across the MEA. Stefan-Maxwell equations (Bird *et al.*, 1960) were used to define the fluxes in the porous transport layers. The generation and consumption terms at active layers were simplified with Faraday's law. The water vapour transport inside the membrane was expressed in terms of electro-osmotic flux and diffusion. The membrane water content isotherm at 303 K was fitted with the experimental data of Zawodzinski *et al*. (1991) and was assumed to be valid at the cell operating temperature. This assumption did not result in a good representation of variations in hydration state and the ion conducting nature of the membrane with the cell temperature. The analysed phenomena included a study of variation in membrane water distribution and resistance with cell current density, showing that ohmic resistances increased with current density.

- ***Bernardi, D. M. and Verbrugge, M. W., (1992)*** developed a steady state, one-dimensional, isothermal, hydraulic-type model of a polymer electrolyte fuel cell. The model employed the Stefan-Maxwell equations for gas transport in the porous electrodes, the Butler-Volmer equation for catalyst active layers, the modified Schlögl's equation for calculating liquid water velocity in the membrane, and the

Nernst-Planck equation for calculating species fluxes in the PEM phase. The framework for the species transport within the membrane is based on the dilute solution theory of electrolytes (Newman *et al.*, 2004). Investigated phenomena included the effects of porosity and volume fraction of the electrode on the cell performance. The model showed that membrane resistance at higher current densities (> 200 mA/cm^2) can lead to significant voltage losses across the membrane. However, being a hydraulic-type model, the model did not account for any vapour phase flow and is based on the assumption the membrane was saturated with liquid water, a condition not suitable for polarization studies at low humidification schemes.

- ***Nguyen, T. V. and White, R. E., (1993)*** developed a steady state, pseudo-(1+1)-dimensional model (integration of one-dimensional model along-the-channel) of a PEM fuel cell. The model calculates the local current density distributions in the gas channel. The generation and consumption terms of species were based on Faraday's law. The membrane layer water transport was described in terms of electro-osmotic flux and diffusion but is calculated based on the local mass transport variations in gas channels. However, it does not consider the convective flux of liquid water between the electrodes. The model allows for observing the cell current-voltage relationships under different humidification schemes.

The model was modified by Yi *et al.* (1998) to include liquid water convection that calculates the hydraulic pressure gradient as a simple linear difference of water pressure between the electrodes. Thirumalai *et al.* (1997) have developed a PEMFC stack model based on the unit cell model of Nguyen *et al.* (1993). They

studied the effects of pressure drop and temperature distribution in the flow fields of a PEMFC stack operation.

- ***Fuller, T. F. and Newman, J. S., (1993)*** developed a pseudo-(1+1)-dimensional, diffusion-type mass transport model for the MEA. The regions of the PEMFC modeled were membrane, anode and cathode. The mass transport in the MEA of this model is based on concentrated solution theory (Newman *et al.*, 2004). All relevant interactions between the individual species inside the polymeric membrane were accounted for writing the flux equations. This approach is similar to the one proposed by Pintauro *et al.* (1984), which expresses thermodynamic driving forces in terms frictional interactions between individual species and represents the corresponding thermodynamic frictional coefficients in the form of measurable transport parameters. The effect of the membrane hydration on the cell current densities was analysed and it was shown that ohmic losses increase at higher current densities.

- ***Gurau, V., Liu, H. and Kakac, S., (1998)*** developed a two-dimensional, non-isothermal transport model for a PEMFC. The model considers the combination of different layers as a single computational domain, thereby avoiding the complexities of internal boundary conditions at component interfaces within the MEA. It employs the generalised forms of Schlögl's equation for defining the PEM phase species fluxes, which additionally account for the electro-osmotic and migration terms for water and proton transports respectively. Analysed phenomena include the variations in membrane liquid water velocity fields, which show the balance between the electro-osmotic drag and hydraulic fluxes with cell

current densities. The model explains the changes in mole fractions of species based on the limiting current densities at the interfaces.

- ***Thampan, T., Malhotra, S., Tang, H. and Datta, R. (2000)*** presented a steady state model for the PEM layer transport. The physical approach for such a representation has been based on percolation theory. Transport of protons in the presence of water vapour or liquid occurs in the form of hydronium ion complexes by diffusion, the *Grotthuss* mechanism, and convection (liquid saturated flow). Generalised Stefan-Maxwell equations were used to solve for mass transport in a multicomponent membrane. Membrane water content has been modeled using a multiple finite layers BET model with empirically fitted parameters.

  Details of variations in the membrane conductivity with water content and temperature have been presented for both vapour and liquid phase flows. The model shows that membrane ionic conductivity in the presence of water vapour increases with an increase in membrane hydration and temperature but drops quickly at low relative humidities (< 20 %). In the case of liquid water saturated Nafion®, the ionic conductivity was found to be greater than that of the water vapour saturated one and the reason for which has been attributed to the *Vehicle* mechanism of proton transport at high temperatures. It was also shown that conventional PEMs of Nafion® are not suitable for operating at high temperatures (> 373 K) with fixed partial pressures of water vapour at ambient humidification temperatures (~333 K). The conductivity of the membrane in this case drops a couple of orders of magnitude.

- ***Weber, A. Z. and Newman, J., (2004b-c)*** developed a steady state, one-dimensional, isothermal, diffusion-hydraulic combination type transport model for a PEM and have embedded it in a simple pseudo-(1+1)-dimensional fuel cell model investigating the water management aspects in the through-plane MEA sandwich and that along-the-channel. The proton transport in the vapour phase has been described in terms of hydronium ion complexes and the *Grotthuss* mechanism. The mathematical approach for the model is based on the concentrated solution theory. The two mechanisms of diffusion-hydraulic transport (liquid and vapour phase) in the PEM are combined by using a capillary framework that is based on the fraction of expanded channels in the two-phase domain.

  By expressing the water content in the membrane that has been saturated between vapour and liquid phases, the authors have described the complex phenomena of Schroeder's paradox: The difference in water uptake by a PEM between the one in vapour saturated state and the other with liquid saturated (Weber *et al.*, 2003). The model also shows the temperature dependency of water uptake and the corresponding effects on the PEM transport properties such as ionic conductivity and transport coefficient. Weber *et al.* (2004c) have extended the model to account for the realistic and complex phenomenon such as swelling constraint on the membrane and simulated the membrane layer mass transport. It revealed that constrained membrane water uptake falls and the corresponding water balance studies show that swelling constraint is actually beneficial for fuel cell water management, avoiding flooding of the cathode.

2.4 Influence of External Design Aspects on Anisotropy in Mass Transport

Anisotropy in mass transport significantly affects the cell performance. A vital factor influencing the cause of anisotropy in mass transport across the MEA is the external design factors such as the aspect ratio of channel to land in the flow field plate. West *et al.* (1996) applied the multicomponent vapour phase transport framework of Fuller *et al.* (1993) to a two-dimensional, cross-the-channel, membrane-cathode model and have investigated the influence of land spacing on the performance of the hypothetical membrane-cathode half cell. It was revealed that the anisotropy in mass transport at the membrane-cathode PTL increases with increase in the land width. They observed that the membrane water content increases in the portion of a MEA under the land (with the increase in the land width) and the deviations in local current densities were found to be nearly 20%. A limitation with their model is that it is estimates the membrane water content based on an empirical expression and overestimates the transport properties such as electro-osmotic drag coefficient and the PEM conductivity. Also the thickness of cathode active layer was considered to be zero, which can overestimate the reaction rates. These shortcomings may implicate misjudging the local current densities and corresponding conductive losses in the membrane.

Natarajan *et al.* (2001) developed a two-dimensional, two-phase, cross-the-channel transient model of a PEMFC cathode half cell. It inherited the properties of the multicomponent transport model of Yi *et al.* (1999) and investigated the influence of land sizing and geometry on the performance of cathode half cell. It was observed that at higher cathode overpotentials, liquid water discharge is vital for the

performance of oxygen reduction reaction. They also studied the effects of temperature and the gas diffusion layer (or PTL) thickness in influencing liquid water discharge from cathode. It was revealed that thinner porous transport layers (10 microns) showed better current densities at low and moderate cathode overpotentials ($\approx 0.3\,\mathrm{V} - 0.5\,\mathrm{V}$). However, a limitation with their model is that the catalyst layer is infinitely-thin, which can over predict local current densities. Also, their modelling framework did not consider for observing the imminent effects of the flow field plate influenced anisotropy in the membrane layer.

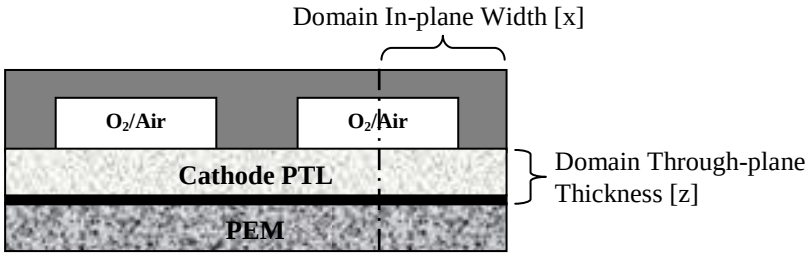

Figure 2.8: Schematic of a cathode half-cell modelling domain

Sun *et al.* (2005a) have investigated the effects of issues causing the anisotropy in the mass transport. Their model is also a two-dimensional, cross-the-channel model of a catalyst layer bonded to the cathode PTL but the geometry of which is much more detailed. In essence, the catalyst layer of the model is an agglomerate structure, which has a thickness of 15 μm. Figure 2.8 illustrates the geometry and the computational domain of Sun *et al.* (2005a) model. They have shown that local current densities depend on the nominal cathode overpotentials (NCO) and the aspect ratios of channel-to-land. The NCO can be defined as a potential difference between the solid phase (PTL) electric potential, Φ_s and the protonic potential, Φ in the PEM phase (Sun *et*

al., 2005a). The operating cell voltage can be obtained by subtracting the NCO from the open circuit cell potential (the cell potential at zero current).

The results by Sun *et al.* (2005a) revealed that the maximum in the local current density shifts from the regions under the land to the regions under the channel with increase in NCO. At a low NCO of 0.3 V, the maximum in the local current density was shown to occur in the region under the land. The corresponding phenomenon implies that oxygen diffusion is not a rate limiting factor. Although their model does not include the PEM layer mass transport, a plausible reason for the increase in proton conduction in the regions under the land can be the increase in the membrane water content in the regions under the land. At moderate and high NCOs of 0.5 V and 0.7 V respectively, the maximum in current density shifts gradually towards the regions under the channel. This indicates that at high NCOs oxygen diffusion affects the reaction rate.

The effect of channel-to-land configurations on the local current densities has been revealed by Sun *et al.* (2005b). A channel-to-land ratio of 2:1 at a NCO of 0.6 V has shown a 7% increase in the average current density above that with 1:1 aspect ratio. The increase in the current density has been attributed to the rapid diffusion of oxygen towards the regions under the channel. At low NCOs ($\approx 0.3\,\mathrm{V}$), the increase in channel to land ratio has no effect on the average current density but the decrease in the ratio has affected the average current density to decrease slightly. A reason for the latter effect can be the decrease in the area of the land, which is critical for the electron conduction.

Kumar *et al.* (2003) have investigated the issues relating to the flow field plate designs at the anode half-cell. They have shown that these factors contribute towards the anisotropy in the mass transport near the anode. Since it is known that the anodic hydrogen oxidation reaction is much faster when compared to the cathodic oxygen reduction reaction, the issues of the anisotropic mass transport in the anode may not significantly contribute towards the cell performance.

2.5 Summary

Several mathematical models have been proposed describing mass transport across the membrane (Springer *et al.*, 1991; Bernardi *et al.*, 1992; Fuller *et al.*, 1993) but none of those have explained both vapour and liquid phase mass transport. More recently, Weber *et al.* (2004) have developed the PEM mass transport model, which described both vapour and liquid phase transport in the membrane and has also taken into account the geometrical factors such as membrane swelling and the corresponding mechanical limitations. Their model is very useful in studying the cell performance with wide-ranging inlet conditions and analyzing near realistic situations such as mechanical effects on the MEA (such as stress effects on the water swollen PEM). The model by Weber *et al.* (2004) is one-dimensional in the PEM, which does not allow studying the effects of anisotropy in the mass transport at membrane-PTL boundaries.

A two-dimensional cross-the-channel model of the cathode half-cell by West *et al.* (1996) investigates the influence of channel to land ratios on the cell performance, but it over estimates the transport properties such as electro-osmotic drag coefficient and local current densities. Sun *et al.* (2005a) model is detailed in catalyst layer and

PTLs but it does not model the mass transport in the membrane layer. Hence, their framework does not allow for observing the relevant effects of flow field plate configurations on the mass transport and conductive losses inside the membrane. Perhaps it is much more vital to study how the membrane layer mass transport is influenced by the anisotropic conditions in the porous transport layers resulting from flow field plate design limitations.

3. MODELLING MASS TRANSPORT IN THE MEMBRANE

3.1 Introduction

The purpose of this chapter is to describe the mathematical equations governing the transport phenomena inside the PEM layer of a PEMFC. The approach adopted and developed in this chapter is a rigorous mathematical framework that supports the computational algorithm for achieving the objectives the current work. The multicomponent framework of a diffusion-hydraulic model was set using concentrated solution theory of Newman *et al.* (2004). The frictional coefficients of interaction between the individual species in the PEM phase have been expressed in terms of transport properties. This approach is the similar to one given by Fuller *et al.* (1992). The capillary equations of Weber *et al.* (2004) have been utilised for explaining the governing equations of the combination type diffusion-hydraulic model. This sort of framework allows for analysing the PEM phase muticomponent system and the corresponding transport parameters with wide-ranging humidification schemes. The physical approach described in section 2.2 provides the hypothetical explanation of the proton-water transport modes in vapour and liquid saturated phases of PEM and supports expressing membrane transport parameters such as PEM ionic conductivity based on the membrane water content.

It is crucial that PEM phase mass transport model should also account for realistic situations such as mechanical stress effects on the PEM that are influenced by

the architecture the fuel cell. The approach of Weber *et al.* (2004c) will be followed for to account for such effects when calculating the membrane transport properties and analysing the relevant implications on membrane water distribution.

3.2 Multicomponent Transport in the PEM

3.2.1 Vapour Phase Transport Modelling

According to Newman *et al.* (2004), mass transport in a concentrated system (such as polymer electrolytes) occurs because of the driving forces acting on the individual species. The relevant interactions between the individual species of such system play a vital role in balancing these forces. A transport framework based on concentrated solution theory considers the relevant interactions between the species in the PEM phase and accounts for all the significant driving forces that are responsible for transport of hydrogen ions and water across the PEM.

In multicomponent solutions such as the one in the PEM, the movement of hydrogen ions and water molecules is relative to the stationary sulfonate groups (SO_3^-) of the PEM. The membrane has to be assumed as electrically neutral where the number of protons equals the number of sulfonic charged sites and the interactions between the components (hydrogen ion, water, and membrane charged sites) become important for calculating the driving forces of mass transport. All driving forces of mass transport are highly dependent on the transport properties of the PEM. The primary driving force causing protonic transport is the protonic potential gradient across the membrane and the secondary cause for protonic flux is the proton-water interactions in the electro-osmotic drag of water molecules. These driving forces increasingly depend on factors such as membrane ion conducting ability, the PEM

hydration state, and electro-osmotic drag coefficient of water molecules. On the other hand, water transport occurs in the form of electro-osmotic flow with the proton migration from anode to cathode. If there are any chemical potential or pressure gradients between the electrodes, it also occurs in the form of diffusion or convection, respectively.

The general form of the multicomponent diffusion equation within concentrated solution theory expresses the driving forces for mass transport in terms of species velocities, given by Newman *et al.* (2004) as

$$c_i \nabla \mu_i = \sum_{j \neq i}^{n} K_{ij} (\mathbf{v}_j - \mathbf{v}_i) = RT \sum_{j \neq i}^{n} \frac{c_i c_j}{c_T \mathscr{D}_{ij}} (\mathbf{v}_j - \mathbf{v}_i) \tag{3.1}$$

where

c_i = the concentration of species i [mol/cm^3],

K_{ij} = the frictional coefficient of interaction between species i and j [J·s/cm^5],

$\mathscr{D}_{ij}$ = the binary diffusion interaction coefficient in the PEM phase [cm^2/s],

μ_i = the electrochemical potential of species i [J/mol],

R = universal gas constant [J/mol·K],

T = temperature [K],

$\mathbf{v}_i$ = the velocity of species i [cm/s],

and where

$$K_{ij} = \frac{RTc_i c_j}{c_T \mathscr{D}_{ij}}, \tag{3.2}$$

$$c_T = \sum_i c_i \ . \tag{3.3}$$

According to Newton's third law, for every action there is an equal and opposite reaction, $\mathscr{D}_{ij} = \mathscr{D}_{ji}$ and $K_{ij} = K_{ji}$ (Onsager, 1931, Newman *et al.*, 2004).

Equation (3.1) can be modified so that species velocities can be expressed in terms of driving forces:

$$c_i \nabla \mu_i = RT \sum_{j=1}^{n} M_{ij} (\mathbf{v}_j - \mathbf{v}_m), \tag{3.4}$$

where

M_{ij} = the modified friction coefficient of species *i* and *j*, [J·s/cm^5], and

$\mathbf{v}_m$ = the reference velocity, the velocity of sulfonate groups, $v_m = 0$

and where

$$M_{ij} = K_{ij}, (i \neq j), \tag{3.5}$$

$$M_{ii} = K_{ii} - \sum_k K_{ik} \ . \tag{3.6}$$

Applying equation (3.4) to the system of hydrogen ions, water vapour and charged sites in a PEM gives the equations for frictional driving forces acting on individual species in terms of the species velocities:

$$c_+ \nabla \mu_+ = RT\left[M_{++}(\mathbf{v}_+ - \mathbf{v}_m) + M_{+0}(\mathbf{v}_0 - \mathbf{v}_m)\right], \tag{3.7}$$

$$c_0 \nabla \mu_0 = RT\left[M_{00}(\mathbf{v}_0 - \mathbf{v}_m) + M_{0+}(\mathbf{v}_+ - \mathbf{v}_m)\right], \tag{3.8}$$

$$c_m \nabla \mu_m = RT\left[M_{m+}(\mathbf{v}_+ - \mathbf{v}_m) + M_{m0}(\mathbf{v}_0 - \mathbf{v}_m)\right], \tag{3.9}$$

where subscripts +, *0*, *m* represent protons, water, and membrane charged sites respectively.

Given a system of n equations in the form of equation (3.4), only $n-1$ equations and $1/2\,n(n-1)$ transport coefficients are needed to fully describe the multicomponent transport (Newman *et al.*, 2004). Hence, in equations (3.7) and (3.8) there are two independent velocity differences, two independent gradients of electrochemical potentials and three transport coefficients that describe the mass transport equations in a PEM. Using the membrane velocity as a reference, equation (3.7) and (3.8) can be expressed in terms of these independent variables. Using vector-matrix notation, the velocity differences are given by:

$$\begin{bmatrix} \mathbf{v}_+ - \mathbf{v}_m \\ \mathbf{v}_0 - \mathbf{v}_m \end{bmatrix} = \frac{1}{RT} \begin{bmatrix} c_+ \nabla \mu_+ \\ c_0 \nabla \mu_0 \end{bmatrix} . \begin{bmatrix} M_{++} & M_{+0} \\ M_{0+} & M_{00} \end{bmatrix}^{-1} . \tag{3.10}$$

In general, equation (3.6) can be expressed as,

$$\mathbf{v}_i - \mathbf{v}_m = -\sum_{k \neq m} L_{ik} c_k \nabla \mu_k \ , \tag{3.11}$$

where, the inverted frictional coefficients, L_{ik}'s are given by

$$\mathbf{L} = -(\mathbf{M})^{-1},$$

$$\text{or, } \begin{bmatrix} L_{++} & L_{+0} \\ L_{0+} & L_{00} \end{bmatrix} = \frac{-1}{M_{++}M_{00} - M_{+0}M_{0+}} \begin{bmatrix} M_{00} & -M_{+0} \\ -M_{0+} & M_{++} \end{bmatrix}. \tag{3.12}$$

Since the reference velocity (membrane velocity) v_m equals zero, equation (3.11) can be used to determine the molar fluxes of species *i* in a PEM. Consequently, the molar fluxes of protons and water can be expressed as,

$$\mathbf{N}_+ = c_+ \mathbf{v}_+ = -c_+^2 L_{++} \nabla \mu_+ - c_0 c_+ L_{+0} \nabla \mu_0 \tag{3.13}$$

and $$\mathbf{N}_0 = c_0 \mathbf{v}_0 = -c_0 c_+ L_{0+} \nabla \mu_+ - c_0^2 L_{00} \nabla \mu_0 \tag{3.14}$$

respectively.

Fuller (1992) explained the methodology for calculating the inverted frictional coefficients shown in equation (3.13) and (3.14) in terms of measurable transport properties. Consider a case where a PEM has been equilibrated with water and has uniform water concentration throughout. For this type of flow, the protonic flux can be expressed as,

$$\mathbf{N}_+ = c_+ \mathbf{v}_+ = -c_+^2 L_{++} \nabla \mu_+, \tag{3.15}$$

$$\text{giving } -L_{++} = \frac{\mathbf{N}_+}{c_+^2 \nabla \mu_+}. \tag{3.16}$$

For this system of uniform compositions, the electrochemical potential gradient of all species reduces to a function of the potential gradient,

$$\nabla \mu_k = z_k F \nabla \Phi, \tag{3.17}$$

where Φ = potential [V]. By substituting equation (3.17) and protonic flux, $\mathbf{N}_+ = \frac{\mathbf{i}}{F}$, into equation (3.16), one gets the following expression:

$$-L_{++} = \frac{\mathbf{N}_+}{c_+^2 \nabla (F\Phi)} = \frac{\mathbf{i}}{c_+^2 F^2 \nabla \Phi}. \tag{3.18}$$

According to Ohm's law, for a solution of uniform composition, current in the solution is directly proportional to the negative of the potential gradient.

$$\mathbf{i} = -\kappa \nabla \Phi, \tag{3.19}$$

where κ = the conductivity of the PEM [S/cm]. Substituting equation (3.19) into equation (3.18) gives

$$L_{++} = \frac{\kappa}{c_+^2 F^2}. \tag{3.20}$$

In the case where minute current is passed through a membrane that has been saturated with a uniform concentration of water, the electro-osmotic drag flow of water can be expressed as

$$\mathbf{N}_0 = c_0 \mathbf{v}_0 = -c_0 c_+ L_{0+} \nabla \mu_+, \tag{3.21}$$

giving $$L_{0+} = -\frac{\mathbf{N}_0}{c_0 c_+ \nabla \mu_+}. \tag{3.22}$$

The electro-osmotic drag coefficient is defined as the number of water molecules induced (dragged) by each proton moving across a membrane (from anode to cathode) that has no concentration gradient of water. The electro-osmotic drag of water in the membrane occurs in the direction of protonic flux and can be expressed as

$$\xi = \frac{\mathbf{N}_0}{\mathbf{N}_+} \tag{3.23}$$

where ξ = electro-osmotic drag coefficient. Substituting equation (3.23) and (3.19) into equation (3.22) gives

$$L_{0+} = -\frac{\xi \mathbf{i}}{c_0 c_+ F^2 \nabla \Phi} = \frac{\xi \kappa}{F^2 c_0 c_+}. \tag{3.24}$$

When no current flows, the protonic flux becomes zero but the gradient in chemical potential of water still promotes the flow of water from regions of high concentration to regions of low concentration in the membrane. Setting $\mathbf{N}_+ = 0$, equations (3.20), (3.24) and equation (3.13) give

$$\nabla \mu_+ = -\xi \nabla \mu_0. \tag{3.25}$$

The flux of water is governed by Fick's Law of diffusion which relates water flux to the chemical potential gradient, $\mathbf{N}_0 = -\alpha_v \nabla \mu_0$, which when substituted into equation (3.14) gives

$$\alpha_V \nabla \mu_0 - c_0 c_+ L_{0+} \nabla \mu_+ = c_0^2 L_{00} \nabla \mu_0 . \tag{3.26}$$

α_V is the transport coefficient [mol^2/J·cm·s] of water vapour. Substituting equations (3.24) and (3.25) into equation (3.26) gives

$$L_{00} = \frac{1}{c_0^2}\left(\alpha_v + \frac{\kappa \xi^2}{F^2}\right). \tag{3.27}$$

Thus, equations (3.20), (3.24) and (3.27) relate the L_{ij}'s to transport properties: the membrane conductivity (κ), the electro-osmotic drag coefficient of water (ξ) and the transport (diffusion) coefficient of water (α). Substituting equations (3.20), (3.24) and (3.27) into equations (3.13) and (3.14), the molar flux of hydrogen ions and water vapour can be calculated as

$$\mathbf{i} = -\kappa_V \nabla \Phi - \frac{\kappa_V \xi_V}{F} \nabla \mu_0 \text{, and} \tag{3.28}$$

$$\mathbf{N}_0 = -\frac{\kappa_V \xi_V \nabla \Phi}{F} - \left(\alpha_V + \frac{\kappa_V \xi_V^2}{F^2}\right) \nabla \mu_0 , \tag{3.29}$$

where transport properties, κ_V, ξ_V, and α_V are for the gaseous phase. A material balance on species *i* over a control volume ΔV in the PEM gives

$$\frac{\partial c_i}{\partial t} = -\nabla \cdot \mathbf{N}_i + R_i \ . \tag{3.30}$$

where R_i is the rate of generation of species *i* in the PEM phase.

As the flow is steady-state, and there are no membrane phase reactions, water in the membrane phase remains conserved. Equation (3.30) applied for water balance becomes:

$$\nabla \cdot \mathbf{N}_0 = 0. \tag{3.31}$$

Since the membrane must remain electrically neutral, current in the membrane is conserved and is constrained by

$$\nabla \cdot \mathbf{i} = 0. \tag{3.32}$$

Equations (3.28), (3.29), (3.31) and (3.32) describe multicomponent transport in a PEM that is equilibrated with water vapour but do not account for any mass transport that occurs in the form of bulk phase hydraulic flux. Hence, these equations are valid only for a PEM where there are water vapour chemical potential gradients.

3.2.2 Liquid Phase Transport Modelling

In the case of a PEM that has been saturated with liquid water, the hydraulic flux of liquid water can be calculated using Darcy's Law which expresses the convective flux of water in terms of liquid pressure gradient and absolute permeability. This approach is similar to the one given in the membrane transport model by Weber *et al.* (2004). In this case, the gradient in chemical potential for water in equations (3.28) and (3.29) can be written as

$$\nabla \mu_0 = RT \nabla \ln a_0 + \overline{V}_0 \nabla p_L, \tag{3.33}$$

where

a_0 = activity of water vapour,

$\overline{V}_0$ = the partial molar volume of water [cm^3/mol], $\overline{V}_0 = \dfrac{M_0}{\rho_0}$, and

p_L = pressure of liquid water [bar].

When the membrane is equilibrated with saturated liquid water ($a_0 = 1$) and equation (3.33) reduces to that of pressure gradient term:

$$\nabla \mu_0 = \overline{V}_0 \nabla p_L . \tag{3.34}$$

Darcy's Law relates the hydraulic flux of liquid water to the pressure gradient and is expressed as

$$\mathbf{N}_0 = -\alpha_L \overline{V}_0 \nabla p_L , \tag{3.35}$$

where α_L is the transport coefficient of liquid water [mol^2/J·cm·s].

The liquid phase water transport in the membrane can be described by substituting equations (3.34) and (3.35) into equation (3.14), which lead to a set of equations similar to equations (3.28) and (3.29):

$$\mathbf{i} = -\kappa_L \nabla \Phi - \frac{\kappa_L \xi_L}{F} \overline{V}_0 \nabla p_L \tag{3.36}$$

$$\mathbf{N}_0 = -\frac{\kappa_L \xi_L \nabla \Phi}{F} - \left(\alpha_L + \frac{\kappa_L \xi_L^2}{F^2} \right) \overline{V}_0 \nabla p_L \tag{3.37}$$

where the subscript "$_L$" indicates the liquid phase. The systems of equations (3.36) and (3.37) are valid for the membrane that has been saturated with liquid water of pressures greater than 0.75 bar, that which is required to expand all the ionic pathways channels for liquid water flow.

3.2.3 Simultaneous Vapour and Liquid Phase Transport Modelling

For the case where the PEM is in transition between vapour and fully liquid saturated states, the component fluxes are calculated based on the capillary framework of Weber *et al.* (2004). This methodology uses the critical radius of the expanded

channels (pores) for calculating the fraction of expanded channels that have radii greater than the critical radius. The channels whose radii are less than that of critical radius are denoted as the collapsed channels (hydrophobic PTFE surrounded ionic pathways of less concentrated sulfonic acid sites) through which vapour phase transport occurs.

The capillary equation given by Weber *et al.* (2004) is used for calculating the critical radius (r_c) of the channel and is expressed in terms of liquid water pressure and the surface tension of water:

$$r_c = -\frac{2\gamma \cos\theta}{p_L}, \tag{3.38}$$

where

γ = the surface tension of water [N/cm],

θ = the channel contact angle [degrees], and

r_c = the critical radius of the channel [nm].

Ascertaining a value for the channel contact angle is very complicated and an exact value is not readily available in the literature. Following Weber *et al.* (2004a), a value of $\theta = 90.02°$ was used in this work. This value represents a mean value of the ones deduced by Weber *et al.* (2004a) from the PEM water uptake experimental data of Meyers (1998) and Cappadonia *et al.* (1995).

The expression for calculating the fraction of expanded channels given by Weber *et al.* (2004a) was found by integrating the channel size distribution from the critical radius to infinity. It is to be noted that uncertainty involved in modelling the fraction of expanded channels involving nanostructures in macroscopic membrane

domain has not been accounted. The equation for calculating the fraction of expanded channels is given as

$$S = \frac{1}{2}\left[1 - \text{erf}\left(\frac{\ln r_c - \ln(1.25)}{0.3\sqrt{2}}\right)\right], \tag{3.39}$$

where

S = fraction of expanded channels, and

erf = error function.

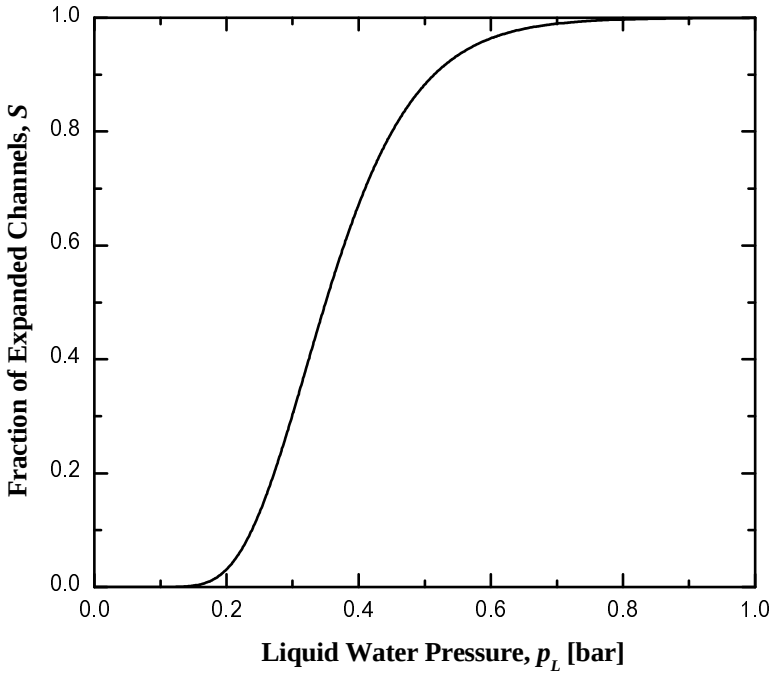

Figure 3.1: Fraction of expanded channels versus liquid water pressure

Figure 3.1, generated using equations (3.38) and (3.39) shows the fraction of expanded channels calculated as a function of liquid water pressures and temperature ($T = 353.15\,\text{K}$). It has been found in the present work that a liquid pressure of $p_L = 0.15$ bar will not have enough hydraulic force to expand the channels. Consequently, the transport through these collapsed channels occurs in a vapour phase.

When liquid pressures reach approximately, $p_L = 0.75$ bar, liquid transport completely dominates. The same was also observed by Weber *et al.* (2004). When the mass transport inside the PEM is dominated by liquid phase, the PEM transport properties change due to their functional dependence on the membrane water content (λ) and temperature.

Equation (3.39), the fraction of expanded channels (S) at a given critical radius (r_c) allows to compute the component of molar flux distributed in the liquid phase. The remaining portion of the molar flux distributed in the in the vapour phase occurs through the collapsed channels. The expressions for calculating the species fluxes are as follows:

$$\mathbf{i} = S\left(-\kappa_L \nabla\Phi - \frac{\kappa_L \xi_L}{F}\overline{V}_0 \nabla p_L \right) + (1-S)\left(-\kappa_v \nabla\Phi - \frac{\kappa_v \xi_v}{F}\nabla\mu_0 \right) \tag{3.40}$$

$$\begin{aligned}\mathbf{N}_0 = {} & S\left(-\frac{\kappa_L \xi_L \nabla\Phi}{F} - \left(\alpha_L + \frac{\kappa_L \xi_L^2}{F^2} \right)\overline{V}_0 \nabla p_L \right) \\ & + (1-S)\left(-\frac{\kappa_v \xi_v \nabla\Phi}{F} - \left(\alpha_v + \frac{\kappa_v \xi_v^2}{F^2} \right)\nabla\mu_0 \right)\end{aligned}. \tag{3.41}$$

The multicomponent transport inside a PEM can now be described for wide-ranging humidifying conditions where water might exist either in vapour and/or liquid phases. For the vapour saturated PEM, the fraction of expanded channels becomes zero and equations (3.40) and (3.41) reduce to equations (3.28) and (3.29). In the case of the PEM which is saturated with liquid water throughout, the fraction of expanded channels is unity and equations (3.40) and (3.41) become that of only liquid phase transport. For a PEM that is equilibrated with both vapour and liquid phases,

equations (3.40) and (3.41) remain the same and the fraction of expanded channels becomes vital in calculating the molar fluxes of the components. In this case, it has to be noted that the number of unknown dependent variables (Φ, μ_0 and p_L) exceed the number of given equations (3.40) and (3.41) and solving such a system is not possible. Hence, the driving force ($\nabla\mu_0$) within the vapour phase has been assumed to be balanced by the one of liquid phase ($\overline{V}_0\nabla p_L$), which is similar to equation (3.34). Equations (3.40) and (3.41) are valid for all three cases in the PEM and the transport properties are calculated with respect to their individual phases.

3.3 Calculation of the Membrane Water Content

It is necessary to understand how the membrane water content varies between the PEM equilibrated with water vapour and liquid water. It is known from the physical explanation provided in chapter 2 that mass transport through the PEM phase is strongly based on its hydration state. The transport properties such as ionic conductivity (κ), electro-osmotic drag coefficient (ξ) and the transport coefficient (α) appearing in equations (3.40) and (3.41) vary with the amount of water uptake by the PEM.

3.3.1 Water Vapour Uptake by a PEM System

The membrane water content, λ, is the ratio of the number of moles of water molecules to that of sulfonic acid sites. Zawodzinski *et al.* (1991) measured the membrane vapour water content, λ_V, at $T = 303\,\mathrm{K}$ and showed that it has a strong functional dependence on the water vapour activity. Their water content data varied little between water activities of 0.15 and 0.75 and the corresponding values of λ_V

were between 2 and 6. The maximum value of λ_V in a vapour saturated PEM was found to be 14. Springer *et al.* (1991) fitted Zawodzinski's (1991) data at $T = 303\,\mathrm{K}$ to a polynomial to give an isotherm of λ_V as a function of activity (a_0). In Springer's correlation, the hydration state of the membrane varies from $\lambda_V = 0$ for a dry membrane to $\lambda_V = 14.03$ for a vapour saturated membrane at $T = 303.15\,\mathrm{K}$. However, the membrane water uptake isotherm by Springer *et al.* (1991) at $T = 303.15\,\mathrm{K}$ might not actually represent the water vapour uptake by the PEM at fuel cell operating temperature ($T < 373\,\mathrm{K}$).

It is not realistic to approximate water contents at water activities lower than required for ion conduction. Also the physical approach of percolation theory described in the previous chapter does not allow for calculating the membrane ionic conductivities in sub-percolation threshold water solvated PEMs. Furthermore, in an ion conducting membrane, charged sites are always bound to a fixed amount of water that allows proton transfer (Hsu *et al.*, 1980; Futerko *et al.*, 1999).

Calculation of the membrane water content based on the cell operating temperature is also very vital for estimating the transport properties. Experimental data by Hinatsu *et al.* (1994) revealed that in the vapour phase, λ_V decreases with an increase in temperature. Thus, a model is required to predict λ_V based on the cell temperature and the membrane water activity.

The thermodynamic model by Futerko *et al.* (1999) calculates the membrane water content as a function of activity and temperature. It assumes that protons are in equilibrium with the water in the hydronium ion complex. The principal basis for this

model is that the transfer of protons in a water vapour solvated PEM occurs in the form of H_3O^+ complexes. The same has been shown by Iwamoto *et al.* (2002) through their experimental investigations. The proton-transfer reaction given by Futerko is shown by equation (3.42),

$$-SO_3H + H_2O(m) \rightarrow [-SO_3^- \cdots^+ H_3O]. \tag{3.42}$$

The model by Futerko *et al.* (1999) uses the Flory-Huggins thermodynamic solution theory for calculating the water vapour uptake by Nafion® 117 at various fuel cell temperatures. According to the Flory-Huggins model, the activity of water vapour, calculated as a function of membrane water content is given as

$$a_0 = (1-\phi_2)\exp\left[\left(1-\frac{1}{r_V}\right)\phi_2 + \chi_F \phi_2^2\right] \tag{3.43}$$

where

r_V = the ratio of molar volumes of the membrane and solvent, $r_V = \frac{\bar{V}_m}{\bar{V}_o}$,

ϕ_2 = the volume fraction of membrane-water system, $\phi_2 = \frac{r_V + \lambda_c}{r_V + \lambda}$,

χ_F = the Flory interaction parameter,

λ_c = the bound water content in the hydronium ion complex, and

$\bar{V}_m$ = the partial molar volume of a dry membrane [cm^3/mol], $\bar{V}_m = \frac{EW}{\rho_{m,o}}$.

Following the analysis of Futerko *et al.* (1999), the bound water content in the hydronium ion complex, λ_c, can be obtained by finding the equilibrium constant for

the proton-transfer reaction given by equation (3.44). The equilibrium constant, *K*, is related to water activity as follows:

$$K_e = \frac{\lambda_c}{(1-\lambda_c)a_0}. \tag{3.44}$$

The temperature dependence of the equilibrium constant has been given as,

$$K_e(T) = (0.0256)\exp\left[\frac{22400}{RT}\right], \tag{3.45}$$

where the proton-transfer enthalpy of 22.4 kJ/mol is for the reaction in a mixture of H_2SO_4 and H_2O (Futerko *et al.*, 1999).

The Flory interaction parameter, calculated as the function of temperature, is expressed as:

$$\chi_F(T) = 1.936 - \left(\frac{2180}{RT}\right). \tag{3.46}$$

Using equations (3.43) and (3.44) with the equilibrium constant given in equation (3.45) and the Flory interaction parameter given in equation (3.46), the membrane water content can be expressed as a function of temperature and computed using a Newton-Raphson method.

Figure 3.2 shows the experimental and computed water vapour uptake by a PEM at two different operating temperatures. It can be observed that the water content in the membrane at a fixed activity decreases with temperature. The calculated data of the water vapour uptake by the PEM has been validated with the experimental data of Hinatsu *et al.* (1994) at 80°C. It also matches closely with the data of Zawodzinski *et al.* (1991) at 30°C.

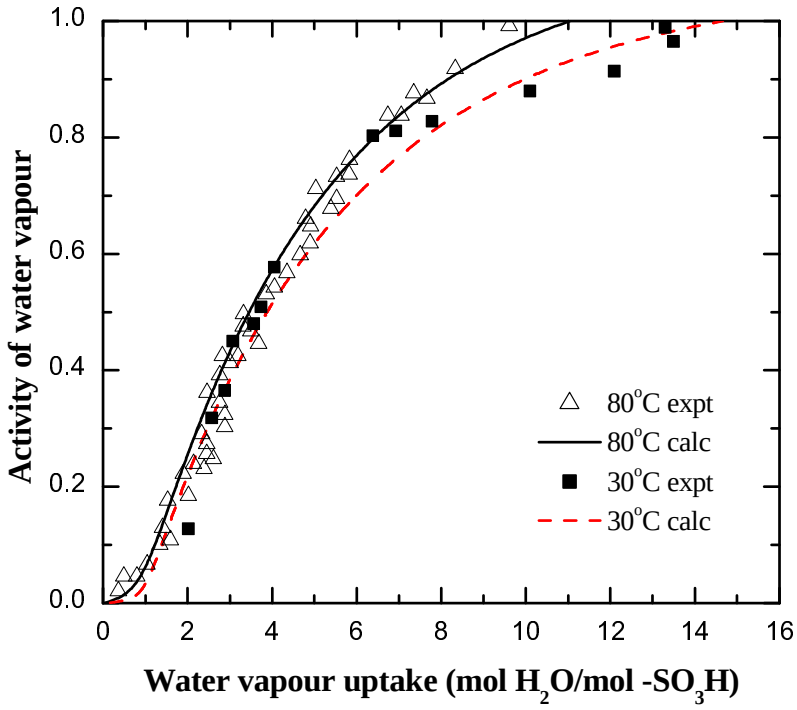

Figure 3.2: Plot of activity as a function of the membrane water content obtained using Flory-Huggins thermodynamic model.

The water uptake by a PEM equilibrated with water vapour differs from that of liquid saturated one. According to the Flory-Huggins model, the decrease in water content with increasing temperature can be ascribed to the exothermic heat of mixing (-2 kJ/mol) from the weaker interactions between sulfonic acid groups and water molecules. Conversely, the endothermic heat of mixing (2 kJ/mol) for the interactions between liquid water and sulfonic acid groups explains why liquid water uptake increases at high temperatures (Futerko *et al.*, 1999). Perhaps this can give a possible explanation to Schroeder's paradox shown by PEMs.

3.3.2 Simultaneous Vapour and Liquid Water Uptake by a PEM System

In the case of a PEM that is saturated with liquid water throughout, the water content, λ_L, has been assumed to remain constant at a value of 22 (Zawodzinski *et al.*, 1993a; Zawodzinski *et al.*, 1993b). For the case where a membrane is neither completely vapour nor fully liquid saturated, water content is calculated based on the concept of the fraction of expanded channels as discussed previously (Weber *et al.*, 2004). The equation for calculating λ in this state is as follows:

$$\lambda = \lambda_V\big|_{a=1} + (\lambda_L - \lambda_V\big|_{a=1})S\,, \tag{3.47}$$

where

$\lambda_V\big|_{a=1}$ = water content in the PEM at unit activity, and

λ_L = water content in liquid saturated membrane, $\lambda_L = 22$.

3.4 Calculation of the PEM Transport Properties

The membrane transport properties such as electro-osmotic drag coefficient (ξ), ionic conductivity (κ) and transport coefficient (α) found in proton and water flux equations (3.35) and (3.36) play a significant role in determining the PEM phase transport by balancing the individual driving forces of transport. These transport properties are calculated based on the membrane water content (λ) and temperature, and are mechanism dependent. Further, these would be useful in analysing the effects of anisotropy in mass transport at the PEM-cathode PTL interface.

3.4.1 Electro-Osmotic Drag Coefficient

The electro-osmotic drag coefficient signifies a proton induced water flux from anode to cathode. Estimation of this parameter is important because, in a good water

management scheme, electro-osmotic flux is ought to balance the diffusive or hydraulic water flux occurring from cathode to anode. The electro-osmotic drag coefficient differs considerably for liquid and vapour water. Thus two correlations are used from literature, both founded upon experimental evidences.

3.4.1.1 Vapour Phase Drag Coefficient

The experimental data of Zawodzinski *et al.* (1995) show that the drag coefficient for vapour phase protonic transport in Nafion 117 remains constant at $\xi_V = 1$ with water content (λ_V) ranging between 1.4 and 14 at $T = 303\,\mathrm{K}$. It has also been suggested that the drag coefficient is not a strong function of membrane micro-structure. The temperature dependence of drag coefficient is not available in the literature. Thus, in this work, The electro-osmotic drag coefficient, ξ_V, of water vapour in the PEM has been fixed to a value of unity and remains constant throughout.

3.4.1.2 Liquid Phase Drag Coefficient

In the case of liquid phase transport, Zawodzinski *et al.* (1995) have shown that the drag coefficient, ξ_L, for a liquid saturated PEM is 2.55. Okada *et al.* (1998) experimentally measured liquid water drag with the streaming potential method and showed that it increases from $\xi_L = 2.6$ at 298 K to $\xi_L = 3.2$ at 353 K. The reason for the increase in drag coefficient for liquid phase flow can be attributed to the bulk phase convection of liquid water through the expanded channels (Ren *et al.*, 2001). The increase may also be due to the stronger interactions between protons and liquid water molecules than the ones between protons and water vapour. Ren and Gottesfeld (2001) have ascribed the temperature dependence of the electro-osmotic drag coefficient to the change in proton transfer mechanism, which shifts with from the

Grotthuss mechanism at low temperatures to the *Vehicle* mechanism at high temperatures. The effect of equivalent weight on the electro-osmotic drag is also evident from their experimental investigations, which show that the drag coefficient increases with decrease in equivalent weight. A compelling reason for this can be the increase in the size of water solvated ionic clusters in PEMs of low equivalent weights, which favours proton movements (Hsu *et al.*, 1982).

The temperature dependent electro-osmotic drag coefficient of liquid water has been calculated using the correlation proposed by Weber *et al.* (2004a) which is based on the above mentioned experimental results and is given in equation (3.48). The temperature dependence is based on Arrhenius expression where the activation energy of 4 kJ is the amount of energy needed to break the hydrogen bond in a water equilibrated PEM (Weber *et al.*, 2004a).

$$\xi_L = 2.55 \exp\left[\frac{4000}{R}\left(\frac{1}{T_{ref}} - \frac{1}{T}\right)\right] \tag{3.48}$$

Note that equation (3.48) suggests that the value of the drag coefficient remains constant at a given temperature and was correlated from experimental data for the 1100 equivalent weight Nafion® series membrane.

3.4.2 Conductivity of a Nafion Membrane

As described earlier in the physical approach of percolation theory, the conductivity of the Nafion® is a strong function of water volume fraction inside the PEM. According to the percolation theory by Hsu *et al.* (1980), the ion conducting nature of Nafion® can be evident when it absorbs certain amount water vapour that helps in solvating the charged sites and setting the initial ion conducting pathways.

This threshold volume fraction of water for the membrane ionic conductivity is 0.06 for the vapour solvated membrane and corresponds to $\lambda_V \approx 2$. This amount of water remains fixed throughout the PEM and is sometimes termed as immobile or bound water (Futerko *et al.*, 1999). Hence, the conductivity of the PEM can realistically be computable once the membrane attains the percolation threshold. The expression for calculating ionic conductivity, given by Hsu *et al.* (1980) is,

$$\kappa = \kappa_o (f - f_0)^n , \tag{3.49}$$

where

κ_o = prefactor constant (for Nafion, $\kappa_o = 0.5$),

f = volume fraction of water in the PEM, $f = \dfrac{\lambda \overline{V}_0}{\overline{V}_m + \lambda \overline{V}_0}$,

f_0 = threshold volume fraction of water, and

n = critical exponent for percolative system, $n = 1.5$.

Equation (3.50) is a generalised form that calculates the ionic conductivity through both collapsed and expanded channels of the PEM (vapour and liquid phases). This expression for calculating the PEM ionic conductivity given by Weber *et al.* (2004a) holds good for both vapour and liquid phase ionic conductivities. In the case of liquid phase membrane conductivity, the water volume fraction varies to the power of 1.5 (Weber *et al.*, 2004a) and the expression for which is analogous to the percolation model equation (3.49). Equation (3.50) shows that the activation energy of 15 kJ is for both *Grotthuss* and *Vehicle* mechanisms, which are predominant modes of proton-water transport through vapour and liquid phases of the PEM respectively.

$$\kappa = \begin{Bmatrix} 0.5(f-0.06)^{1.5} \exp\left[\frac{15000}{R}\left(\frac{1}{T_{ref}}-\frac{1}{T}\right)\right] & f \le 0.45 \\ 0.5(0.39)^{1.5} \exp\left[\frac{15000}{R}\left(\frac{1}{T_{ref}}-\frac{1}{T}\right)\right] & f \ge 0.45 \end{Bmatrix}. \qquad (3.50)$$

The reason why equation (3.50) shows a constant conductivity beyond at fixed temperature beyond $f = 0.45$ can be explained based on the experimental studies by Gebel *et al.* (1993), which say that the conductivity of Nafion® remains constant between water volume fractions of $f \approx 0.45$ and $f = 0.8$, and that the PEM dissolves in water thereafter.

As the conductivity is a strong function of water content (through water volume fraction), it is higher in the PEM saturated with liquid water than in the one saturated with water vapour. Also, the membrane conductivity in both vapour and liquid phases increases with increasing temperature and decreasing equivalent weights. The reason for increasing conductivity with increase in temperature is somewhat similar to the explanation provided for the electro-osmotic drag coefficient: when the temperature increases, the *Vehicle* mechanism of proton-water transport through the bulk phase of liquid becomes a dominant mode of proton-water transport (Thampan *et al.*, 2000; Weber *et al.*, 2003).

3.4.3 Transport Coefficient

The transport coefficient differs considerably in vapour and liquid phase flows. It is mechanism dependent, which obeys Fick's law for water vapour through the ionic pathways (or collapsed channels) and Darcy's law for signifying the bulk phase hydraulic convection through the expanded channels.

3.4.3.1 Vapour Phase Transport Coefficient

For the vapour phase diffusion through the membrane, the transport coefficient in Fick's Law becomes a crucial parameter in determining the diffusion of water across the PEM. The transport coefficient α_V given by Weber *et al.* (2004a) is a function of the diffusion coefficient, concentration and mole fraction of water vapour:

$$\alpha_V = \frac{c_{0,V} D_{\mu_0}}{RT(1 - x_{0,V})}, \tag{3.51}$$

where

$c_{0,V}$ = the concentration of water [mol/cm^3],

D_{μ_0} = the diffusion coefficient of water vapour [cm^2/s],

$x_{0,V}$ = the mole fraction of water vapour,

and where

$$c_{0,V} = \frac{\lambda_V}{\bar{V}_m + \lambda \bar{V}}, \tag{3.52}$$

$$D_{\mu_0} = 1.8 \times 10^{-5} f_V \exp\left[\frac{20000}{R}\left(\frac{1}{T_{ref}} - \frac{1}{T}\right)\right], \text{ and} \tag{3.53}$$

$$x_{0,V} = \frac{\lambda_V}{\lambda_V + 1}. \tag{3.54}$$

3.4.3.2 Liquid Phase Transport Coefficient

For the bulk phase hydraulic flux through the expanded channels, the transport coefficient in equation (3.35) for Darcy's Law is a function of absolute permeability and temperature. The equation given by Weber's (2004a) model for calculating the liquid phase membrane transport coefficient is as follows:

$$\alpha_L = \frac{k_{sat}}{\mu \bar{V}_0^{\,2}} \left(\frac{f}{f_L} \right)^2 , \tag{3.55}$$

where

k_{sat} = absolute permeability [cm^2],

μ = viscosity of water [bar·s], and

f_L = volume fraction of water at $\lambda_L = 22$.

The absolute permeability, k_{sat}, of this expression becomes an important parameter governing the back water hydraulic flux across the PEM (from cathode to anode). The value of k_{sat} in the literature (Verbrugge *et al.*, 1990; Bernardi *et al.*, 1992; Weber *et al.*, 2004) varies by several of orders of magnitude. Further, it has been assumed that the value of k_{sat} can be fitted in the range between a maximum value of Verbrugge *et al.* (1990): $1.58\times10^{-13}\,cm^2$ and a minimum of Weber *et al.* (2004b): $4.7\times10^{-15}\,cm^2$. A value of $k_{sat} = 1.8\times10^{-14}$ cm^2 by Bernardi has been chosen for modelling. The value of k_{sat} strongly affects the back water convection of liquid water. In order to maintain the net water flux (electro-osmotic drag + water back diffusion or convection) across the PEM near to zero, a modification of this parameter (governing the liquid phase transport coefficient) may be required to manage a balance between the individual driving forces of water transport. A table summarising the membrane layer physico-chemical properties appearing in the membrane transport parameter equations is given in Appendix A.

In summary, the transport properties that are functions of the membrane water content seem to be very important for understanding the effect of individual driving

forces and their contribution towards the net fluxes of species (protons and water). Further, the variable membrane transport parameters might give an insight in understanding the influence of external design conditions on the mass transport within the membrane layer of a fuel cell.

3.5 PEM Swelling and Constraints

The architecture of the MEA has to ensure proper contacts between the PEM and porous transport layers, such a design is crucial for avoiding the mass transport and ohmic losses at active layers. A PEM is therefore hot pressed on either side with PTLs, but this type of design constrains the PEM from swelling by water uptake. A constrained PEM absorbs less water than a free-swelling one. As a result, the overall PEM volume decreases in comparison with a free-swelling one. The reduce in dimensions of a PEM increases the gradient in model equations (3.35) and (3.36) and the change in the membrane water content affects the corresponding water dependent transport properties. Hence, it is clear that the assumption of free-swelling membrane in a mathematical model can give a general understanding of mass transport but it does not represent the realistic situation inside a PEMFC.

The volume of a free-swelling membrane has been assumed to be a combination of constant additive molar volumes (Gebel *et al*., 1993) and can be written as (Weber *et al*., 2004c)

$$V_f = V_o\left(1+\frac{\hat{\lambda}_f \overline{V}_0}{\overline{V}_m}\right), \tag{3.56}$$

where

V_f = volume of a free-swelling membrane [cm^3],

V_o = volume of a dry membrane [cm^3], and

$\hat{\lambda}_f$ = average membrane water content of a free-swelling membrane.

The volume of a constrained PEM depends on the magnitude of the constraint factor, χ, the value of which shows the extent to which the PEM is constrained inside the MEA and ranges between 0 (unconstrained) and 1 (fully constrained). The magnitude of constraint (χ) on a PEM depends on the mechanical properties of the materials of the MEA and the extent to which the PEM is hydrated. It can be assessed by observing how the dimensions of the individual components of the MEA change with the impending stresses of the mechanical constraint. Weber *et al.* (2004c) showed that the constraint factor, χ, can be approximated by performing stress balances between the PEM and the PTLs. Their study showed that with a compressed PTL thickness of approximately 250μm (300μm of uncompressed PTL thickness) in an MEA, the magnitude of constraint on Nafion® 1100 *EW* series membranes was well below 50% (with different membrane thicknesses and humidification schemes). Introducing the constraint factor, χ, into equation (3.56) gives an expression for computing the volume of a constrained membrane.

$$V_{con} = V_0\left(1+\frac{\hat{\lambda}_f \overline{V_0}}{\overline{V_m}}(1-\chi)\right), \tag{3.57}$$

where

V_{con} = constrained membrane volume [cm^3],

χ = magnitude of constraint factor, and

$\hat{\lambda}_f$ = the average water content of a free-swelling membrane (unconstrained).

An approach set forth by Weber *et al.* (2004c) calculates the effect of swelling constraint on the PEM water content by stating that the chemical potential of water inside a free-swelling or constrained membrane equals that of surrounding water reservoir, this can be expressed as

$$\mu_0^f = \mu_0^{ext} = \mu_0^{con}, \tag{3.58}$$

where subscripts, *f, ext,* and *con* represent free-swelling, external and constrained respectively.

Based on the multicomponent thermodynamic framework of Meyers *et al.* (2002b), the water chemical potentials for free-swelling and constrained membranes can be written as (Weber *et al.*, 2004c)

$$\mu_0^f = \mu_0^* + RT \ln \hat{\lambda}_f EW + 2RT \sum_{k=1}^{n} E_{0,k}^* m_k \tag{3.59}$$

$$\mu_0^{con} = \mu_0^* + RT \ln \hat{\lambda}_{con} EW + 2RT \sum_{k=1}^{n} E_{0,k}^* m_k + \overline{V}_0 \tau \tag{3.60}$$

where

μ_0^* = a combination of reference states and constants,

m_k = molality of species *k* in the membrane [mol/g],

$E_{0,k}^*$ = the binary interaction parameter between water and species *k* [g/mol],

and

τ = dilatation stress parameter [bar].

The dilatation stress parameter, τ , can be expressed as

$$\tau = -K \ln\left(\frac{V_{con}}{V_f}\right), \tag{3.61}$$

where K is the bulk modulus (bar) of the membrane-water system (Hsu *et al.*, 1982; Weber *et al.*, 2004c), and is given as

$$K = \frac{Y}{3} = \frac{275}{3}\left(\frac{T_{ref}}{T}\right)\exp\left[-0.1655\left(\frac{\hat{\lambda}M_0}{EW} + \frac{1200 - EW}{100}\right)\right]\times 10 \qquad (3.62)$$

where

Y = Young's modulus of Nafion [bar], and

M_0 = molecular weight of water [g/mol].

This expression for bulk modulus of the membrane-water system is valid for temperatures below the glass transition temperatures of Nafion® ($T_g \approx 110°\text{C}$) but at higher temperatures ($T > 110°\text{C}$) it does not hold good and has to be modified.

The expressions of the water chemical potentials for free-swelling and constrained membranes (3.59) and (3.60) respectively are based on the assumptions that stress acts uniformly on the membrane, molalities of charged sites and protons, and binary interaction parameters are constant. The change in chemical potential of water from swollen to constrained states can be written by using these equations:

$$\Delta\mu_0 = RT\Delta\ln\hat{\lambda} + \overline{V}_0\tau = 0, \qquad (3.63)$$

From equation (3.63), the average water content of a constrained membrane can be written as

$$\hat{\lambda}_{con} = \hat{\lambda}_f \exp\left(-\frac{\overline{V}_0\tau}{RT}\right), \qquad (3.64)$$

Using equations (3.56), (3.57) and (3.64), the ratio of the constrained membrane average water content to the free-swelling one can be obtained and is expressed as

$$\frac{\hat{\lambda}_{con}}{\hat{\lambda}_f} = \left[\frac{\overline{V}_m + \overline{V}_0 (1-\chi)\hat{\lambda}_f}{\overline{V}_m + \overline{V}_0 \hat{\lambda}_f} \right]^{K\overline{V}_0 / RT} . \tag{3.65}$$

To utilise equation (3.65) in the swelling constraint model, the average water content of a free-swelling membrane must first be computed. The average water content value obtained by simulating the free-swelling membrane model can then be used in equation (3.65) for calculating the corresponding average water content value of a constrained membrane of volume, V_{con}.

Finally, it has to be noted that the change in the dimensions along the PEM thickness and transversal width also affect the driving forces (chemical potential or pressure gradient terms) in the governing equations (3.40) and (3.41). Hence, it is necessary to properly account for the variation in the dimensions of the membrane. The assumption of isotropic membrane swelling (membrane width in cross-the-channel direction) directions supports having a single expression for calculating the variation in the dimensions with membrane swelling (in thickness and transversal directions). Equation (3.66) is common for calculating swelling in PEM thickness or transversal width and can be used in the membrane model.

$$l_{con} = l_o \left(1 + \frac{\hat{\lambda}_f \overline{V}_0}{\overline{V}_m} (1-\chi) \right), \tag{3.66}$$

where

l_{con} = constrained membrane thickness or width [cm], and

l_o = dry membrane thickness or width [cm].

3.6 Summary

The mathematical framework described explains the PEM layer mass transport with wide-ranging humidification schemes. The membrane transport properties dependent on the membrane water content and the operating temperature provide a useful insight in explaining how the mass transport is affected by the PEM hydration state. Also, expressions used for calculating these have been based on strong experimental evidences. Further, as these properties are variable across the membrane, they are expected to provide good insight into the analysis for showing the anisotropic mass transport effects across the membrane. The practical aspects such as the PEM swelling and the corresponding limitations arising out of the membrane adjacent stress effects can now be effectively evaluated using the approach described in the preceding section.

4. ALGORITHM TO SIMULATE THE MEMBRANE MODEL

4.1 Introduction

The mathematical model described in the previous chapter must be simulated for observing the influence of the cathode half cell on the membrane layer mass transport. The computational algorithm developed here based on a finite volume method is a rigorous approach for solving the dependent variables (Φ, μ_0 or p_L) and bounding with the conservation laws in the PEM phase. A computer generated numerical model from this work is expected to be a handy tool for investigating the variation in the membrane transport properties with its hydration state and studying the anisotropic mass transport issues arising at the interface near the membrane-cathode half cell. The purpose of the current chapter is to describe the computational framework that simulates the membrane layer diffusion-hydraulic model bonded to a cathode half cell. The current chapter also aims at validating the transport model with the data available in the literature. Although validating a stand-alone membrane model is difficult unless it is embedded in a complete fuel cell model, the effort here tries to observe the variation in the PEM phase transport properties with assumed isotropic boundary conditions that result in a desired value of the net water flux per proton flux (β) value seen in literature.

4.2 Geometry of the Computational Domain

The computational domain framed in the current model is a cross-the channel slice of the PEM taken from a virtual MEA, Figure 4.1 shows the top view of the MEA, the gases (H_2 and O_2/air) flow perpendicular to the page. Since Figure 4.1 shows symmetry in flow field plates, only a half portion of the PEM was considered for studying the model (West *et al.*, 1996). The cross-the-channel domain in Figure 4.1 shows the channel to land variations of the flow field plates. As a result of this architecture, the anisotropic conditions would arise at the interfaces between various layers of the MEA. The motivation for choosing this two-dimensional geometrical framework is to investigate the effect of anisotropy in conditions at membrane-cathode PTL interface on the membrane water distribution and the water dependent membrane transport properties. It also gives a clear understanding of the local ionic current distribution.

From a unit cell modelling perspective, it is required that the processes in all the layers of the MEA must be simulated iteratively. As mentioned earlier, this is a limitation of a decoupled membrane model, which is capable of simulating the membrane mass transport based on specified boundary conditions at the membrane-electrode interfaces. Nevertheless, it is expected that such a framework can provide useful details of the variation in the membrane transport properties and related ohmic losses influenced by the specified boundary conditions along the catalyst layers.

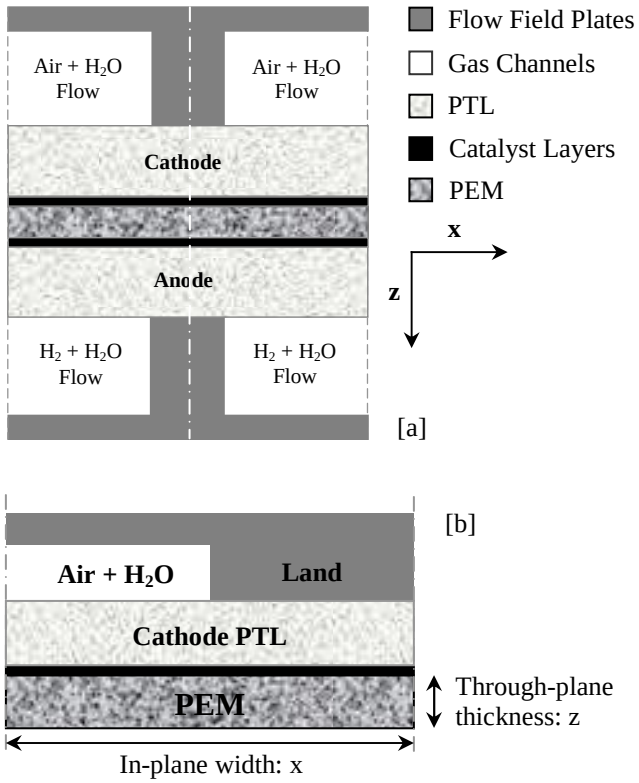

Figure 4.1: Schematic of a PEM fuel cell cross section

4.3 Boundary Conditions

The transport phenomena inside the membrane of a fuel cell depend on water and current boundary conditions distributed along the interfaces of the membrane modelling domain. The boundary conditions along the membrane-catalyst layer interface are essential for simulating the membrane model that is in contact with water vapour alone, or both vapour and liquid water. Based on the mode of water transport assumed, the water flux and the current conservation equations (3.40) and (3.41) are to be solved for finding the dependant variables (protonic potential, the chemical potential of water vapour or liquid water pressure) in the modelling domain.

Figure 4.2 shows the boundaries of the membrane computational domain. Although the catalyst and cathode (PTL) layers have not been modeled in this work,

they have been shown in the figure to avoid any confusion in depicting the cathode side boundary of the PEM. The potential (protonic) at the membrane-anode PTL interface is set to zero and the conditions at membrane-cathode PTL for ionic current densities, chemical potential of water vapour or liquid pressures are specified as described in the following sub sections.

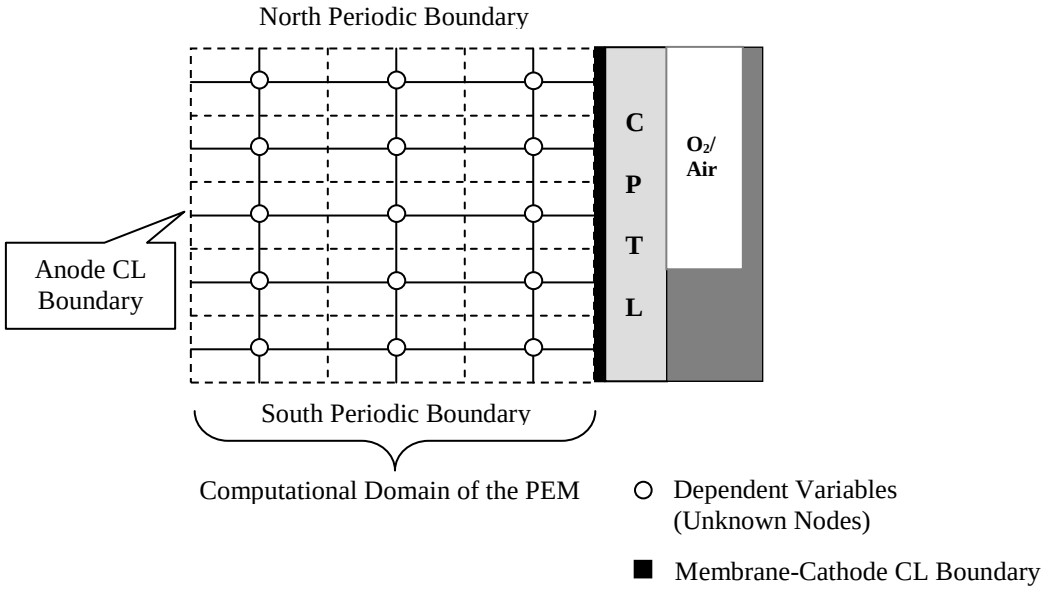

Figure 4.2: Schematic of a PEM computational grid with cathode half cell

4.3.1 Vapour Equilibrated Membrane

In the case of a PEM that is equilibrated with water vapour only, the fraction of expanded channels in the governing equations (3.40) and (3.41) becomes equal to zero and the corresponding equations reduce to that of equations (3.28) and (3.29). The boundary conditions that are required to simulate this case with the PEM phase model are as follows:

- The local ionic current densities ($\mathbf{i}$) along the membrane-cathode catalyst layer interface are required for solving the ionic current density conservation equation

(3.32) inside the membrane. These current densities can be obtained by solving the ionic current density equation in the cathode catalyst layer, which obeys simple Ohm's law (refer to Appendix A.1.3) and neglects proton-water interactions within the catalyst layer.

- The protonic potentials (Φ) at the anode-membrane interface were set equal to an arbitrary zero. This allows for calculating the potential drop across the membrane with specified ionic current densities along the membrane-cathode interface.
- Water flux conservation equation (3.31) (with S = 0, vapour equilibrated) inside the membrane has been solved based on the chemical potential gradient. The specified chemical potentials of water vapour at the membrane-catalyst layer boundaries were assumed to be in equilibrium with water vapour in the catalyst layer-electrodes.
- Gradients of dependent variables at the north and the south periodic boundaries in the in-plane direction of the computational domain (shown in Figure 4.2) were assumed equal to zero ($\nabla\Phi = 0$ and $\nabla\mu_0 = 0$) . This is because symmetry has been assumed to be in mass transport between the computational domain and a similar portion of it extending under the adjacent channel. The corresponding dependent variables at the periodic boundaries have been solved iteratively based on the adjacent interior nodes of the domain.

4.3.2 Membrane Adjacent to Saturated Vapour and Liquid Reservoirs

For the membrane in contact with both saturated water vapour (at anode interface) and liquid water at cathode PTL, the chemical potential of water vapour at the liquid water boundary has been set to the reference chemical potential. In this

case, the gradient of the chemical potential of water in the membrane is assumed to be in equilibrium with the gradient of liquid water pressure, as is given in equation (3.34). The current densities at the cathode interface and the protonic potentials at the anode interface have been set as described for the vapour equilibrated case in the preceding section. The water flux equation inside the membrane (3.41) has been solved based on the specified liquid water pressure gradient between the anode and the cathode. In order to reduce the complexities involved in the two-phase behaviour in the anode boundary, it has been assumed in this work that anode-membrane boundary is saturated with water vapour. Thus liquid water pressure at this boundary has been set equal to zero and the chemical potential of water vapour has been set to the reference chemical potential. Finally, the gradients of dependent variables ($\nabla\Phi$ and ∇p_L) at both the periodic boundaries at top and bottom of the computational domain were assumed equal to zero. This was because symmetry has been assumed in mass transport at the periodic boundaries and the dependent variables at corresponding control volume faces have been solved iteratively based on the interior nodes.

4.4 Computational Algorithm

The finite volume method (Patankar, 1980 and Versteeg *et al.*, 1995) has been adopted for solving the set of governing equations (3.40), (3.41), (3.31) and (3.32) of the mathematical model. This method conserves the molar fluxes in the control volumes surrounding the grid points in the membrane domain. It also bounds with overall molar flux conservation across the modelling region. All nodes are placed at the centres of the control volumes and the *boundary-on-face* approach has been chosen to discretise the control volumes at the boundaries. The mass transport model

described in the previous section has to be solved to calculate the molar fluxes of the species and to observe the variable entities at all nodal points in the two-dimensional, cross-the-channel computational domain of the membrane.

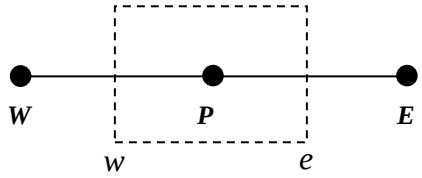

Figure 4.3: A one-dimensional control volume scheme

A control volume depicting the computation of single nodal point is shown in Figure 4.3. The conservation equations (3.31) and (3.32) of protons and water molecules in this method are integrated over this control volume surrounding the nodal point and solved in a sequential step manner by assuming that the nodal points surrounding the control volume as temporarily known variables and calculating for the dependent variable ***P***. Interfacial transport properties of the membrane at faces ***w*** and ***e*** are calculated based on an arithmetic mean of surrounding nodes.

A control volume approach for solving a two-dimensional computational grid has been implemented through a sequential method similar to the one described by Patankar (1980). As shown in Figure 4.4, the dependent variables (Φ, and μ_0 or p_L) at nodal points from $j = 2$ to N_x are assumed to be temporarily known with guessed values and the fluxes on the north and the south faces of control volumes at $j = 1$ and $k = 1$ to N_z are to be added to the source terms of the respective control volumes. The resulting set of discretised equations for all control volumes surrounding the dependent variables in a row at $j = 1$ were solved by a Tri-Diagonal Matrix Algorithm (TDMA). The remaining nodal points (dependent variables) in the subsequent rows

($j = 1$ to N_x) have been computed by utilising the calculated variables of the previous row and the guessed (or newly) calculated variables of the subsequent rows. Thereby all nodal points in the two-dimensional modelling domain have been solved by sweeping the row of discretisation (Line-by-line method) and implementing the procedure described above.

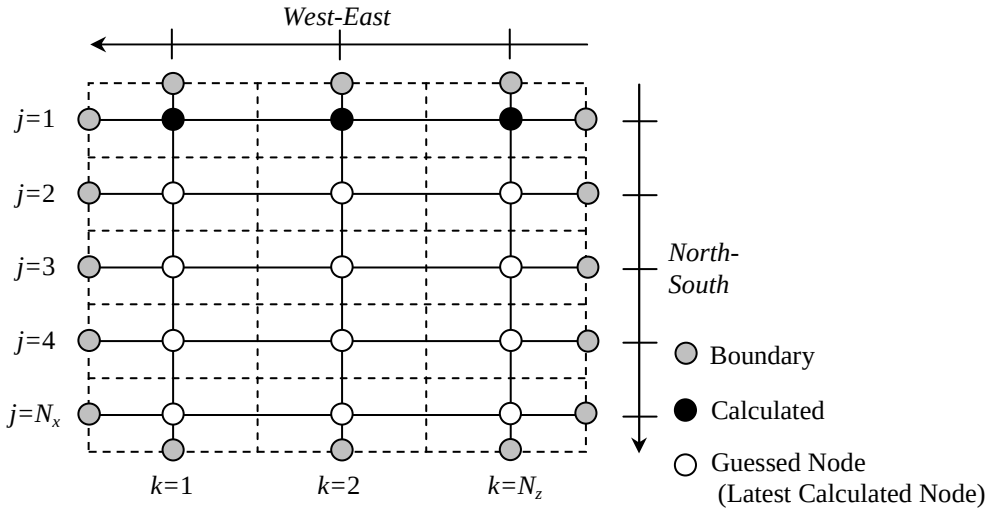

Figure 4.4: A two-dimensional control volume scheme

A Line-by-line method calculates the dependent variables in a row and sweeps through the remaining rows for calculating the rest of the dependent variables. This method of sweeping utilises the calculated variables of the previous row and the old or guessed variables of the subsequent rows and adds them to the source terms. The Alternate Direction Implicit (ADI) method (Hoffman *et al.*, 2000) involves sweeping rows alternatively between east-west direction and north-south direction. A detailed overview of finite volume method and the linearisation techniques for non-linear source terms can be found in Patankar (1980).

4.4.1 Algorithm to Compute Mass Transport across a Free-Swelling PEM

The computation procedure shown in Table 4.1 is based on a two-dimensional finite volume method with a line-by-line approach and is for simulating the transport inside a free-swelling PEM. In the case of a free-swelling membrane, it has been assumed that mechanical stresses acting through the PEM adjacent layers are negligible. Although this assumption is not truly realistic from the MEA design point of view, it is required for to simulate the transport inside a free-swelling membrane before accounting for the swelling constraint aspects (refer to section 3.6).

It should be mentioned that the membrane model has to account the realistic design effects of the fuel cell such as pinching the membrane from swelling along its in-plane width. In these circumstances where the membrane is fully constrained from swelling along its width, dry in-plane membrane width should be used in the calculation procedure. In this case, the membrane still allowed swelling freely along the direction of its through-plane thickness and the computation of its swollen thickness is based on equation (3.66). The algorithm for solving the mathematical model of a free-swelling PEM is also shown using flow charts in Figures 4.5a and 4.5b. All source codes developed in C++ were implemented on Microsoft® Visual Studio .Net. The computational algorithm for simulating the PEM layer mass transport model is grid independent, which allows for mesh refinement.

Table 4.1: Algorithm to compute mass transport across the PEM

Step 1	The dry dimensions of the PEM thickness and length are set. Boundary conditions at the membrane - catalyst layer (electrode) interfaces are specified. Average water content in the PEM is guessed. Run the initial grid function that specifies the guessed values at all nodes inside the PEM (pre-processing) required for solving the conservation equations (3.31) and (3.32).
Step 2	Calculate the swelling in the PEM thickness
Step 3	Calculate all the source terms and the PEM transport properties at all nodes
Step 4	Run PEMsolve function, which uses FVGrid and TDMA functions for calculating the dependent variables (Φ, μ_o or p_L) in equations (3.40) and (3.41) in the row.
Step 5	Sweep to the next row (j = 1 to N_x) in the 2D computational domain and repeat **Steps 2 to 5** till all nodes in the Grid are calculated (line-by-line approach).
Step 6	Calculate the mean of the Error in all calculated variables in the Grid, use a relaxation scheme to accelerate the convergence, update all guessed variables with the calculated ones.
Step 7	Check the convergence criterion for calculated variables ($10^{-6} \leq \text{Err} \leq 10^{-12}$), if the convergence criterion is not met, then repeat **Steps 3 to 7 (inclusive).** Else if the convergence criterion is met, then continue to **Step 8.**
Step 8	Calculate the average water content in the membrane and check for the Error between the calculated water content and the guessed one.
Step 9	Check for the convergence criterion of calculated average water content in the PEM. If the criterion is not met, repeat from **Steps 2 to 9 (inclusive).** If the criterion is met, continue to **Step 10**.
Step 10	Calculate PEM swelling along the across-the-channel width. Except for calculating thickness swelling again, perform the entire simulation to check for the change in dependent variables of the Grid, repeat from **Steps 3 to 8 (inclusive)**. If the PEM is pinched along it in-plane width, skip this step and perform post processing analysis.
Step 11	Check for the convergence criterion of calculated average water content. If the criterion is not met, repeat from **Steps 10 to 11.** Else, continue to **Step 12**.
Step 12	Check the convergence criteria for PEM swelling in all directions. If the criteria are not met, perform the entire simulation from **Step 2** with updated average water content. If the criteria are met, processing is completed. Run the Outdata for post-processing analysis.

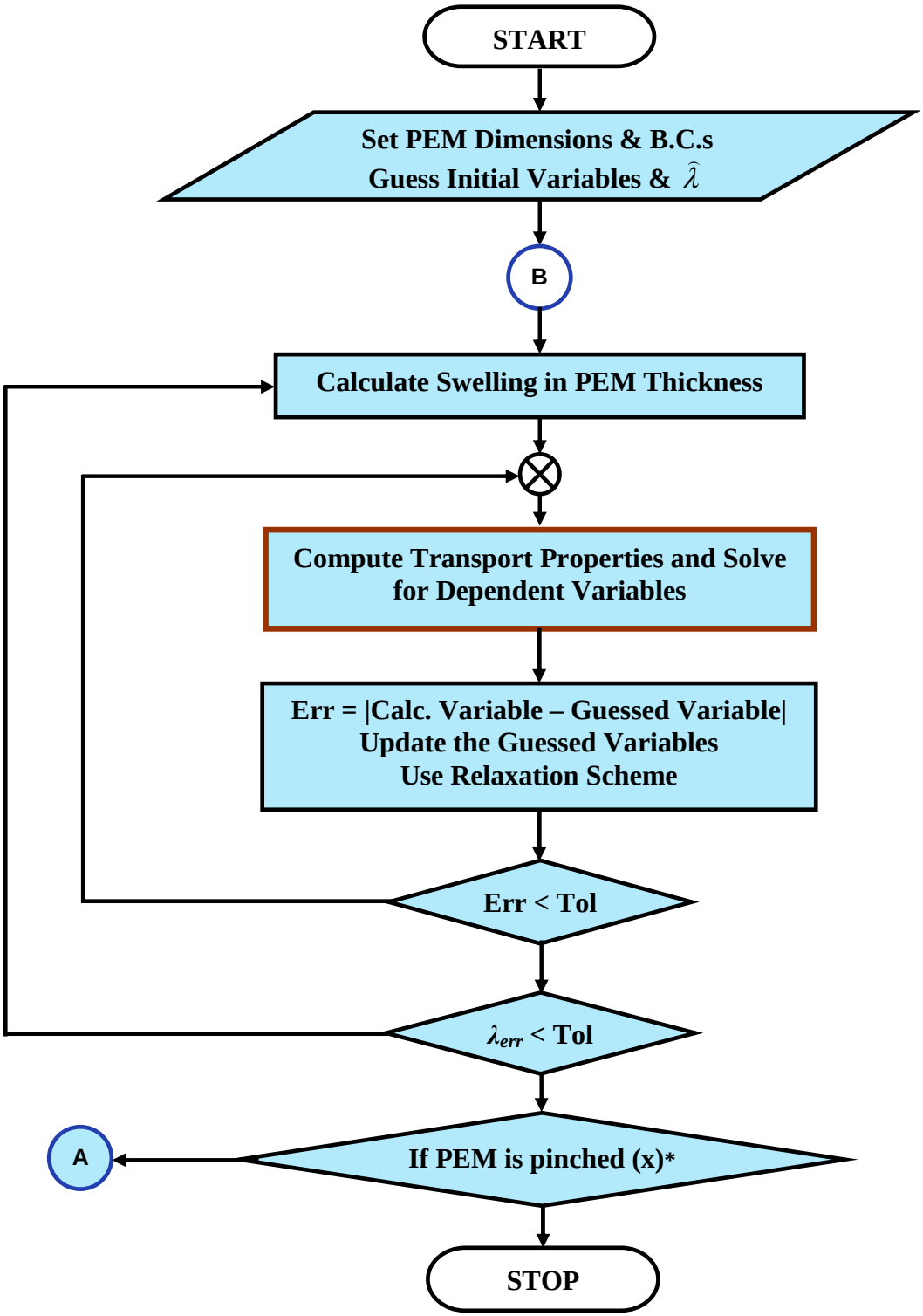

*: from swelling along in-plane width; Tol: $10^{-6} \leq \text{Err} \leq 10^{-12}$

Figure 4.5a: Computational algorithm to simulate mass transport across the PEM

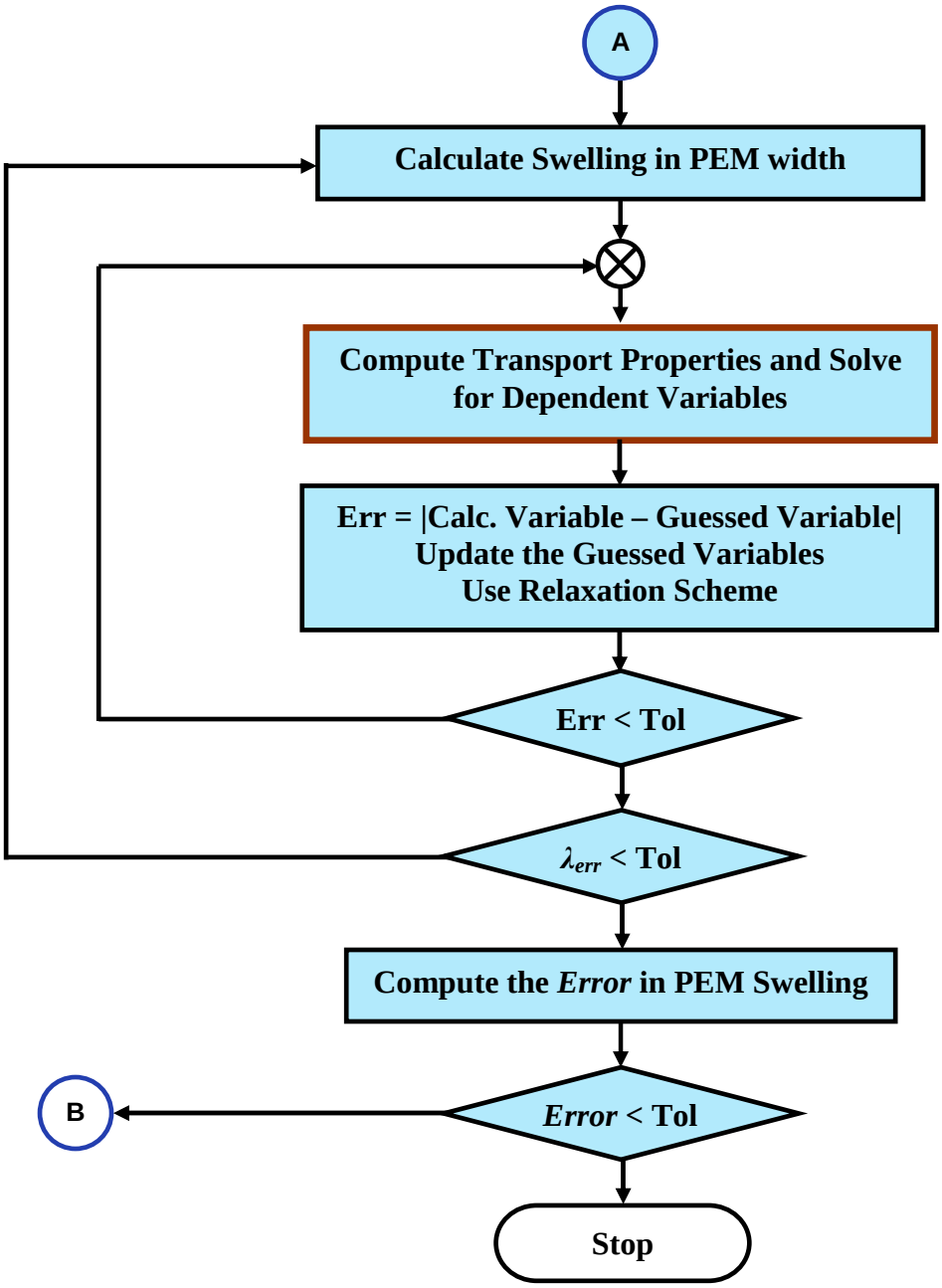

Figure 4.5b: Computational algorithm to simulate mass transport across the PEM (contd. from Figure 4.5a)

4.4.2 Algorithm to Compute Mass Transport across a Constrained PEM

Figure 4.6 shows the algorithm for computing the effect of swelling constraint on the PEM phase mass transport can be implemented by utilising the average water content $\hat{\lambda}$ value of a free-swelling membrane. This can be implemented by simulating the free-swelling membrane model.

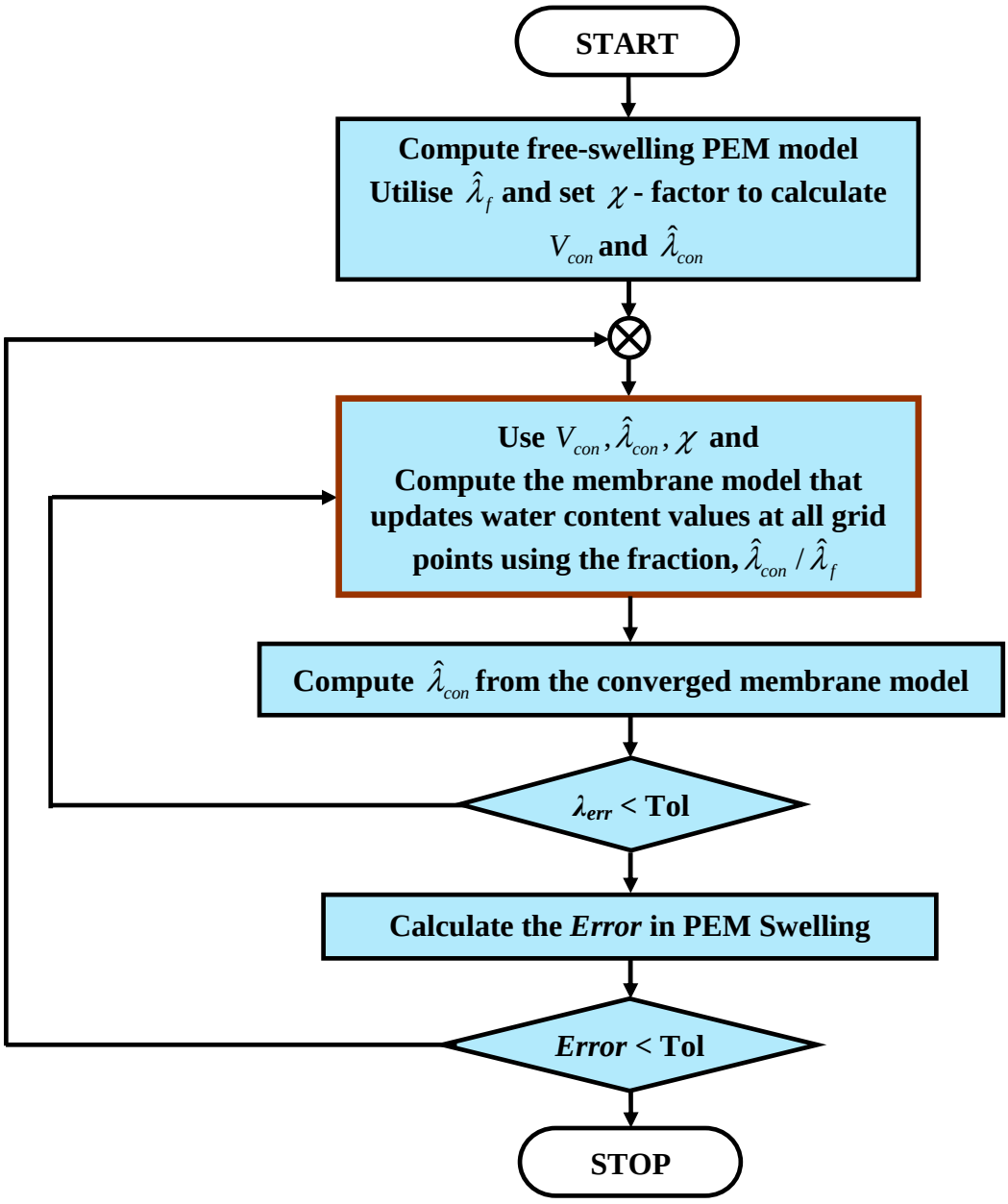

Figure 4.6: Algorithm to simulate the effect of constraint on the PEM

Equations (3.56), (3.57) and (3.65) given in section (3.5) can be used in the algorithm to compute the change in PEM dimensions and water content at a specified magnitude of constraint (χ) imposed on a free-swelling membrane. The model converges when the inner-loop's (membrane model) dependent variables and the outer-loop's swelling calculations both converge.

4.5 Computational Model Verification

Measuring the membrane water profile inside a PEMFC with lab scale techniques is practically not realistic. Hence, it is difficult to validate the computed membrane distribution. The results of the membrane layer mass transport model can be validated, in-part, if the simulations are performed with ideal conditions along the membrane-electrode boundaries. The required boundary conditions of the membrane model can be obtained either by simulating the processes in the porous transport and catalyst layers or by assuming values that are realistic and comparable with the experimental membrane conductivity data available in the literature. For the current portion of work, main aim has been set on describing the membrane transport properties at a desired water net water flux per proton flux (β) across the membrane. The functional dependence of the membrane conductivity and the electro-osmotic drag coefficient, based on the literature experimental evidences, were already been discussed in the chapter on modelling. As mentioned earlier, the results obtained from the computational model bound with the current density and water flux conservation equations (3.31) and (3.32). Hence, it can be understood that the computational procedure adopted in this work to simulate the membrane model is validated numerically. In essence, the purpose of this preliminary analysis is to illustrate the

variation in the membrane transport properties across vapour and liquid equilibrated membranes and compare them with the experimental details available in the literature.

Available data in the literature suggests that the net water flux per proton flux (β), which is a combination of all PEM phase water fluxes occurring due to various driving forces (electro-osmotic drag, diffusion or convection) remains close to zero (Zawodzinski *et al.*, 1993; Janssen *et al.*, 2001; Choi *et al.*, 2000). Based on this evidence, water boundary conditions along the membrane-catalyst layer boundaries have been specified and simulations have been performed at a constant cell current. The results obtained from such simulations with vapour and liquid equilibrated cases showing a desired net water flux per proton flux are presented and discussed in the subsequent sections.

4.5.1 Vapour Equilibrated Membrane

As sufficient hydration of the membrane is necessary to sustain its ion conducting properties, it is critical that the net water flux per proton flux (β) from anode to cathode side be balanced. When there are no pressure gradients across the membrane, water movement in the through-plane direction occurs as a result of electro-osmotic drag from anode to cathode and also because of the chemical potential gradient driven diffusion. In order to maintain a balance between these driving forces, all simulations have been performed to result with a desired β, calculated using the membrane model, given by equation (5.1).

$$\beta = \frac{\dfrac{1}{(n_x n_z)}\sum_{j}^{n_x}\sum_{k}^{n_z}\mathbf{N}_0(j,k)}{\dfrac{\dfrac{1}{(n_x n_z)}\sum_{j}^{n_x}\sum_{k}^{n_z}\mathbf{i}(j,k)}{F}} \tag{5.1}$$

Zawodzinski *et al.*, (1993a) showed that the net water flux per proton flux across a vapour equilibrated Nafion® 117 fuel cell membrane lies close to zero. The observed $\beta = 0.2$ from their fuel cell experimental study, at $80°C$, was obtained at cell current density of 0.5 A/cm^2 with saturated conditions at cathode and 1 bar gas pressure in either flow channels. Perhaps this could be the most compelling piece of evidence available for running stand alone membrane model simulations using forced membrane boundary condition data.

4.5.1.1 Membrane Water Content

In the case of a vapour equilibrated membrane, the partial pressures of water vapour can be used to calculate the chemical potentials of water vapour at the membrane-electrode boundaries. The model has been run to observe the variation in water content between the completely saturated cathode and the partially dry anode. In all simulations, the anode and cathode side membrane boundary conditions were specified to remain above the percolation threshold water content, $\lambda_V \geq 2$. Since the membrane mass transport model uses the Flory-Huggins thermodynamic model (Futerko *et al.*, 1999), the calculated membrane water content in the vapour phase varies between the limits of $\lambda_V = 2$ and $\lambda_V = 11$(saturation). The value of water content at saturation differs to some extent compared to an experimental value reported in the literature by Hinatsu *et al.* (1994), which revealed that at $80°C, \lambda_V \approx 9.2$.

Nevertheless, Flory-Huggins model is reasonably good in predicting the membrane water content at different temperatures (refer to Figure 3.2), which unlike most empirically fitted models (Springer *et al.*, 1991), allows for performing isothermal conductivity studies at different temperatures.

4.5.1.2 Membrane Ionic Conductivity

Figure 4.7 illustrates the ionic conductivity with respect to the position within the membrane. The water content and temperature dependency of Nafion 117 (acid and expanded form) ionic conductivity is evident from Figure 4.7, which shows a linear variation across the membrane, where conductivity increases from anode side to saturated cathode side. All simulations of the vapour equilibrated membrane were performed with uniform water boundary conditions at saturated cathode (RH 100 %) and anode (RH 96 %). The reference chemical potentials at different temperatures were calculated using the thermodynamic tables of Chase *et al.* (1986). The ionic current density in all simulations was maintained constant at 0.5 A/cm^2. It can be observed that the membrane conductivity has increased with temperature showing Arrhenius dependence. The experimental evidences available in the literature also reveal such behaviour (Sone *et al.*, 1996; Lehtinen *et al.*, 1998).

It has to be mentioned that membrane conductivity profiles shown in Figure 4.7 have been obtained through simulations with isotropic boundaries and the purpose of which was to validate the conductivity dependence on water sorption and temperature. In reality, flow field plate design configuration creates the anisotropy in the PEM phase water distribution and leads to distribution in local ionic conductivity of the PEM. A detailed overview of such aspects will be presented in the next chapter.

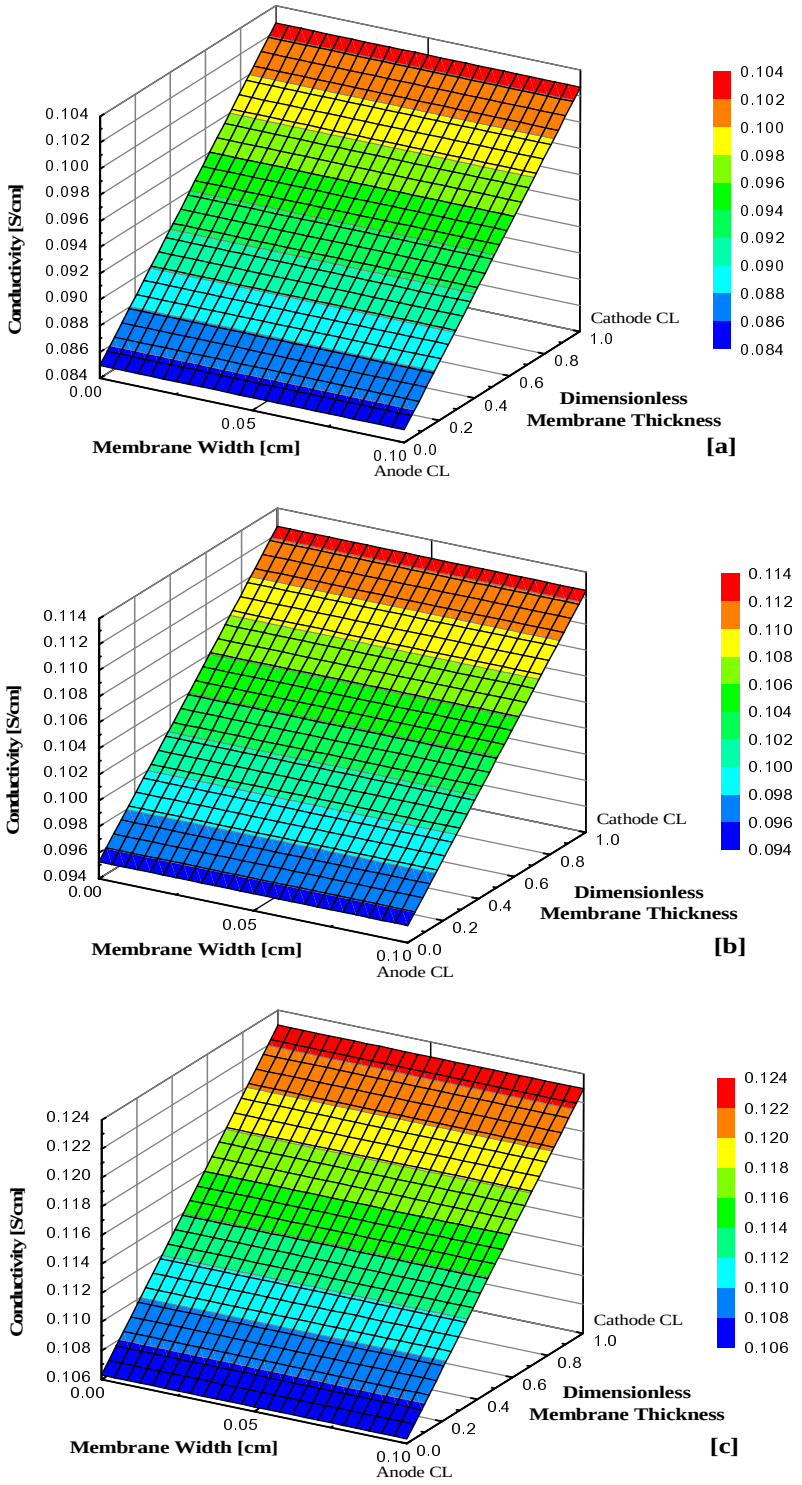

Figure 4.7: Membrane ionic conductivity [S/cm] for vapour equilibrated case with isotropic boundaries specified with saturated cathode and the anode RH of 96%, calculated $\beta \approx 0.2$ at 0.5 A/cm^2 and [a] 343.15 K, [b] 353.15 K, and [c] 363.15 K.

4.5.2 Conductivity of a Vapour-Liquid Equilibrated Membrane

The computational algorithm discussed in the previous section has been simulated at different inlet relative humidities along the membrane-electrode interfaces. A preliminary analysis was done by studying the variation in the membrane water distribution and the corresponding effects on the membrane transport properties. It was observed that in the case of a membrane that has been equilibrated with both vapour and liquid waters, membrane conductivity varies depending on water content and a phase transition occurs between the completely vapour and liquid saturated states. Hence, it obeys the capillary framework and explains Schroeder's paradox in polymer electrolyte membranes. In the case of a membrane that has been equilibrated with both vapour and liquid waters, the hydraulic liquid pressures along the cathode boundaries were set above 0.75 bar. Above this liquid pressure, the fraction of expanded channels will have a value of unity and the membrane will be fully saturated along the cathode side. On the other side, the anode-membrane interface has been equilibrated with saturated water vapour (water chemical potential at unit activity) and has no liquid water.

Figure 4.8 illustrates the ionic conductivity distribution inside vapour/liquid equilibrated Nafion® membranes. All simulations were performed at 353.15 K and a constant current density of 0.5 A/cm^2. It can be observed in Figure 4.8 that the conductivity varies depending on the portions of vapour or liquid phases within the PEM. The conductivity of liquid dominated majority portions of Nafion 115, $\kappa_L = 0.256$ S/cm in Figure 4.8 [b], matches closely with the experimental evidences found in the literature (Thampan *et al.*, 2000).

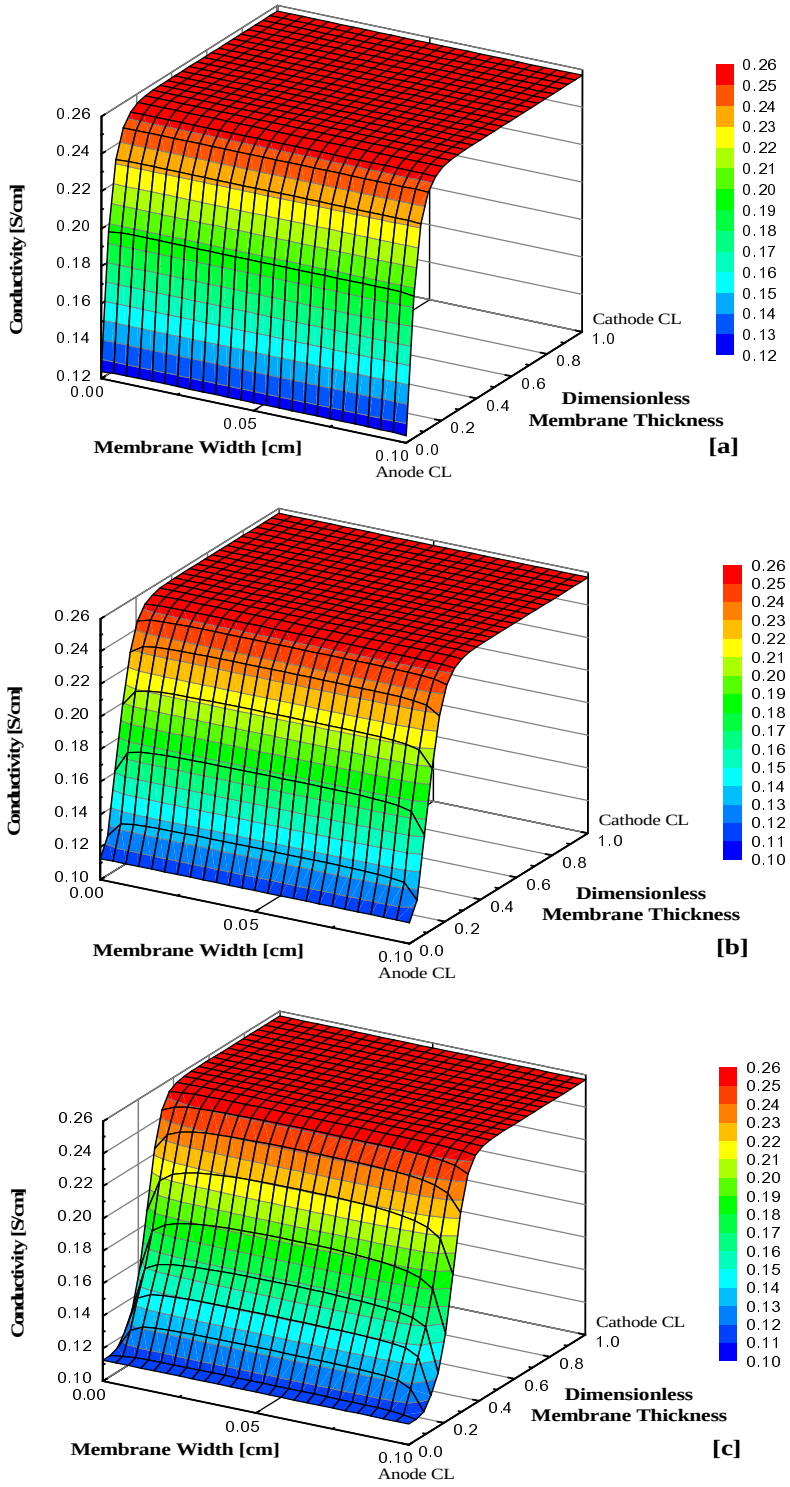

Figure 4.8: Membrane ionic conductivity [S/cm] for vapour/liquid equilibrated case with isotropic boundaries specified with fully saturated cathode ($p_L = 2$ bars and $\lambda_L = 22$) and the anode RH of 100%, at 0.5 A/cm^2 and 353.15 K, and [a] N 112, [b] N 115, and [c] N 117.

The membrane conductivity increases with the increase in liquid water content, which dominates the majority of the membrane portion in all three membrane cases (N 112, 115 and 117). This is because of the bulk phase hydraulic convection that occurs through the expanded channels showing the conductivity of 0.256 S/cm in portions where $\lambda_L = 22$. On the other hand, it is evident that proton conductivity through the collapsed channels (vapour phase) is less than that of liquid phase, which was found to be 0.112 S/cm in portions with $\lambda_V = 11$.

The portions of the membrane showing the conductivity between two extremes of vapour and liquid equilibrated states ($11 \le \lambda \le 22$) depend on the aspects such as the membrane thickness and current density. A thinner membrane promotes larger water back convection showing higher water contents in the majority of the membrane portions. This aspect can be observed from Figure 4.8[a] where the membrane is completely saturated with liquid water. An advantage of using thinner membranes in liquid humidified fuel cell system is that it helps avoiding anode drying and cathode flooding by promoting larger water back convection from cathode to anode. The ionic current density also influences the water distribution in the membrane because it affects the balance between the electro-osmotic drag and water back convection. Nonetheless, this issue is not elaborated further because of the current portion of the work does not model the cathode catalyst layer.

4.6 Overview of Computational Aspects and Limitations

The main advantage of choosing control volume method over general finite difference approaches is that it conserves the fluxes within the domain. In general, there are several computational aspects that influence the solution of the model. All

source terms were linearised using the techniques set forth by Patankar (1980) in order to avoid solutions diverging with negative values for always positive variables. Interfacial transport properties were calculated using a linear interpolation between the surrounding nodes. Although, this may not be an efficient method of calculating the interfacial properties (refer to Patankar 1980) in a non homogeneous systems, for a homogeneous PEM system, a linear interpolation for interfacial properties is a straightforward approach.

The algorithm for solving the membrane layer mass transport works with any number of arranged control volumes in the computational domain. Further, this issue becomes important when dealing with anisotropic boundaries, where the fluxes entering the domain vary along the in-plane width of the membrane-electrode interfaces. The results shown in the current chapter have been obtained with uniform grids of 50x50 (x, y) control volumes (CVs) using the isotropic boundary conditions. The simulations with anisotropic boundaries (as will be seen in the next chapter) have been performed with 40x100 CVs (x, y). The reason for choosing a specified number of control volumes in the modelling grid is dependent upon both converged solution and processing time of the computer model. A grid size was chosen such that increasing the number of control volumes would not significantly alter the resultant profiles. The simulation times of the membrane model with uniform grids increase significantly with the increase in the number of control volumes. Often these would depend on the specified boundary conditions and the physical aspects the domain such as membrane dimensions. All simulations involving a vapour equilibrated membrane, in this work, were performed with uniform grids. This would be appropriate because

the membrane swelling in the vapour phase is comparatively lesser than that of the liquid equilibrated membrane. The algorithm for liquid equilibrated mode is capable of computing the model with block uniform grids, variable, based on the local membrane water retention ($\hat{\lambda}_{local}$).

5. RESULTS AND DISCUSSION

5.1 Introduction

The purpose of this chapter is to discuss the results obtained from the study of anisotropic mass transport issues influenced by the conditions near the cathode side of the membrane. West *et al.* (1996) have modeled the mass transport in the membrane-cathode half-cell and investigated the influence of land spacing on the membrane water content and local current densities. They have revealed that the maximum in local current density would occur anywhere along the membrane-cathode catalyst layer and the location of which depends on the kinetic parameter of oxygen reduction reaction. However, the catalyst layer considered in their model is infinitely-thin. This might have over predicted the local current densities calculated in their study. The work by Sun *et al.* (2005b-c) has investigated the relevant anisotropic transport issues in a much more detailed way. The framework of Sun (2005a) is a cross-the-channel agglomerate model of the catalyst layer in the cathode half cell. They focused their study on determining the effects of channel-land aspect ratios on local current density distributions in the cathode catalyst and porous transport layers. However, their framework did not include modelling membrane layer transport issues. This limits their model's applicability in investigating the PEM layer mass transport issues, which are vital for gaining a thorough understanding of fuel cell design aspects from a membrane perspective.

The current work utilises the available membrane-cathode interfacial boundary condition data from Sun *et al.* (2005b-c) for simulating the two-dimensional membrane model and studying the relevant mass transport effects influenced by the external design factors. In essence, it studies the membrane layer variable entities such as water content, transport properties and local current densities with different schemes of flow field plate geometric parameters and NCOs. An additional part of the study focuses on investigating the effect of the through-plane membrane thickness on the ohmic resistance and also accounts for the realistic design limitations such as the effect of mechanical stress constraints on the membrane water uptake.

5.2 Simulation Parameters and Conditions for the Base Case

5.2.1 Geometric and Physical Parameters

A Nafion® 117 membrane has been considered in all base case simulations. The structure and geometry of the MEA does not allow the membrane to swell in all directions. In order to simplify this complexity, it has been assumed that a fuel cell assembled membrane is pinched from swelling in the direction of its in-plane width but was allowed to swell freely in the direction of its through-plane thickness. The dry thickness of Nafion® 117 is 7 mils and the in-plane width has been set equal to a combined value of half the width of a gas channel and half that of a land. The swelling of the PEM in the direction of its through-plane thickness is water dependent and the extent of which varies with simulation. The details of these have already been discussed in the chapter on modelling. Table 5.1 provides the geometric and physical details considered in base case simulations. The dimensions of the PEM adjoining the catalyst and porous transport layers and the flow field plate have been taken from the

work of Sun *et al.* (2005a). Although, these parameters have not directly been used in PEM layer transport model simulations, they have been included in Table 5.1 for clarity in illustrating the physical parameters influencing the boundary conditions used in base case simulations.

Table 5.1: Physical and geometric parameters used in base case simulations

Parameter	Value	Units	Reference
Channel width (half)	0.05	cm	a
Land width (half)	0.05	cm	a
PTL thickness	250	μm	a
Catalyst layer thickness	15	μm	a
Pt loading in catalyst layer	0.4	mg cm^{-2}	a
Through-plane membrane thickness	0.01778	cm	-
In-plane membrane width	0.1	cm	-
Membrane length	0.01	cm	-
Channel-land aspect ratio	1:1	-	-
Number of control volumes in the PEM	4000	-	-

a – Sun *et al.*, (2005b)

5.2.2 Operation and Transport Parameters

The operating temperature of the fuel cell was set to 353.15 K. The boundary data available at this temperature along the in-plane width of the membrane-cathode interface are based on the gas channel inlet air relative humidity of 50% and pressure of 1.519 bar (1.5 atm). The reference temperature and pressure of the membrane model were set equal to 303.15 K and 1 bar. A detailed overview of the transport parameters pertaining to the agglomerate catalyst layer and cathode PTL can be found in Sun *et al.* (2005a). The PEM phase transport parameters are variable and are dependent on the membrane water content and temperature. The details of these can

be found in Table 3.1. Table 5.2, given below, summarises the operating parameters considered for simulating the membrane model.

Table 5.2: Operating parameters common for all simulations

Parameter	Value	Units
Operating temperature	353.15	K
Cathode gas channel pressure	1.519	bar
Reference temperature	303.15	K
Reference pressure	1	bar
Relative humidity of air	50	%
Oxygen/nitrogen ratio	0.79/0.21	-

5.2.3 Nominal Cathode Overpotential

All simulations, including the base case, have been performed using appropriate boundary conditions available from the modelling work of Sun (2005a) at low, moderate and high nominal cathode overpotentials (NCOs). As given in equation (5.1), NCO is the difference between the solid phase electric potential and the electrolyte phase protonic potential at the agglomerate cathode catalyst active layer. The NCO includes the activation and electrolyte phase ohmic losses in the cathode catalyst layer but does not account for Ohmic losses across the PEM phase (Sun *et al.*, 2005a).

$$\mathrm{NCO} = \Phi_s - \Phi \tag{5.1}$$

where

Φ_s = solid phase electric potential of the cathode catalyst layer [V], and

Φ = electrolyte phase protonic potential in the cathode catalyst layer [V].

An operating fuel cell voltage which accounts for Ohmic losses across the PEM can be expressed by subtracting a specified NCO and simulated ohmic drops across the PEM from the reversible cell potential.

$$E_{cell} = E_{oc} - \text{NCO} - iR_m \tag{5.2}$$

It has to be mentioned that the cell voltage expressed using equation (5.2) does not account for any activation or ohmic losses in the anode. Hence, using it in fuel cell polarization studies may not be realistic. However, the voltage losses in the anode will be typically much smaller when compared to that in the membrane and cathode. Nonetheless, polarization studies using a stand-alone membrane component model can give some idea about the imminent membrane conductive resistances.

5.2.4 Water Balance across a Vapour Equilibrated Membrane

It is critical to account for the effects of an increase in the current density on the membrane water balance. The experimental observations by Choi *et al.* (2000) have revealed that, in the presence of concentration gradients across the PEM, the net water flux per proton flux (β) across Nafion® 115 membrane at 70°C decreases with the increase in current density. The reason for this has been ascribed to the increase in proton concentration at high current densities which hampers the net water drag from anode to cathode. It is also because of the increase in back water diffusion from cathode to anode at higher current densities. Interestingly, the effect of a reduction in β with the increase in current density beyond 200 mA/cm^2 has not been observed in their experimental study. A correlation, accounting all these factors, developed by Sun *et al.* (2005a) is given in equation (5.3).

$$\left.\begin{array}{ll} \beta = 46\mathrm{NCO}^2 - 31.52\mathrm{NCO} + 5.7 & (0.25\ \mathrm{V} \le \mathrm{NCO} \le 0.35\ \mathrm{V}) \\ \beta = 0.3 & (\mathrm{NCO} > 0.35\ \mathrm{V}) \\ \beta = 1 & (\mathrm{NCO} < 0.25\ \mathrm{V}) \end{array}\right\} \qquad (5.3)$$

Equation (5.3) may not be a good correlation for assuming the net water flux per proton flux across a PEM because the flux also depends on essential factors such as membrane thickness, humidification of inlet feed gases, and the cell operating temperature. Also, Weber *et al.* (2004b) have shown that β is sensitive to all of the above mentioned factors. Moreover, in the current work, the assumption of electroneutrality in the membrane contradicts with the observations by Choi *et al.* (2000). Nevertheless, in order to simplify and generalise the above mentioned complexities, it has been assumed that equation (5.3) is valid for a vapour equilibrated Nafion® 117 membrane. The above assumption can be reasonable for examining two-dimensional mass transport effects near the membrane-cathode catalyst layer interface. Moreover, even if a minute deviation in β occurs as a result of an increase or decrease in PEM phase water flux driving forces (electro-osmotic drag or back water diffusion), it would not alter the effect of cathode design parameters on the local current densities along the in-plane width of the membrane-cathode catalyst layer interface. Also, the fuel cell experimental data by Zawodzinski *et al.* (1993a) showed that net water flux per proton flux across Nafion® 117 membrane has a value of $\beta = 0.2$ at $i = 0.5$ A/cm^2. Based on which, it can be considered that $\beta = 0.3$ in this work is within reasonable limits.

5.3 General Issues Influencing the Anisotropy in Mass Transport

5.3.1 Effect of Channel-Land Ratio on the Membrane Water Distribution

It must be obvious that sufficient water uptake is necessary for the PEM to exhibit its proton conductive properties but it is also crucial that there occurs no excess water inundation at the membrane-catalyst layer interface. This is because the presence of excess stagnant water near the catalyst surface could adversely affect the reactant mass transport towards the active sites and hamper the performance of the electrochemical reaction. Accounting for these aspects at the cathode side of the membrane is critical because of the sluggishness of the oxygen reduction reaction. A factor that could lead to a distribution in the membrane water content is the external design aspect of flow field plates. Due to limitations in the design of flow field plates and the architecture of the MEA in a fuel cell, water removal from the regions of MEA under the land is difficult. In essence, a longer travelling path between the portion near the membrane-catalyst layer interface under the land and the exit of the gas channel suggests that water discharge through this path could be slow. As a consequence, there might be a possibility of back water diffusion into the membrane resulting from the increase in water concentration in the portions of the PTL under the land. The amount of water deposited at the membrane-cathode catalyst layer portion under the land might have an influence of the channel to land ratio. Thus, a good flow field plate design configuration is expected allow for better membrane water distribution at the least expense of water blockage near the membrane-catalyst layer interface.

Figure 5.1 shows the membrane water uptake from a base case simulation at 0.5 V NCO. It can be seen that a maximum in the membrane water uptake, along the in-plane width of the membrane-cathode catalyst layer interface, has occurred in the portion under the land. The higher water uptake in these portions can be attributed to a land width of 0.05 cm and channel to land aspect ratio of 1:1, which have not favoured water discharge into the gas channel.

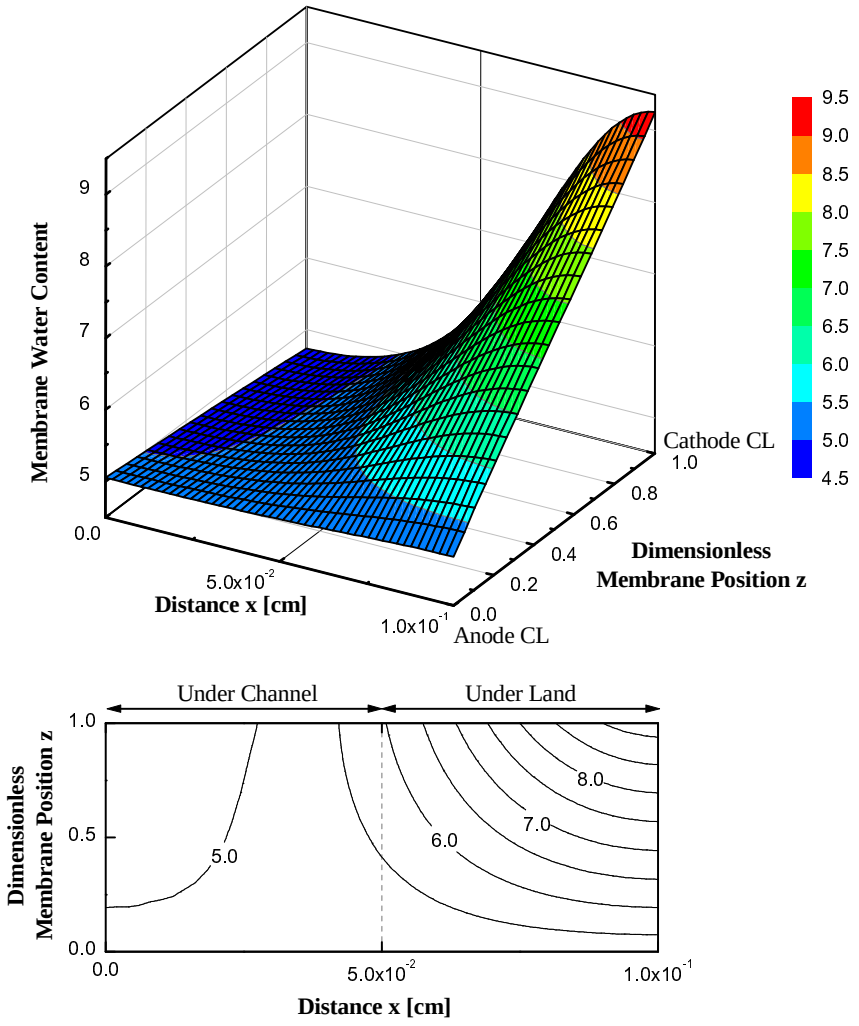

Figure 5.1: Membrane water content λ_V for the base case at 0.5 V NCO

Details of the membrane water content from base case simulations at 0.3 V, 0.5 V and 0.7 V NCOs are presented in Figure 5.2. It should be noted that the extent of the dimensionless membrane thickness is from 0 at the anode catalyst layer-membrane interface to 1 at the membrane-cathode catalyst layer interface.

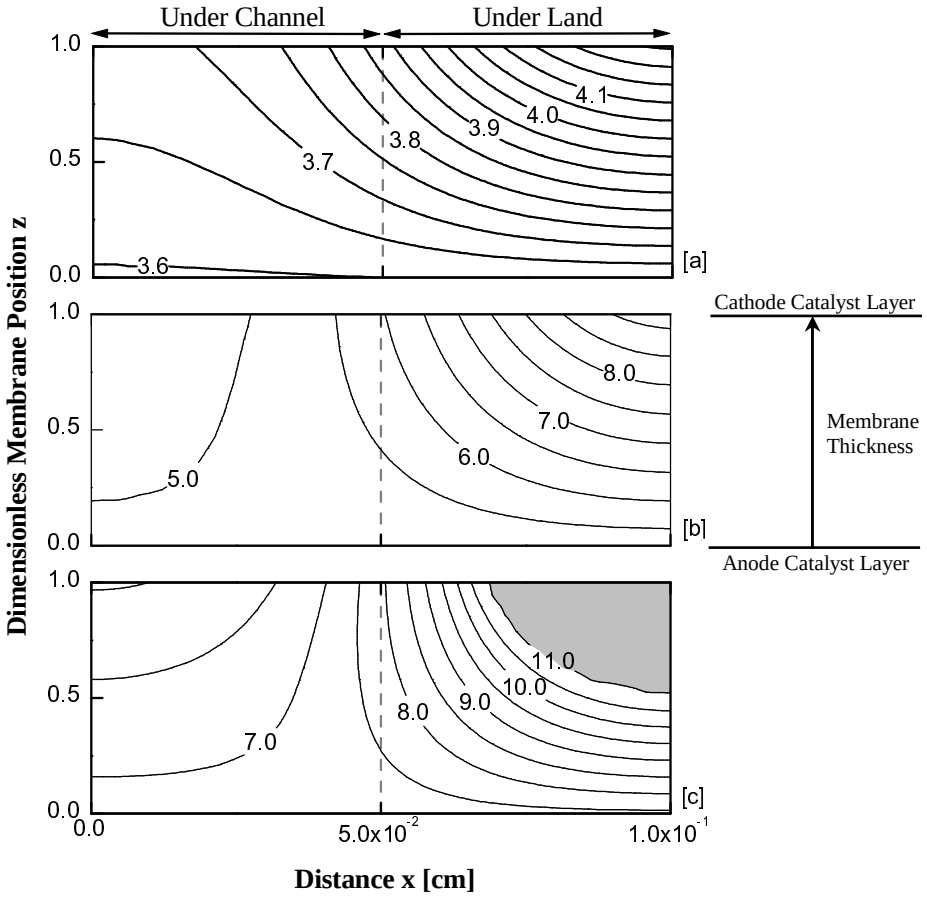

Figure 5.2: Membrane water content λ_V of base case simulations at [a] 0.3 V, [b] 0.5 V and [c] 0.7 V of NCOs. The shaded region under the land in [c] indicates saturated water vapour $(\lambda_V = 11.0)$ calculated based on Flory-Huggins model.

It can be observed from Figure 5.2 that the overall membrane water uptake has increased with NCO, the reason for which can be ascribed to the increase in water production at higher current densities. This effect had motivated back water diffusion from cathode to anode causing an increase in the membrane water uptake. Further, it

is evident from the results at low, moderate and high NCOs in Figure 5.2 that water has collected mainly in the portions under the land. This was because water discharge from these portions into the cathode gas channel might have been slower. In these circumstances, water vapour from a location under the land had to travel a longer distance (covering both half in-plane width and full thickness of PTL) into the cathode gas channel. Consequently, it can be expected that this process would be slower than the discharge of water directly from the portions under the channel. Although, these aspects may create a complex mass transport distribution in the PTL, they actually assist in hydrating the membrane. At a high NCO of 0.7 V, Figure 5.2 [c] shows that water vapour in the membrane is saturated in the portions ($\lambda_V = 11$) under the land and that in the portions under the channel is unsaturated. This distribution in water content across the membrane also affects its conductivity. On the other hand, in the PTL, complex mass transport processes involving water discharge from and oxygen transport towards portions under the land could affect local current densities. This latter effect has been observed in the corresponding simulation and will be elaborated further in the section on local current densities.

The impact of changing the channel to land aspect ratio is shown in Figures 5.3 and 5.4. The nature of the plots in Figure 5.3 with 2:1 channel to land ratio is similar to the ones of 1:1 channel to land aspect ratio (in Figure 5.2), where water uptake is more under the land regions than that under the channel. It should be observed that the overall membrane water uptake in each of the simulations at low, moderate and high NCOs has decreased when compared to corresponding cases of simulations with 1:1 channel to land aspect ratio.

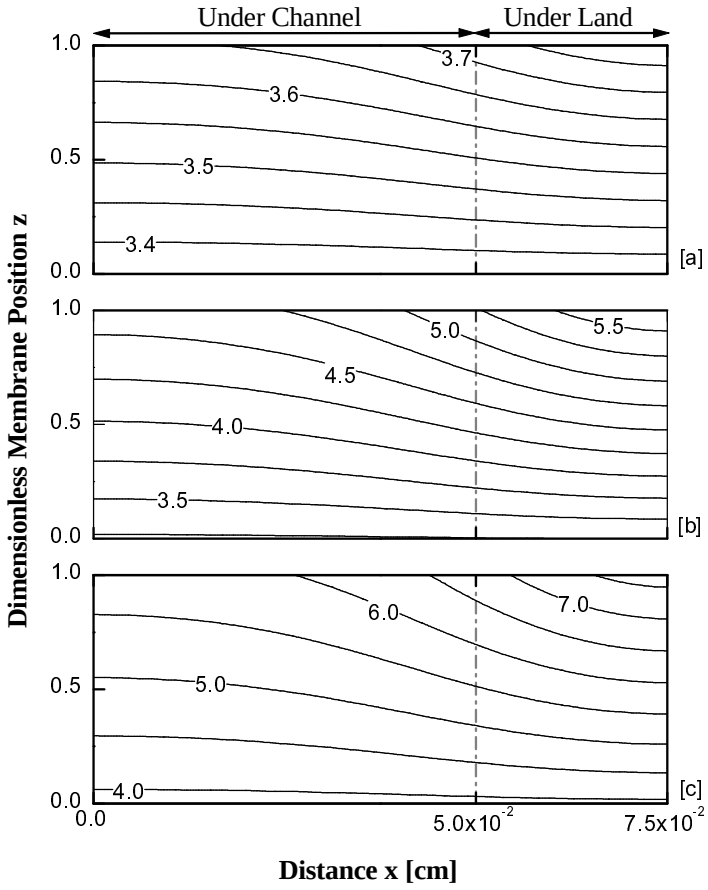

Figure 5.3: Membrane water content λ_V from simulations with channel to land aspect ratio of 2:1 at [a] 0.3 V, [b] 0.5 V and [c] 0.7 V of NCOs

Figure 5.3 presents the results obtained from simulations with conditions influenced by 2:1 channel to land ratio. A larger channel to land aspect ratio of 2:1 has led to a drop in water collection in the portions under the land. It can be expected this could lead to drop in membrane conductivity as well. This in turn implies that in the case with a 2:1 channel to land aspect ratio, water removal from regions under the land into the cathode gas channel has been effective when compared to the corresponding cases with 1:1 channel-land ratio.

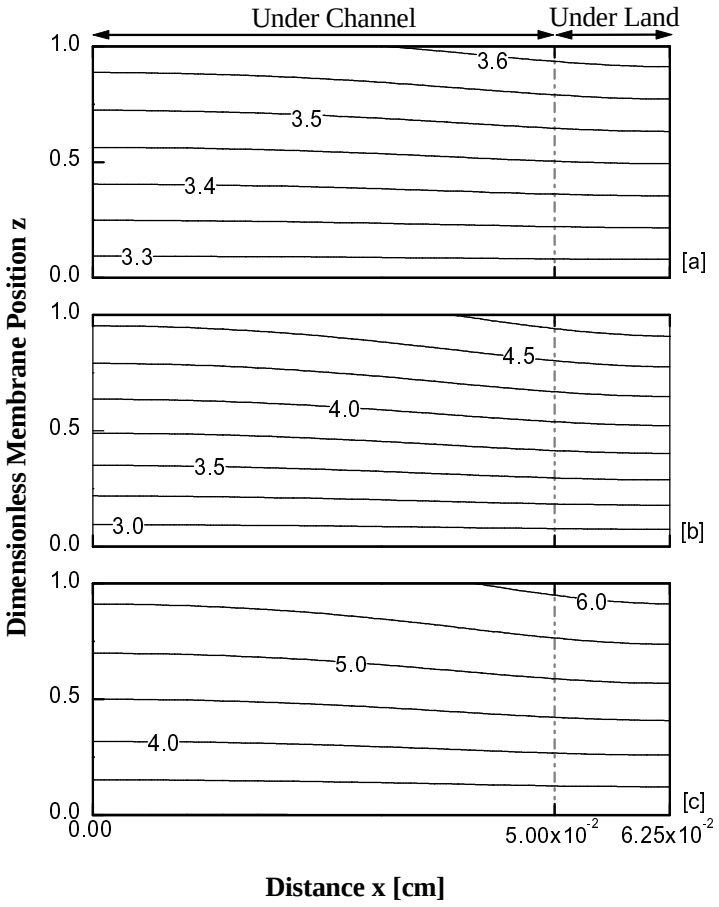

Figure 5.4: Membrane water content λ_V from simulations with channel to land aspect ratio of 4:1 at [a] 0.3 V, [b] 0.5 V and [c] 0.7 V of NCOs

Figure 5.4 shows that 4:1 channel to land aspect ratio has favoured decreasing the anisotropy in water distribution across the membrane width. The membrane water uptake in this case has decreased even further when compared to that with 2:1 channel to land aspect ratio. This potentially states that a larger channel to land ratio could be an option for increasing water discharge from portions under the land into cathode gas channel, but, on the other hand, it actually decreases the overall membrane conductivity, which is not desired for lessening the distributed PEM phase ohmic losses.

Table 5.3 summarises the simulated membrane water uptake data from each of the cases discussed in preceding paragraphs. It can be seen that the change in channel to land aspect ratio at 0.3 V NCO from the base case to 2:1 and 4:1 has slightly affected the average membrane water uptake, but at moderate and high NCOs, it significantly affected the corresponding values. The observed decrease in $\lambda_{V,avg}$ for 0.5 V NCO with 2:1 and 4:1 channel-land ratios has been 28 % and 34 % respectively. At 0.7 V NCO, the decrease in $\lambda_{V,avg}$ with 2:1 and 4:1 channel-land ratios was 35 % and 43 % respectively. Based on this observation, it can be inferred that increase in channel to land ratio has favoured water removal at moderate and high NCOs.

Table 5.3: Effect of channel to land ratio on the membrane water content

Channel-Land Ratio	NCO [V]	Membrane Water Content $\lambda_{V,avg}$
Base Case 1:1	0.3	3.76
	0.5	5.81
	0.7	8.08
2:1	0.3	3.53
	0.5	4.18
	0.7	5.25
4:1	0.3	3.48
	0.5	3.81
	0.7	4.56

5.3.2 Effect of Channel-Land Ratio on the Membrane Conductivity

Proton conductivity calculated based on the percolation theory exhibits its strong dependence on the membrane water content. The membrane conductivity profile shown in Figure 5.5 is from a base case simulation at 0.5 NCO. It should be

noted that the shape of this plot is similar to that of the corresponding base case membrane water distribution shown in Figure 5.1. Again, due to uneven membrane hydration, the ionic conductivity of the PEM phase is not uniform along its in-plane width near the cathode catalyst layer. The portion of the membrane under the land is more conductive than that under the channel.

The PEM phase conductivity distributions from simulations at low, moderate and high NCOs are shown in Figure 5.6. It can be seen that, in all three cases, the membrane conductivity in the portion under the land is greater than that under the channel. Further, Figure 5.6 [c] shows that conductivity of the portion of membrane saturated with water vapour under the land, near cathode catalyst layer, has a value of 0.11 S/cm. It has to be mentioned that conductivity cannot increase further until liquid water formation occurs. However, these effects have not been accounted in this study.

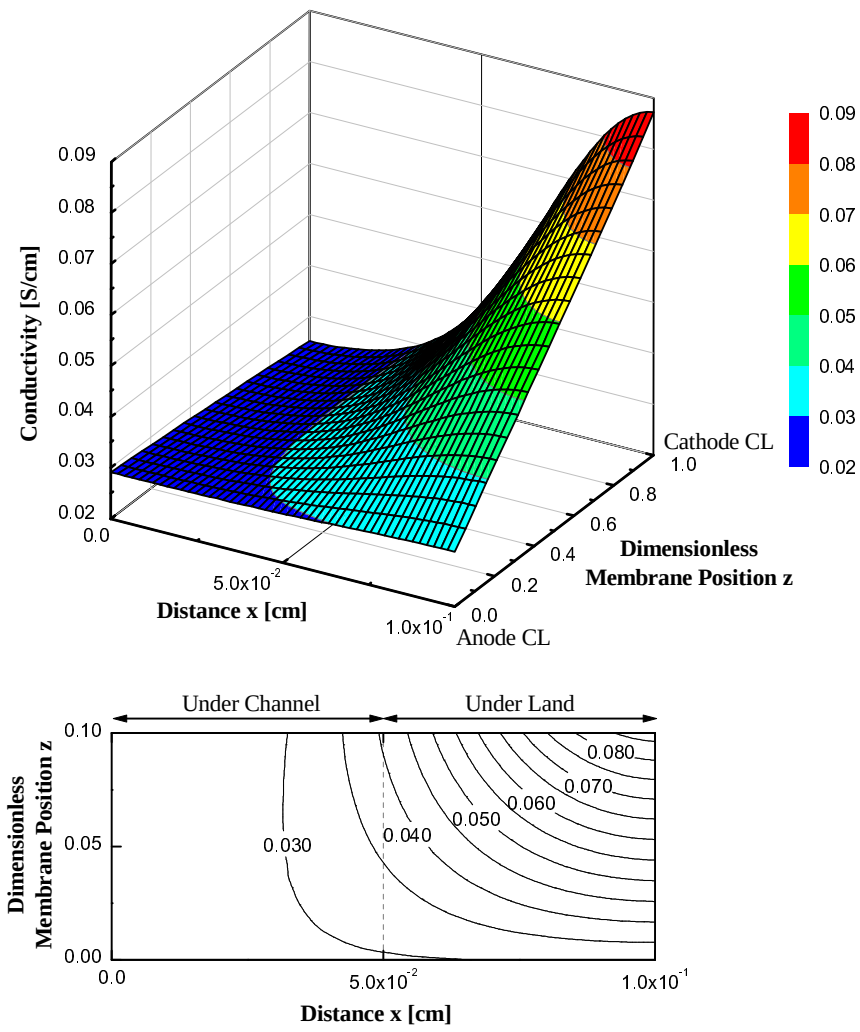

Figure 5.5: Membrane conductivity κ_V [S/cm] from the base case simulation at 0.5 V NCO

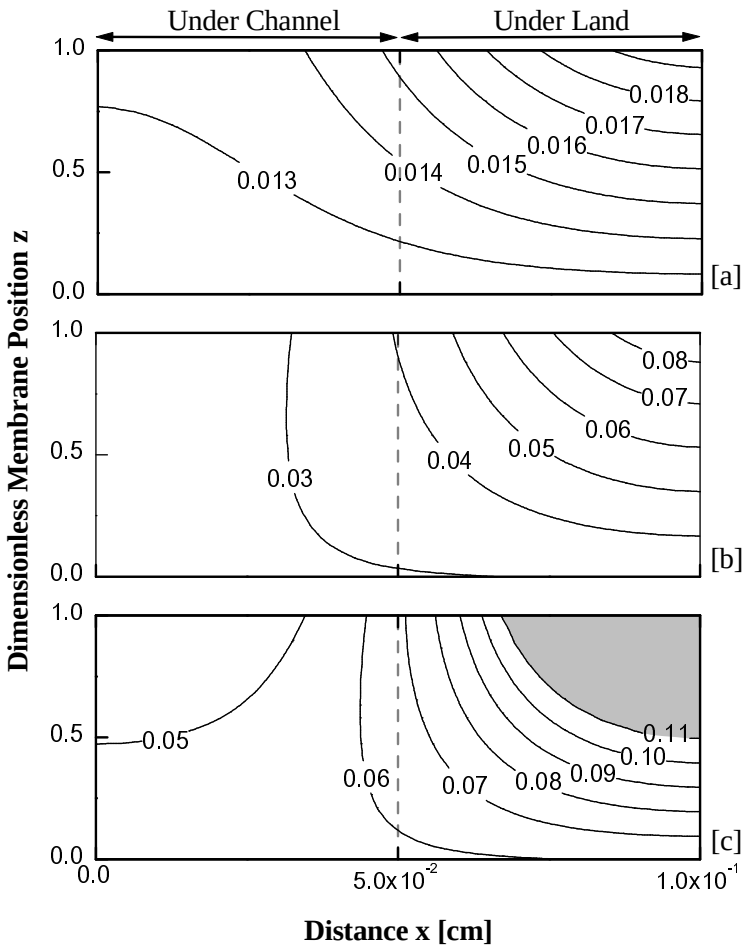

Figure 5.6: Membrane conductivity κ_V [S/cm] from base case simulations using boundary conditions at [a] 0.3 V, [b] 0.5 V and [c] 0.7 V of NCOs

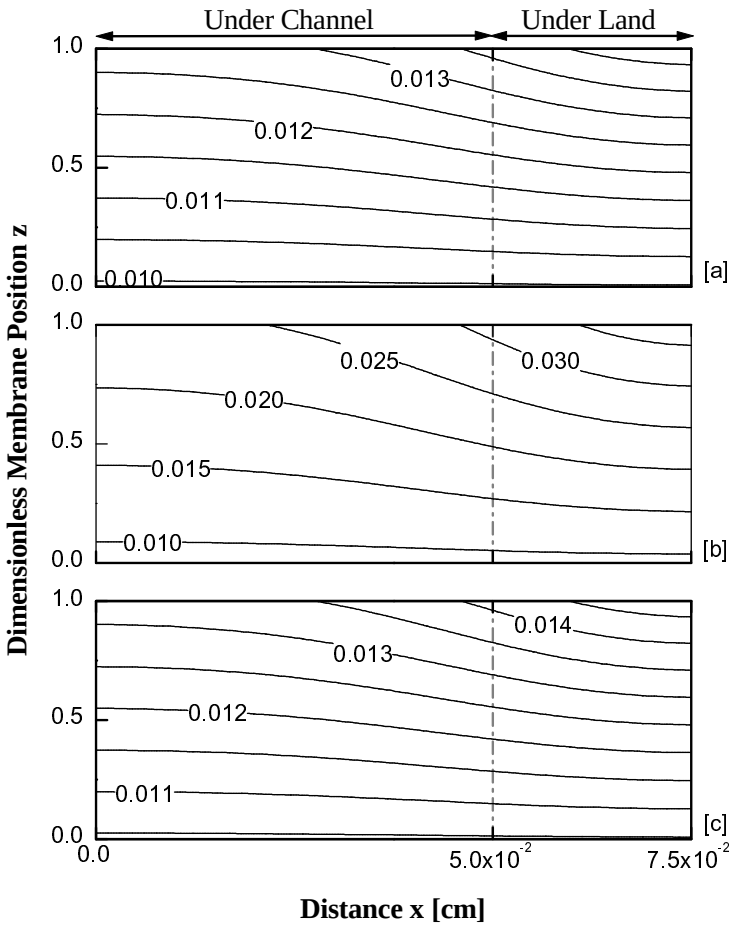

Figure 5.7: Membrane conductivity κ_V [S/cm] from simulations with 2:1 channel to land aspect ratio at [a] 0.3 V, [b] 0.5 V and [c] 0.7 V of NCOs

The effects of increasing the channel to land ratio on the membrane conductivity can be seen from Figures 5.7 and 5.8. It has to be observed that conductivity contours, in all three cases, have been smoothed to a certain extent when compared with those from the base case simulations. Increasing the channel to land ratio to 2:1 and 4:1 has led to the decrease in the anisotropy of conductivity but the overall membrane conductivity has also substantially reduced, the reason for which is the decrease in the membrane water content. The latter effect of the decrease in the

membrane conductivity with the increase in channel to land ratio might not be favourable for the membrane performance at higher current densities. The details of these can be found from Table 5.4 in the following section analysing current density distributions.

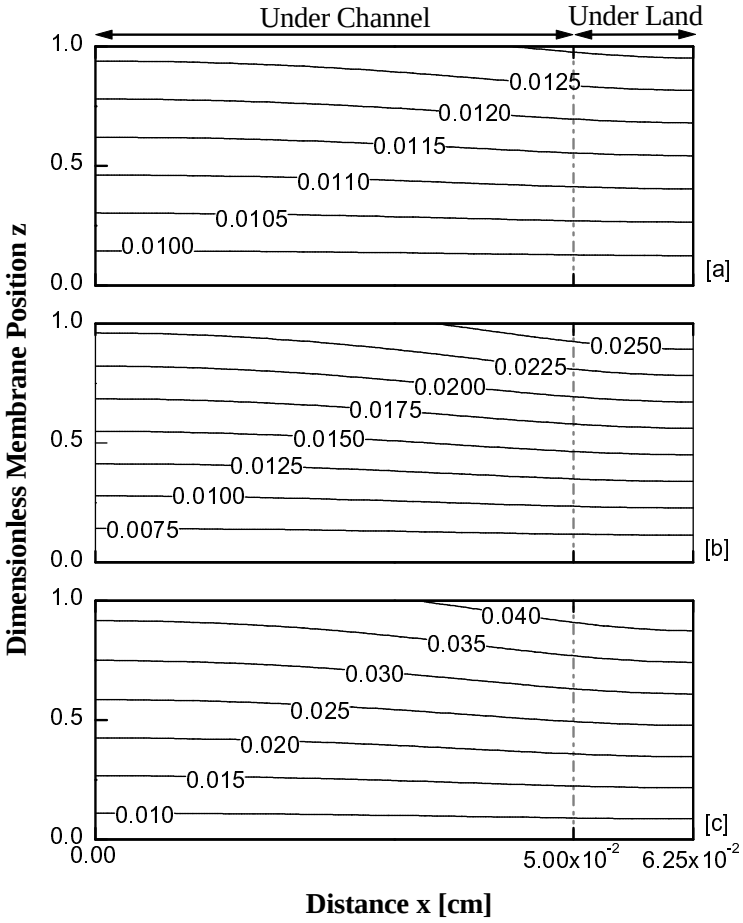

Figure 5.8: Membrane conductivity κ_V [S/cm] from simulations with 4:1 channel to land aspect ratio at [a] 0.3 V, [b] 0.5 V and [c] 0.7 V of NCOs

5.3.3 Effect of Channel-Land Ratio on the Current Density Distribution

The current density deviates along the in-plane width of the membrane-catalyst layer, the extent of which depends on the mass transport effects impacting the oxygen reduction reaction. The local ionic current density distribution across the membrane based on a specified NCO is expected to provide useful details for ascertaining the local ohmic loss distribution. The factors influencing the local current density distribution in the two dimensional membrane model have been examined and discussed below.

Figure 5.9 shows the through-plane local ionic current density distribution inside the membrane from a base case simulation at 0.5 V NCO. The highest local current density along the PEM/cathode interface can be observed midway along the membrane-cathode catalyst layer interface. This has been the case because the current density boundary conditions at these portions were favoured by the efficient transport of all reacting species (oxygen, protons and electrons) of oxygen reduction reaction (Sun *et al.*, 2005). The reason for the observed greater local current densities along the anode/PEM interface is that the dependent variables of two-dimensional control volumes in those regions are more influenced by the surrounding nodes other than the ones at the boundary.

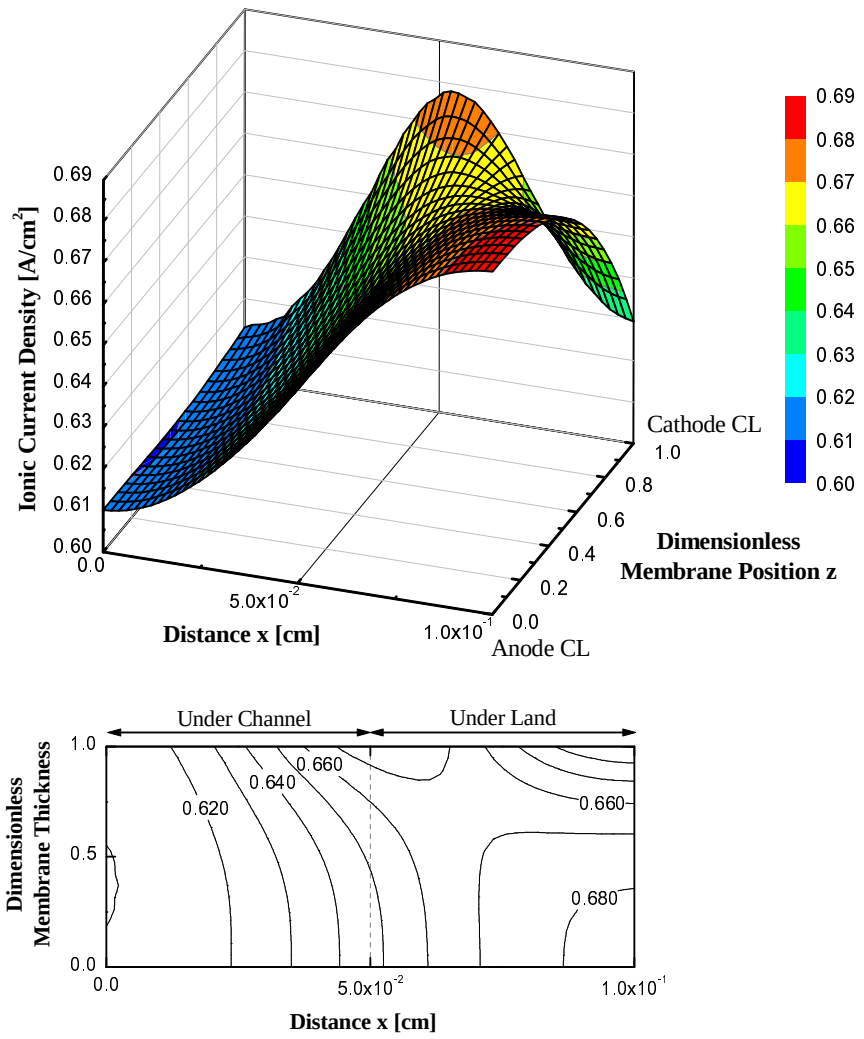

Figure 5.9: Through-plane ionic current density, i [A/cm^2] distribution across the PEM from a base case simulation at 0.5 V NCO

It is interesting to find from Figure 5.6 [b] and from Figure 5.9 (and from the same plot in Figure 5.10 [b]), that water concentrated portions of the membrane under the land have shown higher proton conductivities but the current densities observed in these portions were not higher. In these circumstances, one can expect less ohmic losses than that occur in the low conductivity/high current portions of the membrane under the channel.

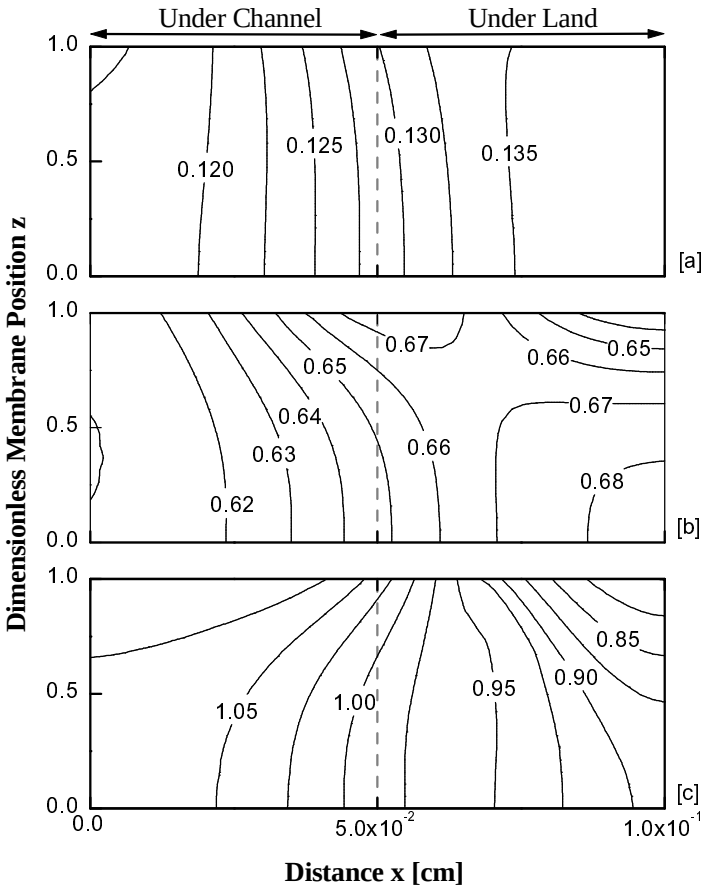

Figure 5.10: Through-plane ionic current density i [A/cm^2] from base case simulations at [a] 0.3 V, [b] 0.5 V and [c] 0.7 V of NCOs

The base case simulation at a low NCO of 0.3 V has resulted in showing interesting current density profiles. Figure 5.10 [a] shows higher local current densities in the relatively more conductive portions of the membrane under the land. At the same time, it has to be mentioned that cathode (PTL) mass transport factors such as oxygen diffusion towards portions under the land might not have been a rate limiting factor for the oxygen reduction reaction (Sun *et al.*, 2005a). This implies that the base case flow field design has forced the higher current densities through higher conductive portions of the membrane under the land. Based on the observed

phenomena, one can anticipate that the resulting situation might not significantly impact creating anisotropy in the membrane performance. This topic will be elaborated further in the section on local ohmic losses.

The ionic current density distribution does not entirely depend on the PEM phase conductivity but is also governed by mass transport effects in the cathode. It can be seen from Figure 5.2 [c] and from Figure 5.10 [c] that these effects become critical at higher current densities (at 0.7 V NCO) and are influenced by the design pattern of channel to land aspect ratio. It can be observed that the maximum local current density in the membrane has shifted from the portion under the land towards that under the channel where the membrane conductivity has been relatively lower than that under the land. This has been the case because the simulation (with boundary conditions at high NCO) has forced the ionic current to flow through relatively less conductive portions of the membrane under the channel. This could aggravate the PEM phase conductive losses. The reason for this forcing circumstance of ionic current density boundary conditions under the channel is the faster oxygen reduction reaction (at 0.7 V NCO). On the other hand, boundary conditions showing relatively less current density in the portion under the land might have been because of the poorer oxygen reduction reaction caused by the mass transport limitations of oxygen in the cathode (Sun *et al.*, 2005a).

It can be determined from Figure 5.2 [c] that at a higher NCO of 0.7 V, the presence of saturated water vapour along the in-plane width of membrane-cathode interface under the land has not resulted in improving the local ionic current densities. This is because the boundary conditions influencing the current densities are affected

by the mass transport limitations in the PTL. Firstly, the discharge of saturated water vapour into the cathode gas channel will not be favoured by a small channel to land aspect ratio (1:1). Secondly, oxygen scarcity in these portions could have occurred because it has to travel a longer distance from gas channel inlet towards catalyst layer portions under the land. On the contrary, the higher current densities exhibited in less conductive portions under the channel is because the boundary conditions are influenced by the factors of faster oxygen diffusion and water discharge through shorter paths of transport between gas channel and membrane-catalyst layer interfacial portions. As a result, one can expect the distribution in the membrane performance.

As a whole, the results from base case simulations in Figure 5.10 suggest that distribution in the ionic current density, influenced by the cathode side boundary conditions, could force the membrane to conduct protons even through less conductive portions, which could indeed result in uneven phase potential losses. At higher current densities, this issue becomes critical and causes more potential drop in less conductive portions of the membrane under the channel. This issue is evident from Figure 5.10a [c], which illustrates the PEM phase potential from base case simulations. Though potential gradient across the membrane causes the protons to migrate from the regions of high potential (anode) to the regions of low potential (cathode), it was observed that the potential drops in the regions of low water concentrations where ionic conductivity becomes difficult.

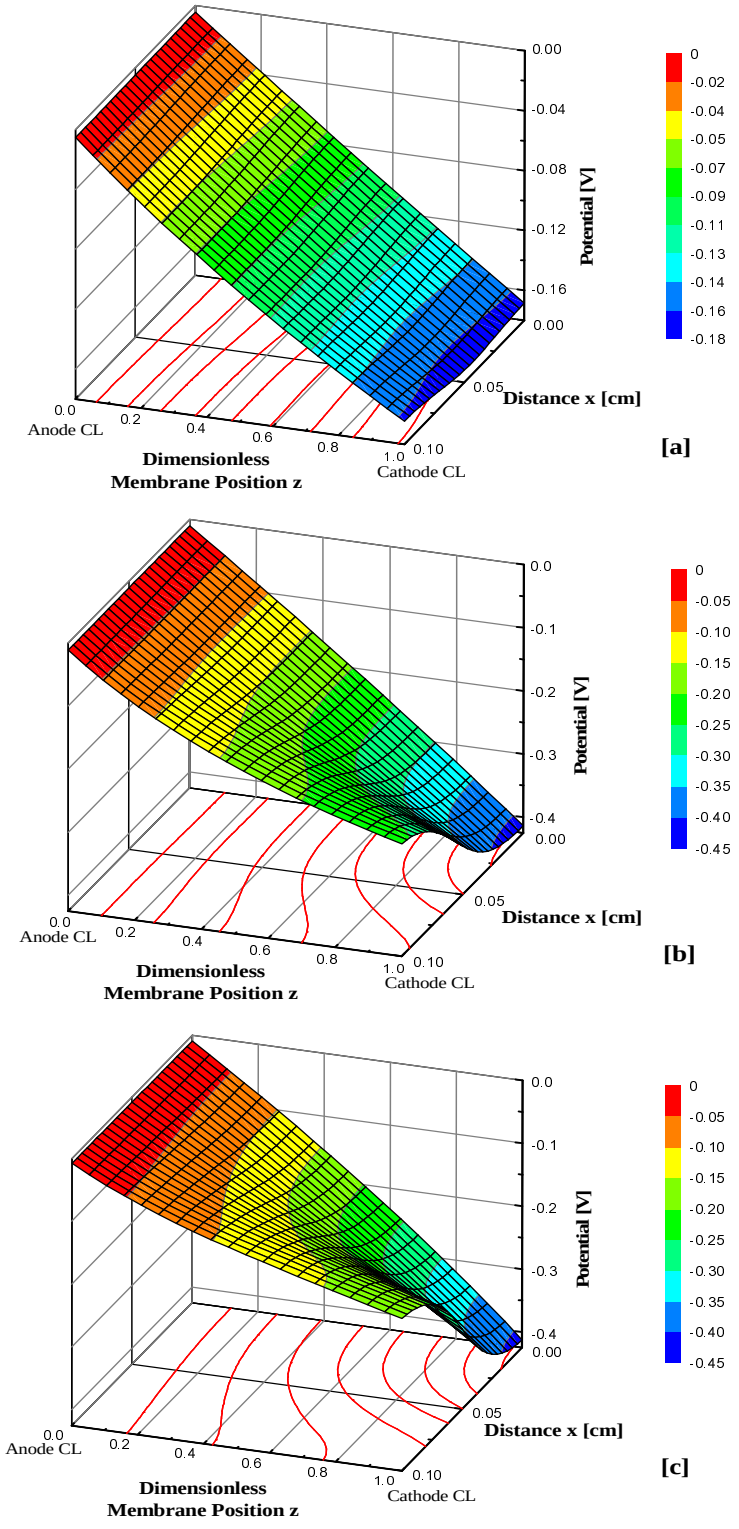

Figure 5.11: The protonic potential [V] across the membrane from base case simulations at [a] 0.3 V NCO, [b] 0.5 V NCO and [c] 0.7 V NCO. Membrane width is from 0 – 0.05 cm (under the channel) and 0.05 - 0.1 cm (under the land).

Figure 5.12 shows the results obtained from simulations using boundary conditions with a 2:1 channel to land ratio. It is observed that at low and moderate NCOs higher local current densities in the portions of the membrane near the cathode catalyst layer interface under the land coincide with the regions of high conductivity. This implies a more efficient utilisation of the membrane and consequently, it can be expected that ohmic losses in these regions would be lower than that under the channel, as will be discussed in section 5.3.4.

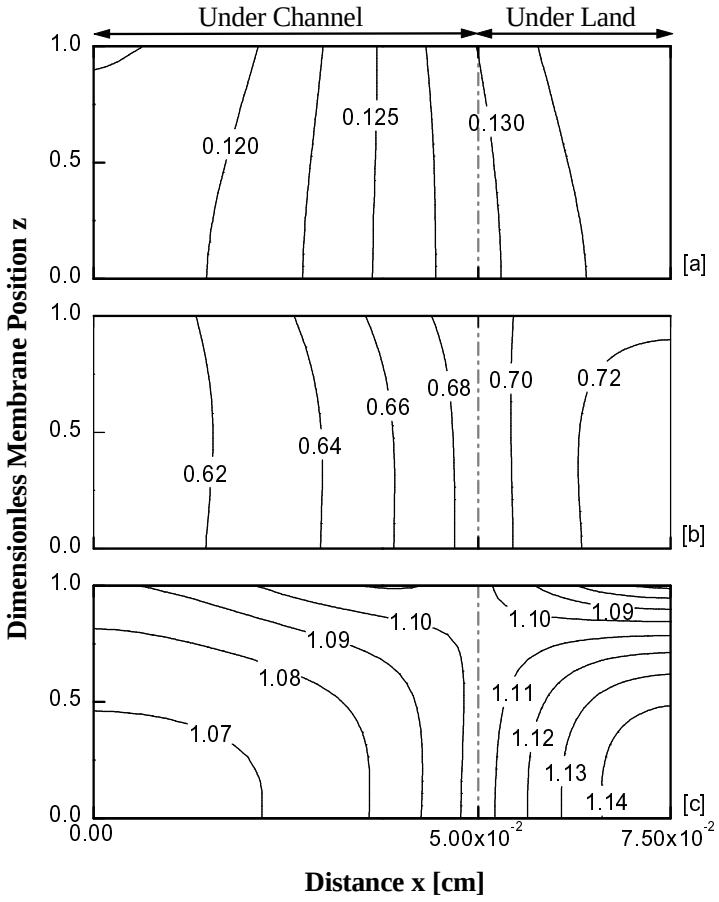

Figure 5.12: Through-plane ionic current density i [A/cm^2] from simulations with 2:1 channel to land aspect ratio at [a] 0.3 V, [b] 0.5 V and [c] 0.7 V of NCOs

Figure 5.13 reveals the results obtained with boundary conditions in simulations with a 4:1 channel to land aspect ratio. Comparing the figure to Figure

5.8, it can be seen that regions of higher conductivity (under the land) showed higher current densities. It is also important to observe that the area of the membrane showing better local conductivities and current densities under the land is smaller than that of the less conductive portions under the channel. This indicates that simulations with increased channel to land ratios with partially humidified boundary conditions may not actually be beneficial to the performance of the membrane.

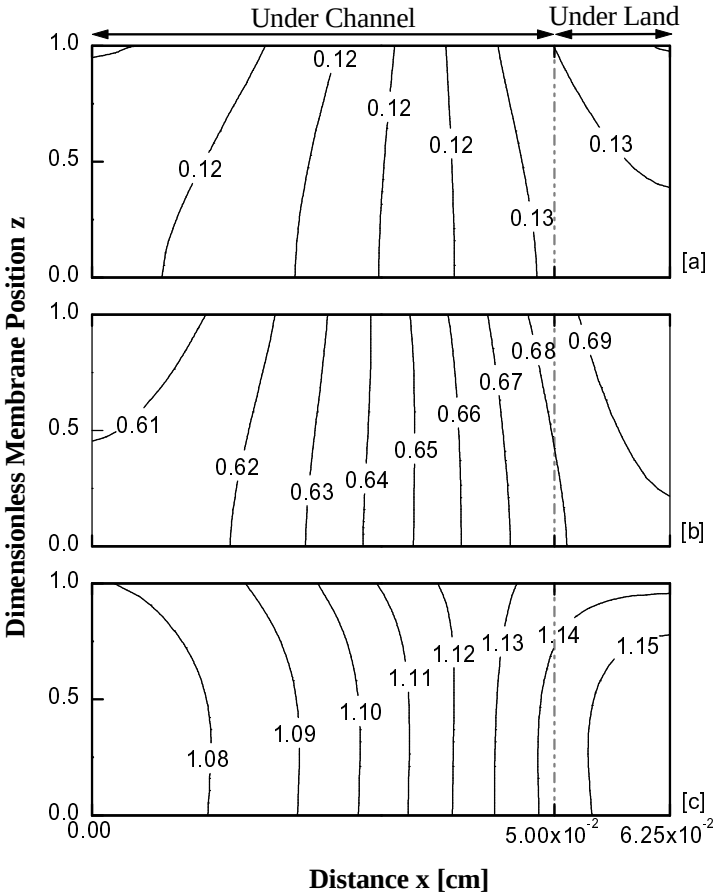

Figure 5.13: Through-plane ionic current density i [A/cm^2] from simulations with 4:1 channel to land aspect ratio at [a] 0.3 V, [b] 0.5 V and [c] 0.7 V of NCOs

Table 5.4 summarises the average membrane conductivity and current density distributions across the two-dimensional membrane domain. It is obvious that

variations in the average membrane conductivity with channel-land ratios directly correspond to the ones observed in the average membrane water content data given in Table 5.3. The PEM phase conductivity increases with the increase in water retention at higher current densities (and thus higher H_2O production). The decrease in conductivity with the increase in channel to land aspect ratio is because of the increase in the water removal from the cathode. It can be observed that at low NCOs, the increase in the aspect ratio has not resulted in a significant decrease in conductivity. At moderate and higher NCOs, a larger channel-land aspect ratio of 2:1 or 4:1 has significantly affected the conductivity. This states that the flow field plate design that is beneficial to catalyst layer (refer to current density column in Table 5.4) may not result in improving the overall conductivity of the membrane.

Table 5.4: Effect of flow field parameters on calculated average membrane conductivity and ionic current density

Channel-land aspect ratio	NCO [V]	Average membrane ionic conductivity $\kappa_{V,avg}$ [S/cm]	Average ionic current density $\mathbf{i}_{avg}$ [A/cm^2]
Base case 1:1	0.3	0.014	0.128
	0.5	0.039	0.647
	0.7	0.070	0.988
2:1	0.3	0.011	0.125
	0.5	0.019	0.664
	0.7	0.032	1.094
4:1	0.3	0.011	0.122
	0.5	0.014	0.646
	0.7	0.023	1.109

$$\kappa_{V,avg} = \frac{1}{V}\sum_{j}^{n_x}\sum_{k}^{n_z}\kappa_V(j,k)dV \;;\; \mathbf{i}_{avg} = \frac{1}{V}\sum_{j}^{n_x}\sum_{k}^{n_z} i(j,k)dV$$

5.3.4 Factors Influencing the Local Ohmic Losses in the Membrane

A factor that influences the local ohmic losses is the hydration state of the membrane. Ohmic resistances towards current flow are inherent in the membrane. Under fully humidified conditions, they are expected to show little variation across membrane. This means that if the membrane is fully hydrated ($\lambda_L = 22$), ohmic losses across the membrane would not vary. In contrary, this might not be true in the case of an unsaturated ($\lambda_V < 11 \text{ at } T = 353\,\text{K}$) vapour equilibrated membrane. It is obvious that this is because the ionic conductivity of the membrane is dependent on the extent of water humidification. Although initial hydration of the membrane is absolutely necessary for attaining the threshold volume fraction of water required for proton conductivity, a further increase (or decrease in membrane resistivity, $r = 1/\kappa$) depends on the amount of water absorbed. It is apparent from earlier discussions that flow field plate design significantly alters the membrane water distribution and local current densities. In order to investigate the impact of this flow field plate design on losses, ohmic loss ($\mathbf{i}r$) plots have been generated.

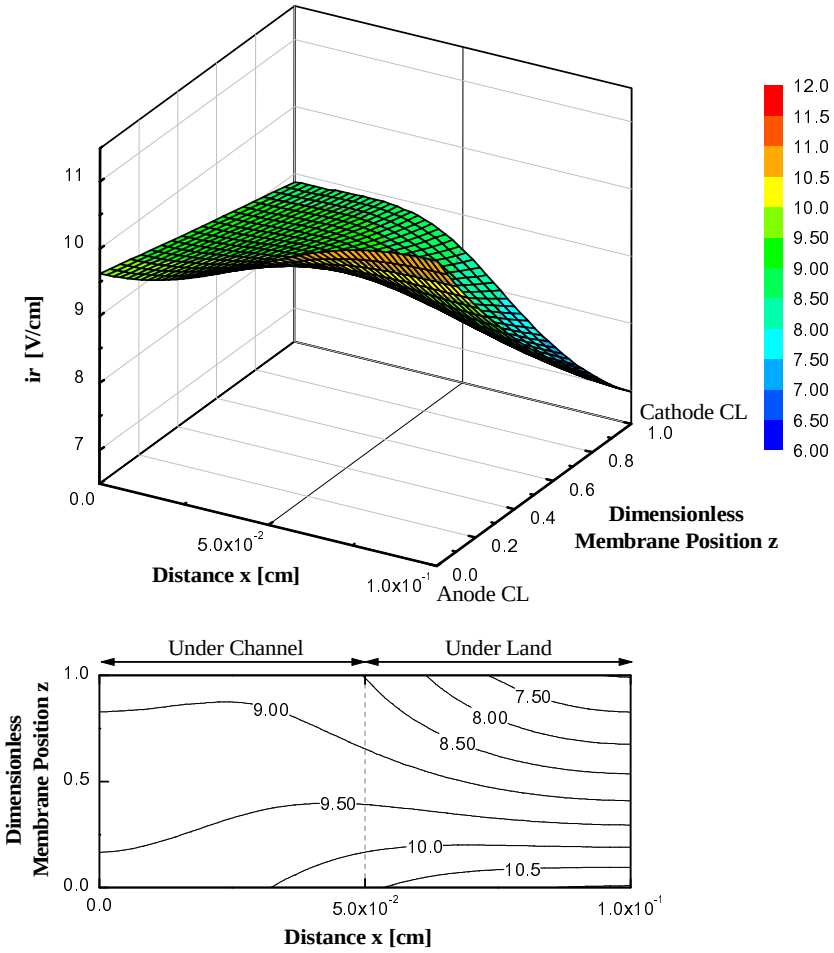

Figure 5.14: Membrane (i*r*) distribution from base case simulation at i_{avg} = 0.128 A/cm^2 (0.3 V NCO).

Figure 5.14 shows the local ohmic distribution from a base case simulation at an average current density of 0.128 A/cm^2. As expected, the *ir* distribution is influenced by the membrane water profile. The minimum local ohmic drop has occurred in the region under the land where the maximum water content was observed (refer to water content profile from the corresponding case in Figure 5.2 [a]). It can also be found from Figure 5.10 [a] and 5.14 that maximum current density along the

in-plane width of membrane-cathode CL occurred in the region of minimum ohmic drop. Thus, at lower current densities and with the base case channel-land configuration, circumstances forcing protonic current through the membrane might not adversely result with the ohmic losses. A better hydration option, improving the membrane water distribution could indeed lessen the anisotropy in the ohmic loss distribution and improve the membrane performance.

It has to be mentioned that the study of PEM phase conductivity related ohmic losses evaluated in this work explains the influence of cathode side mass transport and design aspects but does not predict the relevant effects arising from the conditions at the anode. This is because water (chemical potential) boundary conditions along the anode-membrane interface have been assumed to be uniform. Nevertheless, the emphasis here is laid on showing the impact of the flow field plate design and cathode mass transport factors on the ohmic losses in the membrane.

Figure 5.15 shows the ohmic distribution from a base case simulation with an average current density of 0.647 A/cm^2 (at 0.5 V NCO). It is observed that the portions of the membrane (refer to Figure 5.10 [b]) at the channel/land junction which exhibited higher local current densities had less ohmic losses than the observed area of lower current density under the channel. Although the portions showing higher current densities with low ohmic losses do not hamper the membrane performance, in this case, they represent only a small part of the membrane domain. On the other hand, it is obvious that the overall performance of the membrane will still be influenced by the portions showing greater ohmic losses under the channel.

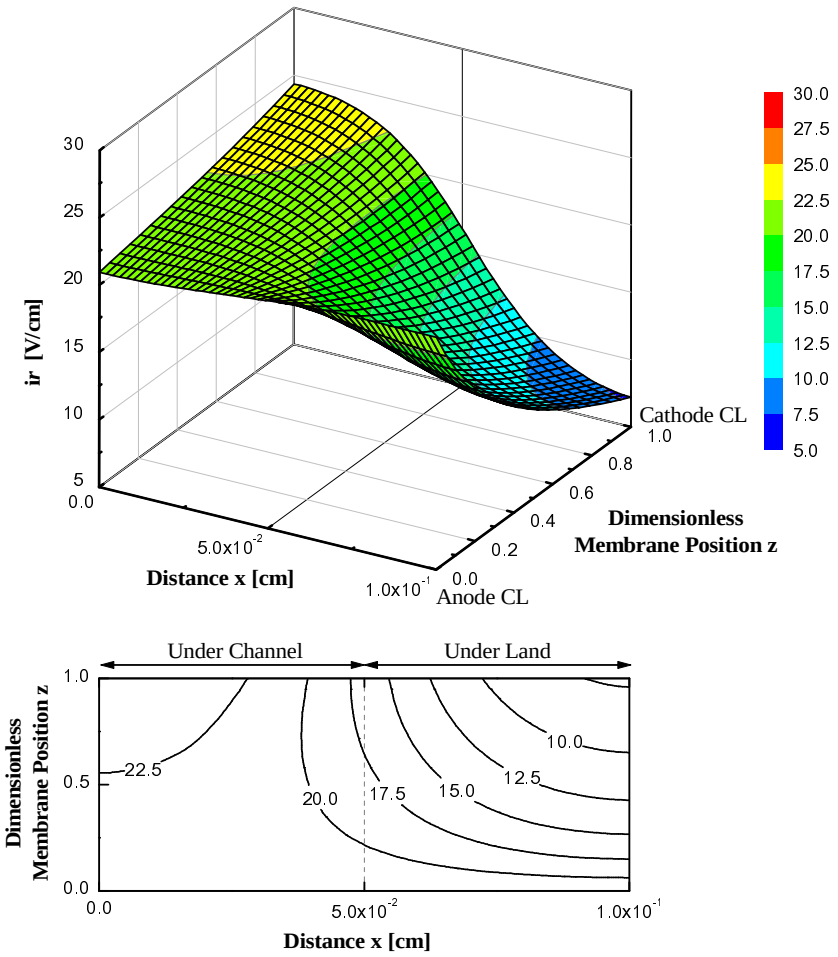

Figure 5.15: Membrane (*ir*) distribution from base case simulation at 0.5 V NCO.

At higher current densities, the local ohmic distribution from the base case simulation, shown in Figure 5.16, reveals that the performance of the membrane in the vapour saturated portion under the land is better than that under the channel. Although it is understood that the local ohmic behaviour of the membrane is based on its hydration state, it has to be observed that maximum current density along the membrane-cathode catalyst layer has not occurred in the region of low ohmic profile. This is because the boundary conditions have forced the membrane to conduct the ionic current through the region under the channel. Hence, the local *ir* losses are more

in these regions where relatively larger local current densities and lesser water content were observed (refer to Figures 5.10 [c] and 5.2[c]).

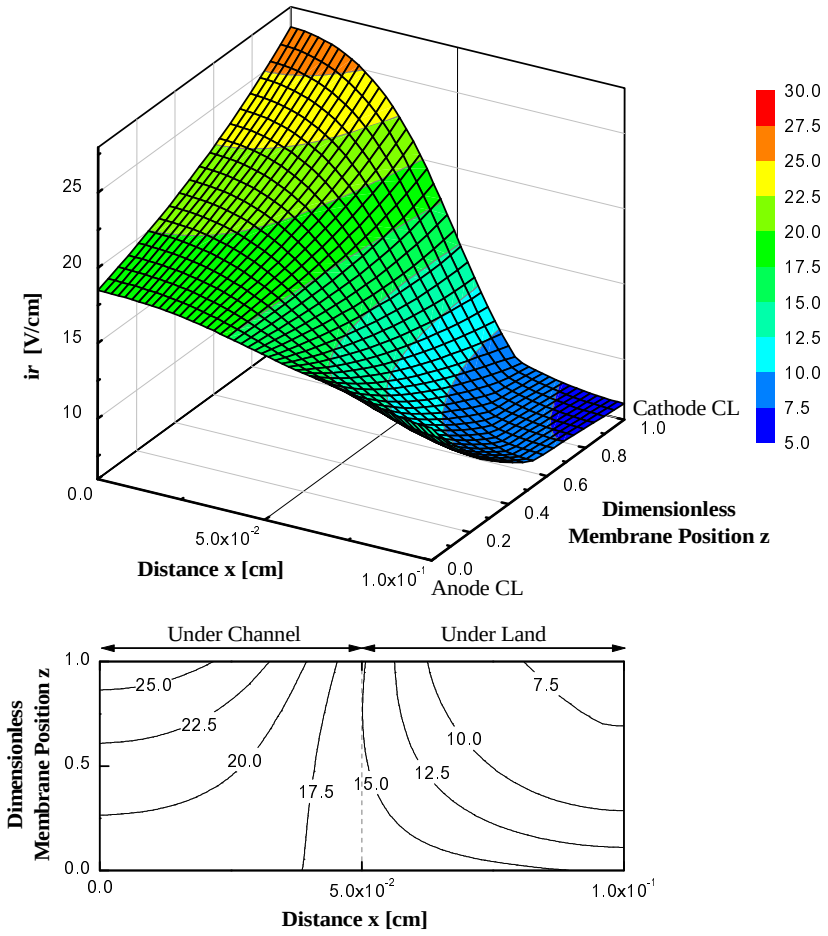

Figure 5.16: Membrane (i*r*) distribution from base case simulation at 0.7 V NCO

Based on the above observations of the base case simulation, it can be inferred that, in an unsaturated membrane operating at higher current densities of $\mathbf{i}_{avg}$ = 0.988 A/cm^2 (at 0.7 V NCO) and with uneven water distribution, the local ohmic losses in the regions showing poorer water retention and greater local current densities are greater and not desirable.

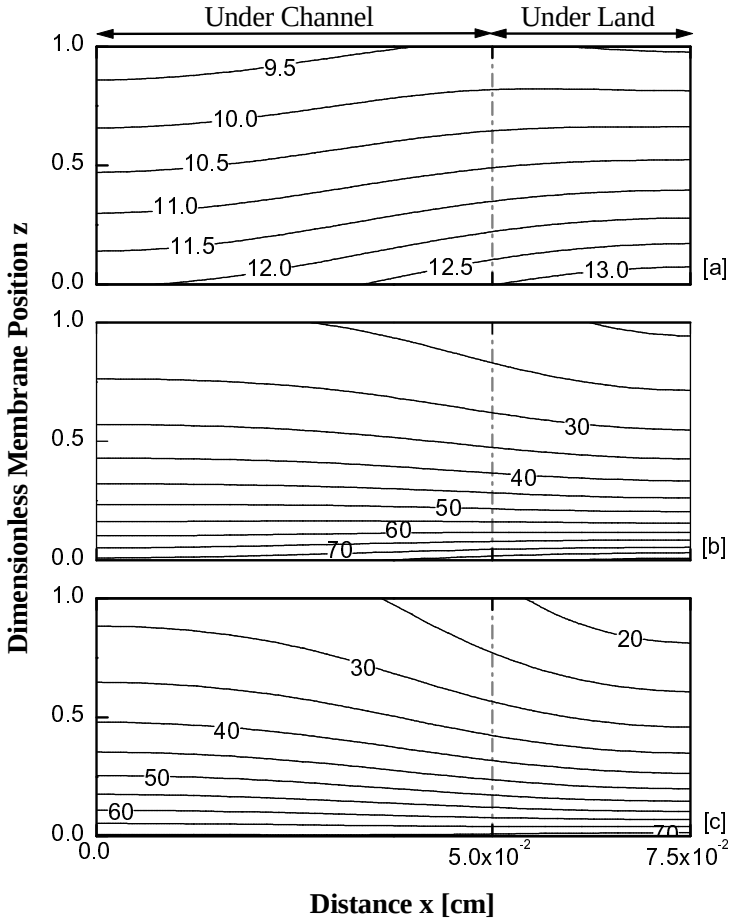

Figure 5.17: Membrane (i_r) distribution [V/cm] from simulations with 2:1 channel to land ratio at 0.3 V, 0.5 V and 0.7 V NCOs

The local ohmic loss profiles from simulations with the boundary conditions influenced by the channel to land aspect ratio of 2:1 are shown in Figure 5.17. It can be observed that contour plots at low, medium and high current densities are less anisotropic than that with base case boundary conditions. This suggests that increasing the channel-land aspect ratio had reduced the anisotropy in ohmic profile. However, due to lower overall water content of the membrane, ohmic drops are comparatively more than that observed in the corresponding cases of the base case simulations.

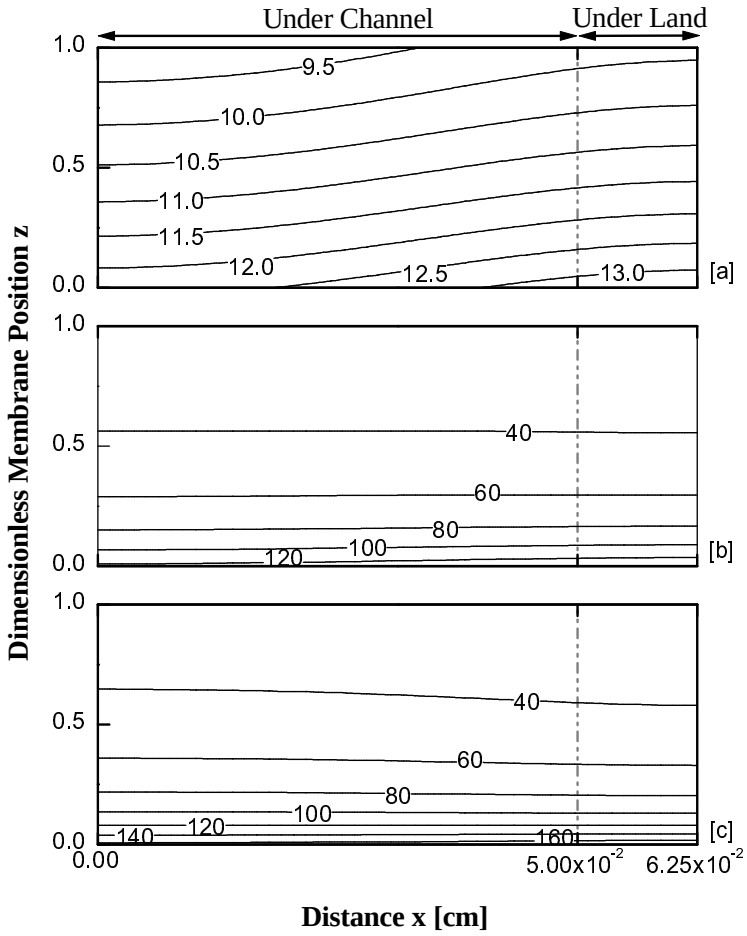

Figure 5.18: Membrane (i_r) distribution [V/cm] from simulations with 4:1 channel to land ratio at 0.3 V, 0.5 V and 0.7 V NCOs

Figure 5.18 shows the local ohmic distribution in the membrane obtained from simulations with a 4:1 channel to land aspect ratio. In all three cases, at low, moderate and high NCOs, it can be observed that overall ohmic losses have increased. This is because of decreased water retention resulting from better water mass transport on the cathode side of the membrane. It has to be mentioned that these circumstances are beneficial in reducing the anisotropy in the PEM phase ohmic loss profile but aggravated ohmic losses are not favourable. In order to gain a clearer understanding of the effects of the flow field plate design on the membrane performance, the details of

the PEM phase losses have been outlined in Table 5.5 presented after the following section on local power consumption.

5.3.5 Factors Influencing Local Power Consumption in the Membrane

In order to illustrate the local power losses across the membrane, local power consumption ($\mathbf{i}^2 r$) plots have been utilised. These plots are expected to throw light on potential areas of local heat evolution inside the membrane domain. As expected, relatively less conductive portions of the membrane have led to more power losses than that observed in more water concentrated portions. It has to be noted that these situations only represent the influence of cathode side physical and mass transport effects but they do not account for the possible repercussions of the hydration state of the anode. As mentioned earlier, this is one of the model's limitations by its nature. Nevertheless, the PEM phase power consumption studies are aimed at understanding the potential causes of geometric and mass transport effects of the cathode on the membrane.

It is quite interesting that power consumption in a base case simulation, with boundary conditions at 0.3 V NCO given in Figure 5.19, is more in the membrane region along the anode/membrane interface under the land. Also, the local power consumption along the membrane/cathode is more at the junction between channel and land. This is because the functional dependence of power loss on the square of local current density ($\mathbf{i}^2$) is more than that on the local resistivity (r).

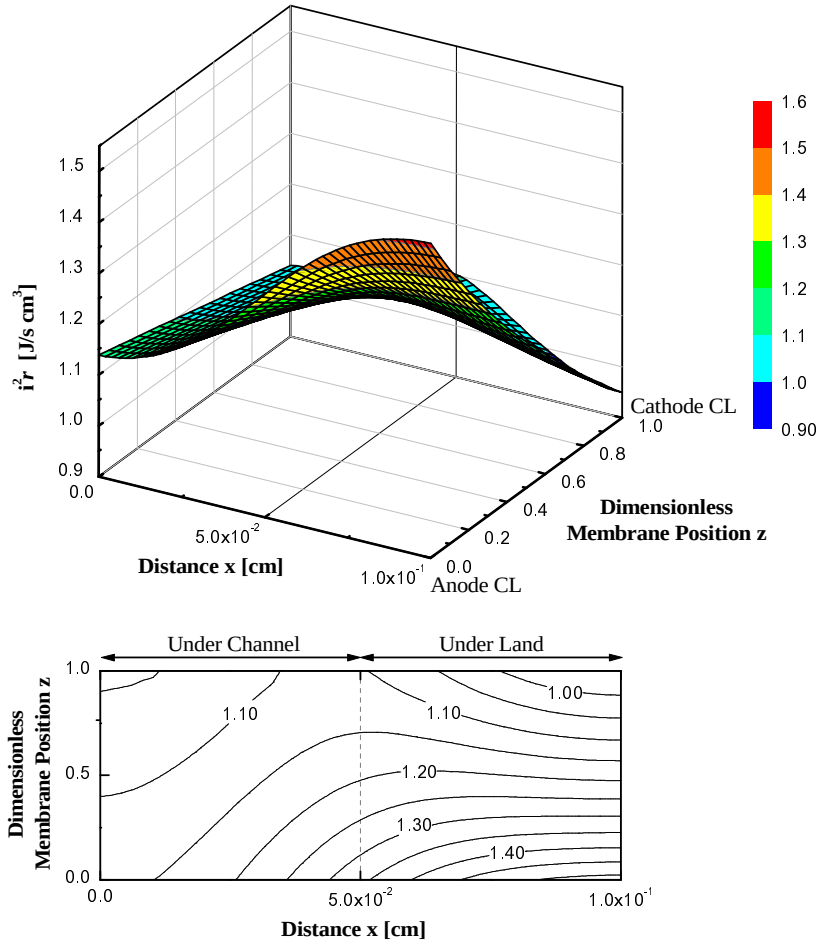

Figure 5.19: Membrane power i^2r [J/s cm^3] drop from simulations with the base case channel to land ratio at 0.3 V NCO.

Figures 5.20 and 5.21 present the local power consumption across the membrane at moderate and high current densities respectively. At moderate NCO of 0.5 V, Figure 5.20 shows that larger power drop inside the membrane has not occurred in the region of greater local current densities (refer to Figure 5.10 [b]) along the cathode catalyst layer/PEM interface at the junction between land and channel. Instead, it can be observed that larger resistive regions of the membrane under the channel have shown a larger power drop.

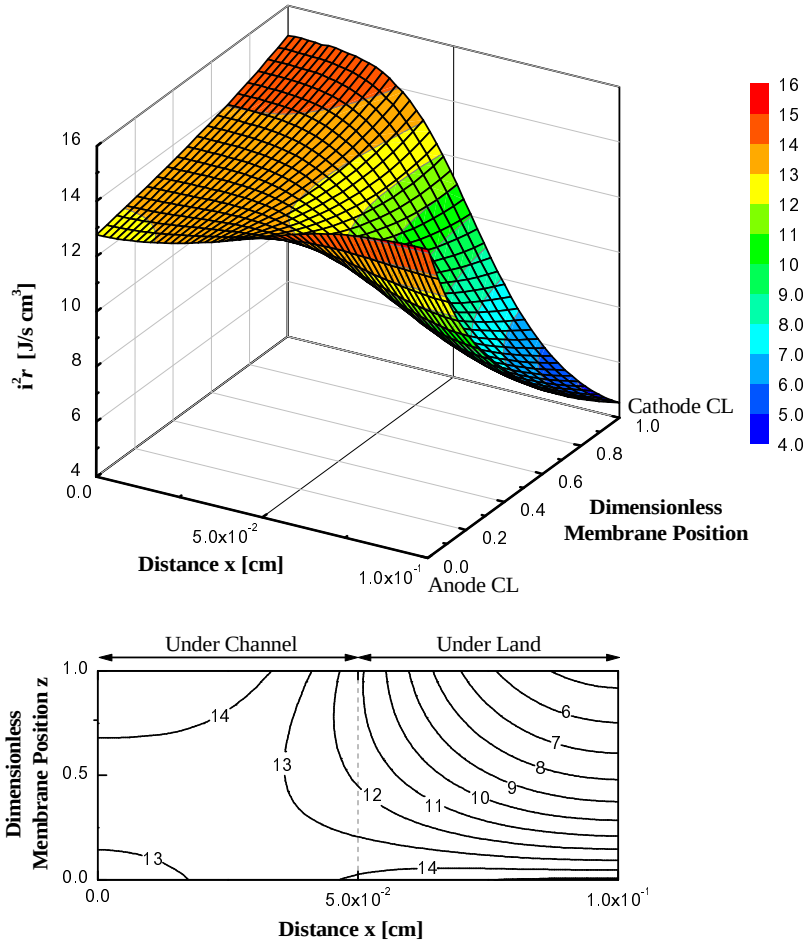

Figure 5.20: Membrane power i^2r [J/s cm^3] drop from simulations with the base case channel to land ratio at 0.5 V NCO

Also from Figure 5.20, it must be obvious that the membrane under the land with less resistive regions have given relatively lower power consumption along the cathode side of the domain. On the other hand, the greater local power losses in the portions along the anode side of the membrane under the land have resulted because of greater local current densities and resistivities.

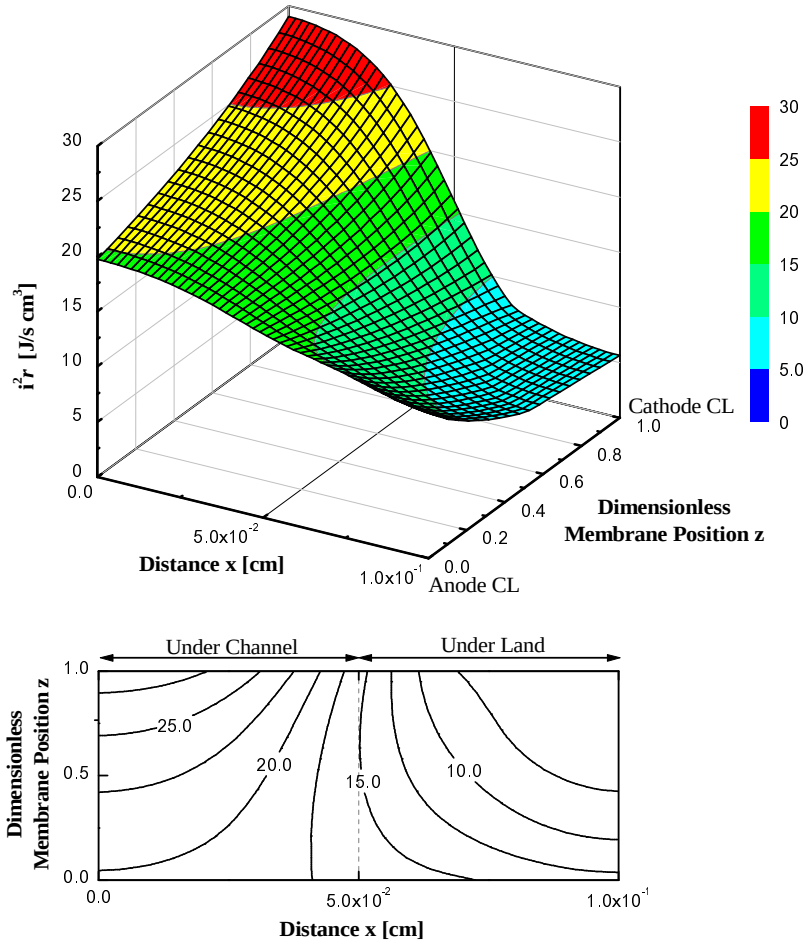

Figure 5.21: Membrane power i^2r [J/s cm^3] drop from simulations with the base case channel to land ratio at 0.7 V NCO

By increasing the current flow by using the high NCO boundary conditions, the membrane power drop profile in Figure 5.21 shows that PEM phase performance was hindered by lack of sufficient water content in the portions under the channel. It can be observed from Figure 5.10 [c] that higher local current densities combined with these more resistive portions under the channel have led to larger power drops. At the same time, the anode side of the membrane under the land showed less power consumption, the reason for which can be lesser local current densities.

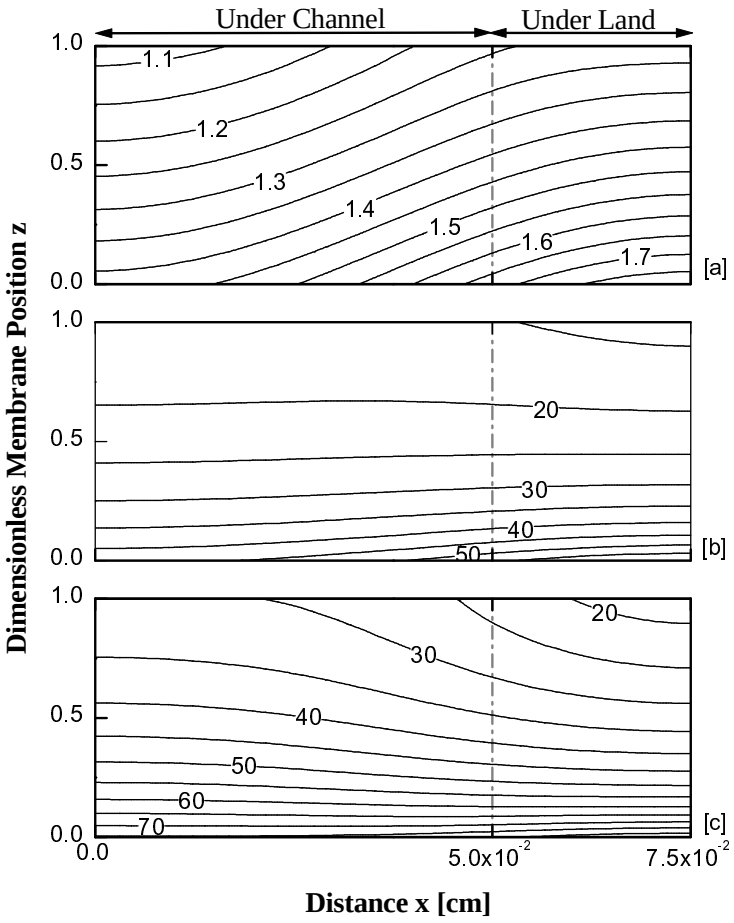

Figure 5.22: Membrane power i^2r [J/s cm^3] drop from simulations with 2:1 channel to land ratio at 0.3 V, 0.5 V and 0.7 V NCOs

Figure 5.22 shows that, with 2:1 channel to land ratio, the overall power drop across the membrane has actually increased compared to that from the corresponding base case simulations. Although power drop at lower current densities in Figure 5.22 [a] has not been significant, at moderate and higher current densities shown in Figures 5.22 [b] and [c], there has been considerable power consumption along the in-plane width near the cathode side of the membrane. The larger power drops along the anode side of the membrane, observed in both Figures 5.22 and 5.23, are caused because of the larger local current densities and ionic resistivities.

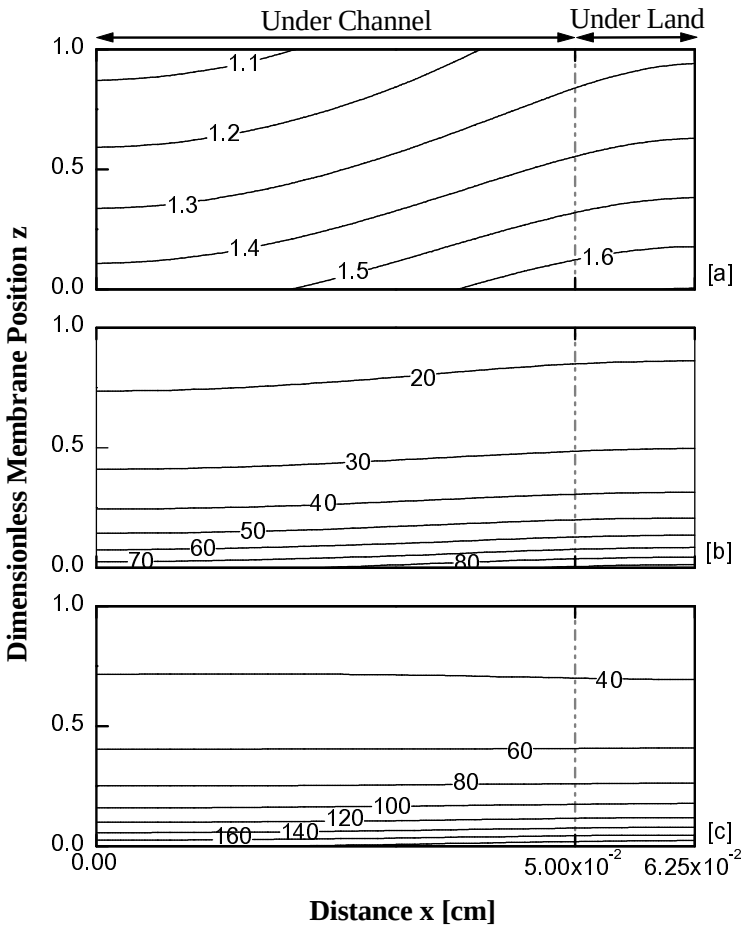

Figure 5.23: Membrane power i^2r [J/s cm^3] drop from simulations with 4:1 channel to land ratio at 0.3 V, 0.5 V and 0.7 V NCOs

Figure 5.23 shows the effect of increasing the channel to land ratio further. This resulted in reducing the anisotropy of the membrane resistivity but has increased the magnitude of local power consumption in all three cases (at low, moderate and high NCOs). This is because a majority of protonic current, in the portions under the land, flows through relatively less humidified membrane portions. A notable influence of increasing the channel to land ratio is that simulations have resulted in less power consumption anisotropy along the in-plane width of the membrane. This could become a positive design aspect if the membrane is fully humidified by water vapour

($\lambda_V = 11$) but in the case of an unsaturated membrane, the observed increase in the power consumption is not desirable.

Table 5.5: Ohmic loss and power consumption across the membrane from simulations with different channel-land configurations

Channel-Land Ratio	NCO [V]	$\mathbf{i}_{avg}$ [A/cm^2]	$(\mathbf{i}r)_{avg}$ [V/cm]	$(\mathbf{i}^2 r)_{avg}$ [J/s cm^3]	R_m [Ω cm^2]
Base case	0.3	0.128	9.169	1.174	1.330
	0.5	0.647	18.034	11.602	0.530
	0.7	0.988	15.576	15.756	0.307
2:1	0.3	0.125	10.866	1.368	1.621
	0.5	0.664	39.792	26.390	1.123
	0.7	1.094	38.703	42.315	0.663
4:1	0.3	0.122	10.990	1.345	1.686
	0.5	0.646	53.729	34.770	1.558
	0.7	1.109	61.209	67.922	1.034

$$(\mathbf{i}r)_{avg} = \frac{1}{V}\sum_{j}^{n_x}\sum_{k}^{n_z}\mathbf{i}r(j,k)dV\ ;\quad (\mathbf{i}^2 r)_{avg} = \frac{1}{V}\sum_{j}^{n_x}\sum_{k}^{n_z}\mathbf{i}^2 r(j,k)dV\ ;\quad R_m = \frac{1}{\mathbf{i}_{avg}A}\sum_{j}^{n_x}\sum_{k}^{n_z}\mathbf{i}r(j,k)dV$$

Table 5.5 summarises the results of conductivity related ohmic losses across the membrane. It can be observed that ohmic losses have increased with the increase in channel to land ratio. This is because of the overall decrease in the membrane water content with the increase in the flow field plate aspect ratio. Fewer ohmic losses have been observed in the base case results because of a better trade-off between water concentrated portions under the land and that under the channel. The increase in power consumption with channel-land aspect ratio is because a larger portion of the membrane has been forced to conduct protonic current through less conductive regions under the channel (refer to plots explained earlier) and that along the anode interface. Finally, it can be observed that the membrane resistance was lower in the base case

simulations than that with increased channel-land ratio. This suggests that with partially humidified vapour equilibrated membranes operating at moderate and high current densities, the flow field design that results in showing improved current densities may not actually be beneficial for the membrane. Also, it should be noted that the manufacturing difficulties involved in designing higher channel to land ratios such as 4:1 (smaller land width) are greater (Scholta *et al.*, 2006).

5.3.6 Effect of Channel-Land Ratio on the Net Water Flux per Proton Flux

A smaller channel to land ratio could promote larger back water diffusion across the membrane from cathode to anode. This is because of the increase in the membrane water content in the portions under the land shown in Figure 5.2 [c]. It can be said that this phenomenon is a consequence of the inefficient water removal from regions under the land of the cathode PTL into the gas channel, which creates a larger chemical potential gradient across the membrane. In contrary, water back diffusion in the membrane portions under the channel might not be on par with that under the land (due to less water concentrated portions under the channel). As a result, one could observe varied water flow patterns inside the membrane. Figure 5.24 presents these effects using results obtained with different channel to land ratios at 0.5 V NCO. Although net water flux varies across the membrane, the net water flux per proton flux (β) has been maintained according to equation 5.3.

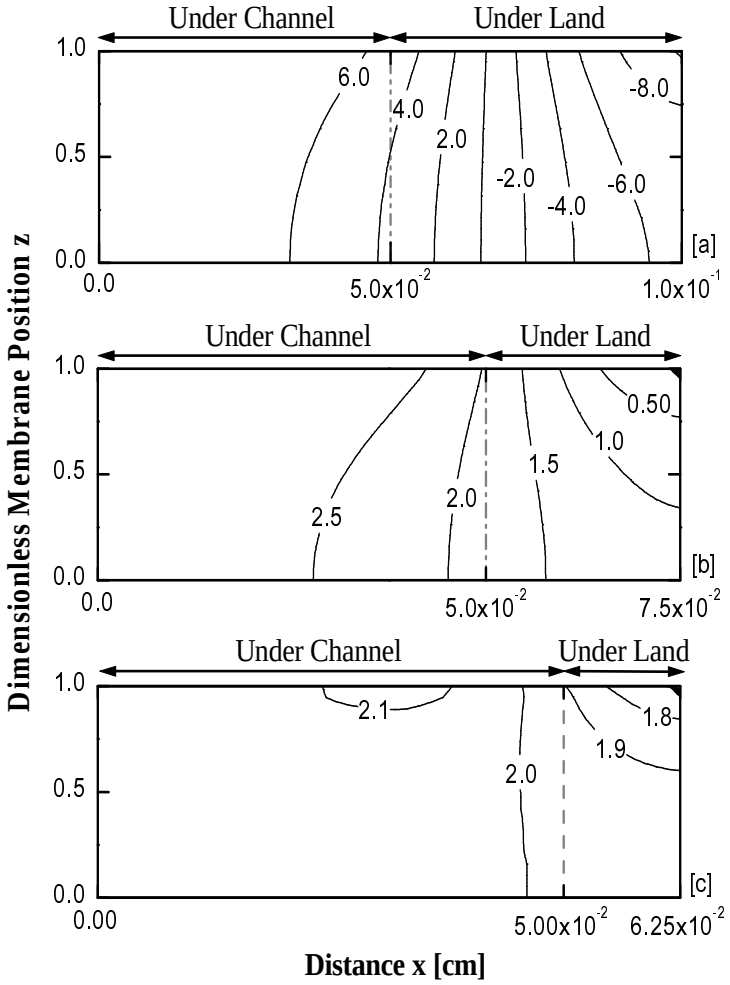

Figure 5.24: Through-plane net water flux [10^6 mol/cm^{2}s] distribution across the membrane from simulations using boundary conditions with 1:1 [a], 2:1 [b] and 4:1 [c] channel to land aspect ratios at 0.5 V NCO

It can be observed from Figure 5.24 [a] that through-plane net water flux across the membrane portions under the land is negative. This indicates that water movement in these portions is from cathode to anode, which predominantly is induced by the increase in water retention in the cathode region under the land. Simultaneously, a positive net water flux across the membrane region under the channel indicates that flow is from anode to cathode. It must be obvious that this has been the situation because of efficient water removal from the cathode PTL under the channel.

Figures 5.24 [b] and [c] reveal that combinations of larger channel to land ratio have resulted in a less anisotropic net water flux distribution, which is positive throughout the membrane indicating water movement from anode to cathode. This observation indicates that water discharge from cathode PTL, in these two cases, has been better than the base case.

5.4 Effect of Membrane Thickness on Water Balance and Ohmic Resistance

Water transport across the membrane also depends on the physical characteristics such as the through-plane membrane thickness. Essentially, the mass transport across a thinner membrane is governed by larger driving force gradients compared to that across a thicker membrane with the same boundary conditions. As a result, it can be anticipated that under the same conditions there would be larger back water diffusion across the thinner membrane. The purpose of this section is to demonstrate these aspects and compare the results obtained from simulations with various Nafion® 1100 *EW* membranes. Table 5.6 shows calculated net water flux per proton flux (β) values from base case simulations with various Nafion® membranes.

The decrease in β with the membrane thickness is evident from Table 5.6. In the case of simulations with N 117, β has been maintained using equation (5.4), and the corresponding values from simulations with Nafion 112 or 115 were computed using the same boundary conditions as that of the simulation with N 117 membrane. As expected, the reason for observed smaller β in thinner membranes (N 115 and N 112) is larger water back diffusion from cathode to anode.

Table 5.6: H_2O/H^+ flux, β, current density, $\mathbf{i}_{avg}$ and membrane resistance, R_m, from base case simulations with Nafion membranes

NCO [V]	Membrane Type†	β	$\mathbf{i}_{avg}$ [A/cm^2]	$\lambda_{V,avg}$	R_m [Ω cm^2]
0.3	N 117	0.385	0.128	3.76	1.330
	N 115	0.139	0.128	3.76	0.950
	N 112	-1.151	0.128	3.76	0.380
0.5	N 117	0.299	0.647	5.81	0.530
	N 115	0.019	0.647	5.81	0.380
	N 112	-1.450	0.647	5.81	0.152
0.7	N 117	0.301	0.988	8.08	0.307
	N 115	0.020	0.988	8.07	0.221
	N 112	-1.450	0.988	8.06	0.089

†: N *xxy* has *xx*00 *EW* and *y* mils thickness ($1\,\text{mil} = 2.54\times10^{-3}$ cm)

It also can be observed from Table 5.6 that a thinner membrane, with the same water content, offers lesser resistance to proton transport than a thicker membrane. This is in accordance with the Ohm's law for electrolytes (Newman *et al.*, 2004), which states that thickness of the ionic conductor affects the potential gradient across the membrane. It is interesting to see that, in all three cases, the membrane resistance has decreased with the increase in current density. The reason for this can be ascribed to the increase in overall membrane water uptake at higher current densities. It should be mentioned that values given in Table 5.6 reflect the influence of cathode side conditions and may not represent that of a complete fuel cell. In a fuel cell operating at with partially humidified inlet gases at higher current densities and thicker membrane (N 117), there may be a possibility that anode side of the membrane may become dehydrated and influence the membrane resistance in a situation when water transport driving forces are not balanced. Thus it is also vital to account these aspects

in the membrane water management of a fuel cell. Also, it has to be mentioned that, when the membrane is fully humidified with liquid water $\lambda_L = 22$, ohmic resistance of the membrane is expected to remain constant.

5.5 Membrane Swelling Constraint Effects

For investigating the effects of constraining the membrane from swelling along its through-plane thickness with membrane water uptake, simulations were performed by considering a range of constraint factors (χ). This is because there is no experimental data available in the literature that shows the magnitude of membrane swelling constraint. Weber *et al.* (2004c) have shown these aspects by modelling the stress balances between the membrane and PTL. They have predicted that a membrane is partially constrained inside the fuel cell and the extent of constraint depends on the hydration state of the membrane and the physico-mechanical properties of the MEA components. Based on Weber's model, it has been assumed that a partially hydrated PEM, considered in this work, is constrained to an extent between 30 to 50 % of that of a free-swelling membrane.

Table 5.7 shows the results obtained from simulations accounting constraint factor on the membrane swelling in through-plane thickness. As mentioned earlier, in all simulations, the membrane has been fully pinched from swelling along its in-plane width. It has to be noted that a constraint factor of $\chi = 0$ means that membrane has been allowed to swell freely in its through-plane thickness. The magnitudes of $\chi > 0$ indicate the extent to which PEM is constrained from swelling along its through-plane thickness. The effect of constraining the membrane is evident from the decrease in the

membrane water uptake with the increase in the magnitude of constraint. Upon constraining, the membrane water uptake decreases when compared to that of a free-swelling membrane. It must be obvious that this occurs as a consequence of the decrease in its overall volume.

Table 5.7: Effect of constraining PEM swelling on water uptake ($\lambda_{V,avg}$), ionic conductivity ($\kappa_{V,avg}$) and H_2O/H^+ flux (β) from base case simulations with Nafion 117 membrane

Current Density $\mathbf{i}_{avg}$ [A/cm^2]	N 117 Constraint Factor χ	$\lambda_{V,avg}$	$\kappa_{V,avg}$ [S/cm]	β
0.128	0	3.76	0.0141	0.385
	0.3	3.71	0.0150	0.356
	0.35	3.70	0.0152	0.351
	0.4	3.69	0.0154	0.346
	0.45	3.68	0.0156	0.341
	0.5	3.67	0.0157	0.336
0.647	0	5.81	0.0393	0.299
	0.3	5.70	0.0426	0.240
	0.35	5.68	0.0432	0.229
	0.4	5.66	0.0438	0.219
	0.45	5.64	0.0444	0.208
	0.5	5.62	0.0450	0.197
0.988	0	8.08	0.0705	0.301
	0.3	7.87	0.0777	0.211
	0.35	7.83	0.0789	0.195
	0.4	7.80	0.0802	0.179
	0.45	7.76	0.0815	0.162
	0.5	7.72	0.0828	0.145

It can also be observed from Table 5.7 that there is a larger decrease in water uptake due to membrane constraints when the unconstrained membrane shows higher water content. This is because the membrane swelling increases with water uptake is

released, and upon constraint, more water than that at low water uptakes. Since all the membrane transport properties are functions of water content directly or indirectly (through water volume fraction), they are also expected to vary with the extent of constraint. It can be seen that the membrane conductivity has actually increased with constraint. This is because the conductivity of the membrane is a strong function of water volume fraction. Although membrane water content has reduced with the constraint, the volume fraction of water has increased because of decreased overall membrane-water volume. Consequently, the conductivity of the membrane has increased when compared to that of a free-swelling membrane.

Constraining the membrane also affects the water balance across the membrane. This is because of the decrease in the membrane thickness with the extent of constraint. It can be understood that this aspect is analogous to what has been observed with the effect of membrane thickness on the net water flux per proton flux β in the preceding section. It can be observed from Table 5.6 that as the constraint factor increases β decreases. This has been the case because of larger water back diffusion from cathode to anode. The reason there was a significant decrease in β at $i = 0.988$ A/cm^2 is that there was a larger chemical potential gradient. It can be found from Figure 5.2 [c] that the portion of membrane along the in-plane width under the land at the cathode/CL interface is saturated, which makes it obvious that there would be a larger chemical potential gradient across the membrane. Hence, upon constraint, the effect of water back diffusion is greater.

5.6 Summary

This chapter presented and discussed the results of the simulations performed with anisotropic boundary conditions on the membrane transport properties, ohmic losses and power consumption under low, medium and high nominal cathode overpotentials. In general, it is apparent that flow field plate design and mass transfer considerations greatly affect the conditions and potential operability of a fuel cell membrane. Performance will not only be dictated by the anisotropy in the PTL and catalyst layer, but the resulting anisotropic conditions in the membrane also need to be considered. The study the effect of physical aspects such as the membrane thickness showed that the ohmic resistance contributed by the membrane reduced with its thickness. The membrane thickness also plays an important role in governing the net water flux across the membrane. The analysis of the membrane swelling constraints revealed that they alter the membrane water retention and transport properties of a free-swelling membrane. Further, a detailed summary of the observed results and conclusions will be presented in the next chapter.

6. CONCLUSIONS AND FUTURE WORK

6.1 Conclusions

The variation in the local performance of the membrane based on its hydration state has been predicted in the current analysis. It has been found that the anisotropy in membrane ionic conductivity, influenced by the cathode side conditions and flow field plate geometry, decreases with the increase in the channel to land aspect ratio. Interestingly, it has been observed that the increase in the channel to land ratio with fixed inlet relative humidities affects the performance of the membrane by lowering its average ionic conductivity. This is because of the decrease in the overall membrane water retention in simulations with boundary conditions influenced by 2:1 or 4:1 channel to land ratios. The membrane-cathode catalyst layer boundary conditions obtained from Sun (2005a-c) suggest that the increase in the channel to land ratio betters the performance of the cathode to a reasonable extent, but the membrane layer simulations performed in this work reveal that ohmic losses across the membrane will be aggravated with the increase in channel-land configurations under low humidified conditions. The results obtained by using a decoupled membrane model in this work neglect the mutual effects of ohmic losses between the membrane and catalyst layers. Hence, the analyses of ohmic distribution and power consumption across the membrane with the computer model may not represent that of a realistic fuel cell membrane but they does show the potential consequences of anisotropic boundary

conditions along membrane-cathode electrode interface on the performance of a fuel cell membrane.

In simulations of base case, membrane water retention in the portions under the land had supplemented the overall conductivity of the membrane. This has not been the case in simulations with increased channel to land ratio, where increased water removal from cathode has had an impact on the cathode side membrane boundary conditions reducing the overall conductivity of the membrane. A smaller channel to land ratio promotes larger back water flux keeping the membrane sufficiently hydrated reducing the conductive losses $(\mathbf{i}r)$. This can be found from the results presented in Table 5.5, where base case $(\mathbf{i}r)_{avg}$ value at 0.7 NCO has been found to be considerably lower than the corresponding values from simulations with 2:1 and 4:1 channel to land ratio influenced boundary conditions. These observations imply that, with partially humidified inlet gases, a smaller channel to land aspect ratio of flow field plate could keep the membrane better humidified than that with a larger configuration. This aspect of design has to be carefully dealt for optimising a flow field plate configuration that is beneficial for the mass transport in both porous transport/catalyst and membrane layers.

The physical parameters of the membrane also play an influential role in governing the performance and water balance across the membrane. It has been found that with the same boundary conditions, N 112 offered lesser resistance (R_m) to protonic current than that by N 117. Also, the net water flux per proton flux has decreased with the membrane thickness. This has been the case because of the larger water back diffusion from cathode to anode, which exceeded the electro-osmotic flux.

The membrane swelling constraint analysis revealed that ionic conductivity improves when the membrane is partially constrained from swelling (< 50 %). Although, water retention inside a partially constrained membrane is lower compared to that of a free-swelling membrane, the conductivity improves because of the increase in the volume fraction of water inside the membrane. So, one can expect the partially constrained membrane exhibit a better performance than an unconstrained membrane. Although, this situation is beneficial from the performance perspective, it may also be possible that expansion-contraction cycles of the membrane could affect its durability. This is because the volume of the membrane varies with its water retention. Nonetheless, analysing the relevant effects is beyond the scope of this thesis.

6.2 Future Work

The computational framework set for solving the membrane layer mass transport model of a PEM fuel cell has to be extended to account for the mass transport equations in both porous transport and agglomerate catalyst layers. The finite volume method should be applied to solve the transport phenomena in all layers of a fuel cell, iteratively. Such a framework is expected to provide a foundation for performing more comprehensive analysis of the MEA water and thermal management aspects between the flow field plates at either electrode of a fuel cell. In general, the following aspects could be included in the future work for improving the applicability of the computer model in a unit cell design:

- Developing a computer model to simulate the two-dimensional, two-phase, mass and heat transport across a fuel cell MEA sandwich and integrate the species fluxes along the length of the channel (pseudo three-dimensional).

- Analysing the influence of mass transport limitations in either electrode of the fuel cell on the performance of the membrane.
- Extending the membrane constraint model to perform the membrane durability/failure analysis with alternate MEA component parameters.

LITERATURE CITED

Berger, Carl, 1968. Handbook of Fuel Cell Technology. *Prentice-Hall, Inc. Englewood Cliffs, N.J.*, First Edition.

Bernardi, D. M. and Verbrugge, M. W., 1991. Mathematical Model of a Gas Diffusion Electrode Bonded to a Polymer Electrolyte. *AIChE Journal*, 37: 1151-1163.

Bernardi, D. M. and Verbrugge, M. W., 1992. A Mathematical Model of the Solid-Polymer-Electrolyte-Fuel Cell. *J. Electrochem. Soc.*, 139: 2477-2490.

Bird, R. B., Stewart, W. E. and Lightfoot, E. N., 2002. Transport Phenomena. *John Wiley & Sons, Inc.*, Second Edition: 538, 582-600.

Bossel, U., 2005. On the Way to a Sustainable Energy Future. *Intelec '05' Berlin*.

Boyle, N. G., McBrierty, V. J. and Eisenberg, A., 1983. NMR Investigation of Molecular Motion in Nafion Membranes. *Macromolecules*, 16: 80-84.

Cappadonia, M., Erning, J. W., Niaki, S. M. S. and Stimming, U., 1995. Conductance of Nafion 117 membranes as a Function of Temperature and Water Content. *Solid State Ionics*, 77: 65-69.

Carrette, L., Friendrich, K. A. and Stimming, U., 2001. Fuel Cells - Fundamentals and Applications. *Fuel Cells*, 1: 5-39.

Choi, K., Peck, D., Kim, C. S., Shin, D. and Lee, T., 2000. Water Transport in Polymer Membranes for PEMFC. *J. Power Sources*, 86: 197-201.

Choi, P. and Datta, R., 2003. Sorption in Proton-Exchange Membranes. *J. Electrochem. Soc.*, 150: E601-E607.

Costamagna, P. and Srinivasan, S., 2001. Quantum jumps in the PEMFC science and technology from the 1960s to the year 2000, Part I. Fundamental scientific aspects. *J. Power Sources*, 102: 242-252.

Chase, M. W., 1986. JANAF Thermochemical Tables, *ACS & AIP, USA.*

Falk, M., 1980. An Infrared Study of Water in Perfluorosulfonate (Nafion) Membranes. *Can. J. Chem.*, 58: 1495-1501.

Fontes, E. and Nilsson, E., 2001. Fuel cells in the Automotive Industry. *Comsol AB.*

Fuller, T. F. and Newman, J., 1993. Water and Thermal Management in Solid-Polymer-Electrolyte Fuel Cells. *J. Electrochem. Soc.*, 140: 1218-1225.

Fuller, T. F., 1992. Solid-Polymer-Electrolyte Fuel Cells. Ph.D. Thesis, University of California-Berkeley. *UMI, MI, USA.*

Futerko, P. and Hsing, I., 1999. Thermodynamics of Water Vapour Uptake in Perfluorosulfonic Acid Membranes. *J. Electrochem. Soc.*, 146: 2049-2053.

Gebel, G., Aldebert, P. and Pineri, M., 1987. Structure and Related Properties of Solution-Cast Perfluoronated Ionomer Films. *Macromolecules*, 20: 1425-1428.

Gebel, G., Aldebert, P. and Pineri, M., 1993. Swelling Study of Perfluorosulphonated Ionomer Membranes. *Polymer*, 34: 333-339.

Gurau, V., Liu, H. and Kakac, S., 1998. Two-Dimensional Model for Proton Exchange Membrane Fuel Cells. *AIChE Journal*, 44: 2410-2422.

Hinatsu, J. T., Mizuhata, M., and Takenaka, H., 1994. Water Uptake of Perfluorosulfonic Acid Membranes from Liquid Water and Water Vapour. *J. Electrochem. Soc.*, 141: 1493-1498.

Hoffman, K. A. and Chiang, S. T., 2000. Computational Fluid Dynamics, Volume II. *Engineering Education System, KS, USA.*

Hoogers, G., 2003. Fuel Cell Technology Handbook. *CRC Press LLC, USA*, First Edition.

Hsu, W. Y., Barkley, J. R. and Meakin, P., 1980. Ion Percolation and Insulator-to-Conductor Transition in Nafion Perfluorosulfonic Acid Membranes. *Macromolecules*, 13: 198-200.

Hsu, W. Y. and Gierke, T. D., 1982. Elastic Theory for Ion Clustering in Perfluorinated Ionomers. *Macromolecules*, 15: 101-105.

Hsu, W. Y. and Gierke, T. D., 1983. Ion Transport and Clustering in Nafion Perfluorinated Membranes. *J. Membrane. Sci.*, 13: 307-326.

Hsu, C. H. and Wan, C. C., 2003. An Innovative Process for PEMFC Electrodes Using the Expansion of Nafion Film. *J. Power Sources*, 115: 268-273.

Incropera, F. P. and DeWitt, D. P., 2002. Fundamentals of Heat and Mass Transfer. *John Wiley, NY, USA*, Fourth Edition.

Iwamoto, R., Oguro, K., Sato, M. and Iseki, Y., 2002. Water in Perfluorinated Sulfonic Acid Nafion Membranes. 106: 6973-6979.

Janssen, G. J. M. and Overvelde, M. L. D., 2001. Water Transport in Proton-Exchange Membrane fuel cell: measurements of the effective drag coefficient. *J. Power Sources*, 101: 117-125.

Kumar, A. and Reddy, R., 2003. Effect of Channel Dimensions and Shape in Flow-Field Distributor on the Performance of the Polymer Electrolyte Membrane Fuel Cells. *J. Power. Sources*, 113: 11-18.

Larminie, J. and Dicks, A., 2000. Fuel Cell Systems Explained. *John Wiley & Sons, Ltd., England*, First Edition.

Laughton, M. A., 2002. Fuel cells. *Power Eng J*., 16: 37-47.

Lehtinen, T., Sundholm, G., Holmberg, S., Bjornbom, P. and Bursell, M., 1998. Electrochemical Characterization of PVDF-based Proton Conducting Membranes for Fuel Cells. *Electrochim. Acta*, 43-1881-1890.

Mathias, M. F., Makharia, R., Gasteiger, H. A., Conley, J. J., Fuller, T. J., Gittleman, C. J., Kocha, S. S., Miller, D. P., Mittelsteadt, C. K., Xie, T., Yan, S. G. and Yu, P. T., 2005. Two Fuel Cell Cars in Every Garage?. *The Electrochem. Soc. Interface, Fall 2005*: 24-35.

Meyers, J. P., 1998. Simulation and Analysis of the Direct Methanol Fuel Cell, Ph.D. Thesis, University of California-Berkeley, *UMI, MI, USA.*

Meyers, J. P. and Newman, J., 2002. Simulation of the Direct Methanol Fuel Cell, I. Thermodynamic Framework for a Multicomponent Membrane. *J. Electrochem. Soc.*, 149: A710-A717.

Natarajan, D. and Nguyen, T. V., 2001. A Two-Dimensional, Two-Phase, Multicomponent, Transient Model for the Cathode of a Proton Exchange Membrane Fuel Cell Using Conventional Gas Distributors. *J. Electrochem. Soc.*, 148: A1324-A1335.

Newman, J. and Thomas-Alyea, K. E., 2004. Electrochemical Systems. *John Wiley & Sons, Inc.*, Third Edition.

Nguyen, T. V. and White, R. E., 1993. A Water and Heat Management Model for Proton Exchange Membrane Fuel Cells. *J. Electrochem. Soc.*, 140: 2178-2186.

Okada, T., Xie, G. and Meeg, M., 1998. Simulation for Water Management in Membranes for Polymer Electrolyte Fuel Cells. *Electrochimica Acta*, 43: 2141-2155.

Onsager, L., 1931. Reciprocal Relations in Irreversible Processes. II. *Phys. Rev.*, 37: 2265-2279.

Patankar, S. V., 1980. Numerical Heat Transfer and Fluid Flow. *Hemisphere Publishing Corp., USA*, First Edition.

Perry, M. L. and Fuller, T. F., 2002. A Historic Perspective of Fuel Cell Technology in 20th Century. *J. Electrochem. Soc.*, 149: S59-S67.

Pintauro, P. N. and Bennion, D. N., 1984. Mass Transport of Electrolytes in Membranes. 1. Development of Mathematical Transport Model. *Ind. Eng. Chem. Fundam.*, 23: 230-234.

Ren, X. and Gottesfeld, S., 2001. Electro-osmotic Drag of Water in Poly (perfluorosulfonic acid) Membranes. *J. Electrochem. Soc.*, 148: A87-A93.

Schroeder, P. V., 1903. Über Erstarrungs- und Quellungserscheinungen von Gelatine. *Z. Phys. Chem.*, 45: 75-128.

Scholta, J., Escher, G., Zhang, W., Küppers, L., Jörissen, L. and Lehnert, W., 2006. Investigation of the Influence of Channel Geometries on PEMFC Performance. *J. Power Sources*, 155: 66-71.

Slade, S., Campbell, S. A., Ralph, T. R., Walsh, F. C., 2002. Ionic Conductivity of an Extruded Nafion 1100 EW Series of Membranes. *J. Electrochem. Soc.*, 149: A1556-A1564.

Smitha, B., Sridhar, S. and Khan, A. A., 2005. Solid Polymer Electrolyte Membranes for Fuel Cell Applications - a review. *J. Membr. Sci.*, 259: 10-26.

Sone, Y., Ekdunge, P. and Simonsson, D., 1996. Proton Conductivity of Nafion 117 as Measured by a Four-Electrode AC Impedance Method. *J. Electrochem. Soc.*, 143: 1254-1259.

Spakovsky, M. R. V. and Olsommer, B., 2002. Fuel cell systems and system modeling and analysis perspectives for fuel cell development. *Energy Convers. Manage.*, 43: 1249-1257.

Springer, T. E., Zawodzinski, T. A. and Gottesfeld, S., 1991. Polymer Electrolyte Fuel Cell Model. *J. Electrochem. Soc.*, 138: 2334-2341.

Sun, W., Peppley, B.A.P. and Karan, K., 2005a. An Improved Two-Dimensional Agglomerate Cathode Model to Study the Influence of Catalyst Layer Structural Parameters. *Electrochim. Acta*, 50: 3359-3374.

Sun, W., Peppley, B.A.P. and Karan, K., 2005b. Influence of Gas Diffusion Layer and Channel Geometry Parameters on Catalyst Performance: Investigation using a 2-D Model. *J. Power Sources*, 144: 42-53.

Sun, W., 2005. Two-Dimensional Agglomerate Model for the Cathode of a PEM Fuel Cell, M.Sc. Thesis. *Wei Sun, Queen's University, Kingston, Canada*.

Thampan, T., Malhotra, S., Tang, H., and Datta, R., 2000. Modeling of Conductive Transport in Proton-Exchange Membranes for Fuel Cells. *J. Electrochem. Soc.*, 147: 3242-3250.

Thirumalai, D. and White, R. E., 1997. Mathematical Modeling of Proton Exchange Membrane Fuel Cell Stacks. *J. Electrochem. Soc.*, 144: 1717-1723.

Thomas, S, and Zalbowitz, M, 1999. Fuel cells - Green power, *Los Alamos National Laboratory (LANL), NM, USA.*

Verbrugge M.W. and Hill, R.F., 1990. Ion and Solvent Transport in Ion-Exchange Membranes. *J. Electrochem. Soc.*, 137: 886-893.

Versteeg, H. K. and Malalasekera, W., 1995. An Introduction to Computational Fluid Dynamics - The Finite Volume Method. *Longman Scientific and Technical, England.*

Weber, A. Z. and Newman, J., 2003. Transport in Polymer-Electrolyte Membranes, I. Physical Model. *J. Electrochem. Soc.*, 150: A1008-A1015.

Weber, A. Z. and Newman, J., 2004a. Transport in Polymer-Electrolyte Membranes, II. Mathematical Model. *J. Electrochem. Soc.*, 151: A311-A325.

Weber, A. Z. and Newman, J., 2004b. Transport in Polymer-Electrolyte Membranes, III. Model Validation in a Simple Fuel-Cell Model. *J. Electrochem. Soc.*, 151: A326-A339.

Weber, A. Z. and Newman, J., 2004c. A Theoretical Study of Membrane Constraint in Polymer Electrolyte Fuel Cells. *AIChE Journal*, 50: 3215-3226.

Wendt, H. and Kreysa, G., 1999. Electrochemical Engineering, Science and Technology in Chemical and other Industries. *Springer-Verlag Berlin Heidelberg*, First Edition.

West, A. C. and Fuller, T. F., 1996. Influence of Rib Spacing in Proton-Exchange Membrane Electrode Assemblies. *J. App. Electrochem.*, 26: 557-565.

Yeager, H. L. and Steck, A., 1981. Cation and Water Diffusion in Nafion Ion Exchange Membranes: Influence of Polymer Structure. *J. Electrochem. Soc.*, 128: 1880-1884.

Yeo, S. C. and Eisenberg, A., 1977. Physical Properties and Supermolecular Structure of Perfluorinated Ion-Containing (Nafion) Polymers. *J. Appl. Polym. Sci.*, 21: 875-898.

Yeo, R. S., Ion Clustering and Proton Transport in Nafion Membranes and Its Applications as Solid Polymer Electrolyte. *J. Electrochem. Soc.*, 130: 533-538.

Yi, J. S. and Nguyen, T. V., 1998. An Along the Channel Model for Proton Exchange Membrane Fuel Cells. *J. Electrochem. Soc.*, 145: 1149-1159.

Yi, J. S. and Nguyen, T. V., 1999. Multicomponent Transport in Porous Electrodes of Proton Exchange Membrane Fuel Cells Using the Interdigitated Gas Distributors. *J. Electrochem. Soc.*, 146: 34-45.

Zawodzinski, T. A., Neeman, M., Sillerud, L. O. and Gottesfeld, S., 1991. Determination of Water Diffusion Coefficients in Perfluorosulfonate Ionomeric Membranes. *J. Phys. Chem.*, 95: 6040-6044.

Zawodzinski, T. A., Jr, Derouin, C., Radzinski, S., Sherman, R. J, Smith, V. T., Springer, T. E, and Gottesfeld, S, 1993a. Water Uptake by and Transport Through Nafion® 117 Membranes. *J. Electrochem. Soc.*, 140: 1041-1047.

Zawodzinski, T. A., Springer, T. E., Davey, J., Jestel, R., Lopez, C., Valerio, J. and Gottesfeld, S., 1993b. A Comparative Study of Water Uptake by and Transport through Ionomeric Fuel Cell Membranes. *J. Electrochem. Soc.*, 140: 1981-1985.

Zawodzinski, T. A., Davey, J., Valerio, J. and Gottesfeld, S., 1995. The Water Content Dependence of Electro-Osmotic Drag in Proton-Conducting Polymer Electrolytes. *Electrochim*. *Acta.*, 40: 297-302.

APPENDIX A – PARAMETERS AND ADDITIONAL FIGURES

A.1 Physico-Chemical Parameters used in the Membrane Model

Parameter	Value	Reference
Density of water, ρ_0	$1.1603 - 0.0005371 \cdot T$ [g/cm^3]	Weber *et al.*, (2004b)
Density of the dry membrane, $\rho_{m,o}$	2.0 [g/cm^3]	Weber *et al.*, (2004a)
Surface Tension, γ	$(1.1603 - 0.0005371 \cdot T) \times 10^{-2}$ [N/cm]	Weber *et al.*, (2004b), Incropera *et al.*, (2002)
Absolute membrane permeability, k_{sat}	1.8×10^{-14} [cm^2]	Bernardi *et al.*, (1992)
Water vapour pressure, p_0^{vap}	$\exp\left(11.6832 - \frac{3816.44}{T - 46.13}\right)$ [bar]	Weber *et al.*, (2004b)
Channel contact angle, θ	90.02°	Weber *et al.*, (2004a)
Viscosity of water, μ	$(2695.3 - 6.6 \cdot T) \cdot 1 \times 10^{-11}$ [bar s]	Weber *et al.*, (2004b)

A.2 Plots of the Vapour Phase Transport Coefficient

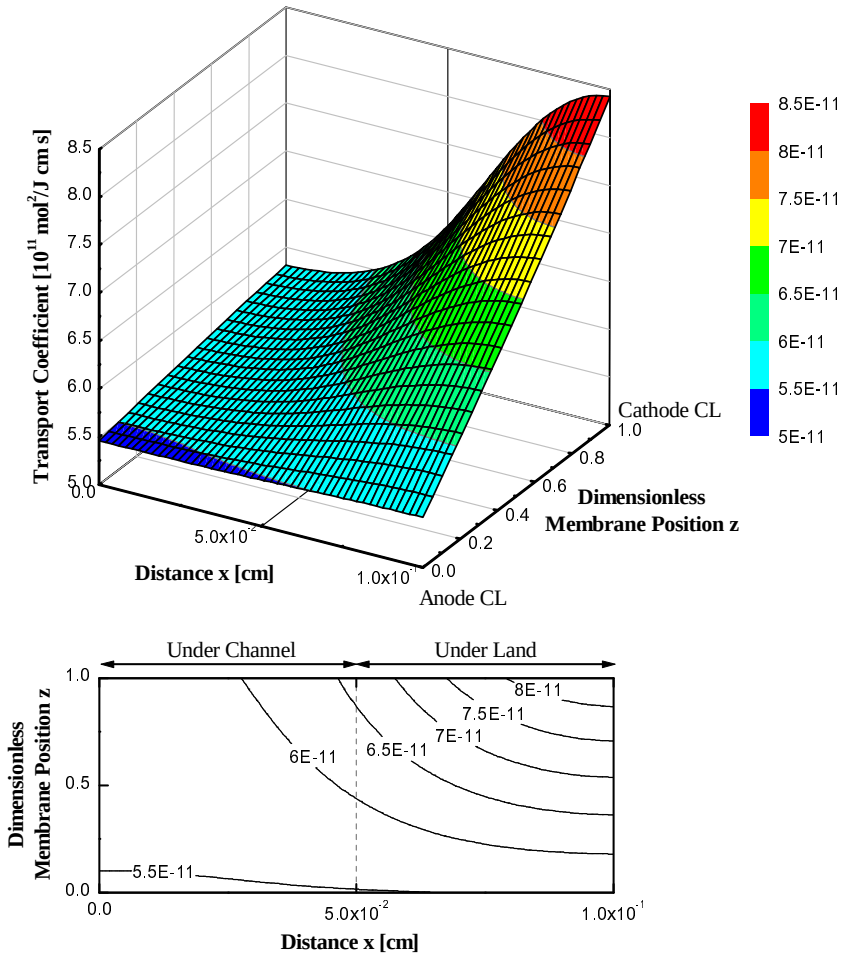

Figure A.1: The vapour phase transport coefficient α_V in a simulation with base case conditions and parameters at 0.3 V NCO.

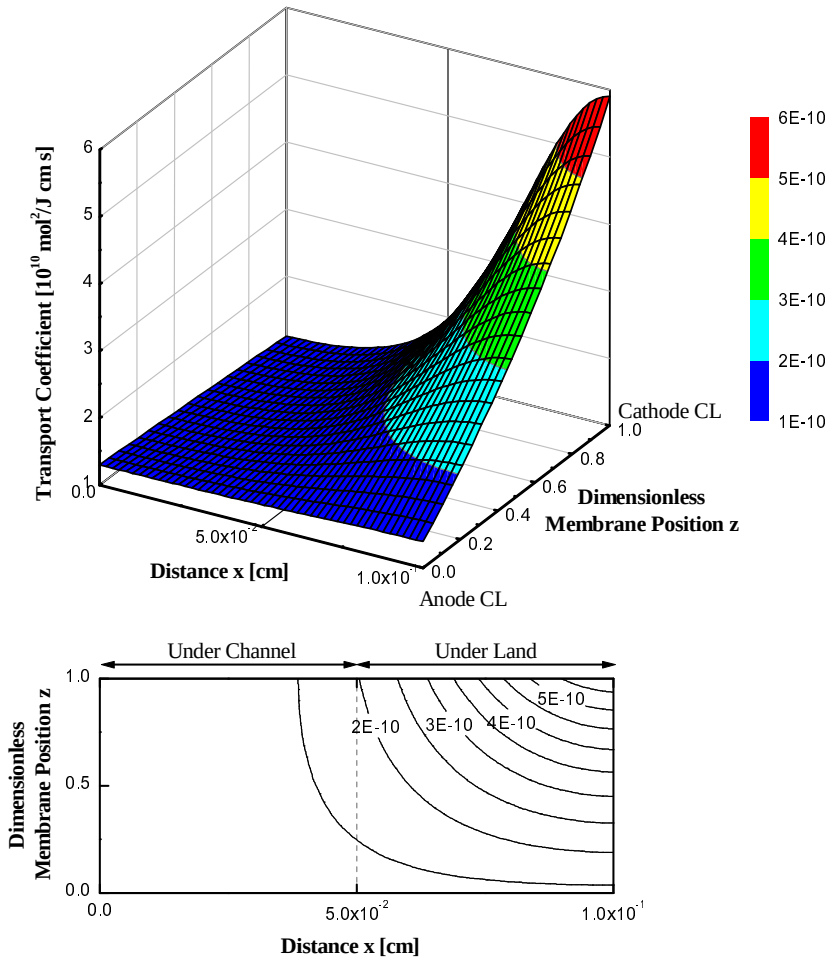

Figure A.2: The vapour phase transport coefficient α_V in a simulation with base case conditions and parameters at 0.5 V NCO.

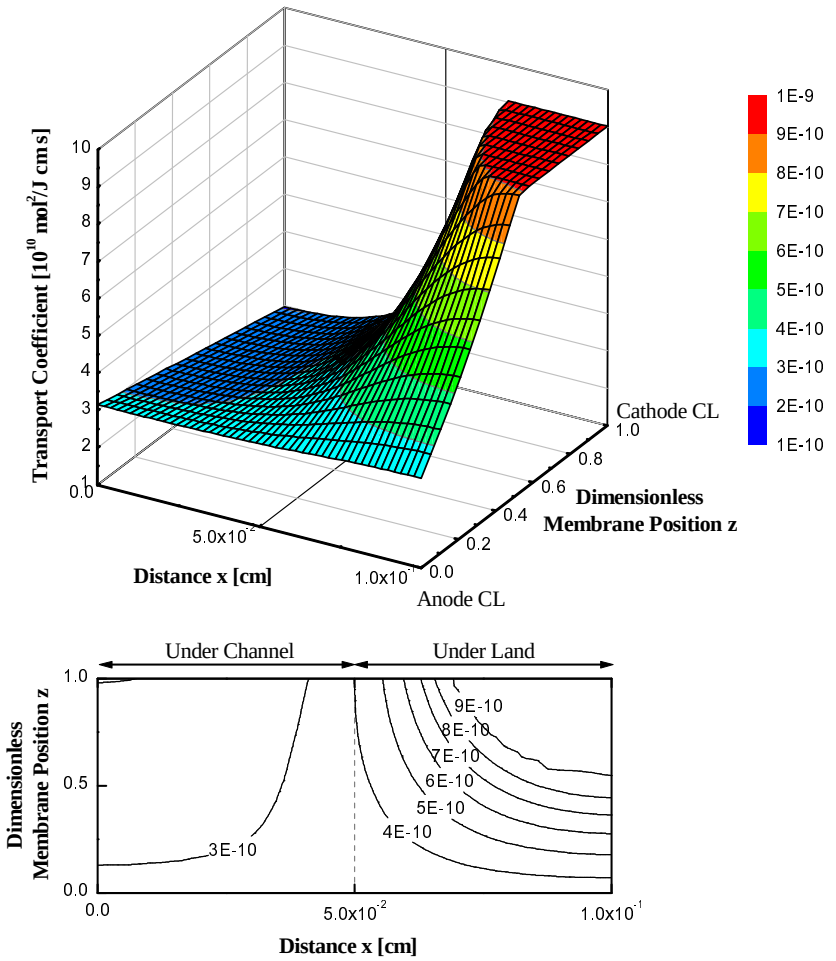

Figure A.3: The vapour phase transport coefficient α_V in a simulation with base case conditions and parameters at 0.7 V NCO.

APPENDIX B – MODELLING MASS TRANSPORT IN THE CATHODE

B.1 Modelling Mass Transport in Porous Transport and Catalyst Active Layers

The equations relevant to the mass transport inside the porous transport and cathode catalyst active layers will be presented in this portion of the appendix. As mentioned earlier, the boundary conditions used in the current work for analysing the anisotropic mass transport issues inside the membrane layer of a fuel cell have been obtained from the agglomerate model by Sun *et al.*, (2005a-b). The equations given in this appendix represent that of an agglomerate cathode half-cell model developed by Sun *et al.* (2005a-b).

In general, the phenomena that occur in the cathode half-cell can be described as follows:

1. Gas diffusion in the porous transport layers towards the catalyst layer.
2. Diffusion of oxygen reduction reaction participating species from high concentrated portions of PTL (O_2) towards the active surface of the agglomerate catalyst structure.
3. Electron conduction through the PTL and catalyst layer towards the reactive surface of the agglomerate structure.
4. Proton migration on the Nafion film surrounding the agglomerate structure.
5. Oxygen reduction on the active surface of the agglomerate catalyst structure.
6. Water production from oxygen reduction reaction.

B.1.1 Reactant Transport

The Stefan-Maxwell equation (Bird *et al.*, 2002) expresses the multicomponent gas diffusion inside the porous transport layer. The modified form the equation accounting the effective diffusivities (Bernardi *et al.*, 1991) in the PTL and catalyst layer, given by Sun *et al.*, (2005b), is as follows:

$$\nabla n_i = \nabla\left[-\rho w_i \sum_j D_{ij}^{eff} \frac{M}{M_j}\left(\nabla w_j + w_j \frac{\nabla M}{M}\right)\right] \tag{B.1}$$

$$D_{ij}^{\text{eff}} = D_{ij}\varepsilon_{PTL}^{1.5} \tag{B.2}$$

$$D_{ij,C}^{\text{eff}} = D_{ij}\varepsilon_{CAT}^{1.5} \tag{B.3}$$

where

n_i = Species mass flux vector,

w_i = Mass fraction for component *i*,

ρ = Density of gas mixture,

M = Molecular weight of the gas mixture,

D_{ij} = Binary diffusivities of species *i* and *j*, and

ε = Porosity.

B.1.2 Electrode Kinetics

The overall oxygen reduction reaction for a four electron transfer reaction on the catalyst active layer can be written as,

$$4H^+ + O_2 + 4e^- \rightleftharpoons 2H_2O$$

A material balance of oxygen over a control volume in the agglomerate catalyst active layer relates gives,

$$\nabla \cdot \mathbf{N}_{o_2} + R_{o_2} = 0 \qquad \text{(B.4)}$$

Expressing the oxygen flux term in equation (A.4) in terms local current density and the oxygen consumption in terms of the reaction rate on the surface of the agglomerate in the cathode catalyst layer, the following equation can be obtained,

$$\nabla \cdot \mathbf{i}_{\text{cl}} = 4F \frac{P_{o_2}}{H} \left(\frac{1}{E_r k_c (1-\varepsilon_{\text{CAT}})} + \frac{(r_{agg}+\delta)\delta}{a_{agg} r_{agg} D} \right)^{-1} \qquad \text{(B.5)}$$

where

a_{agg} = Effective specific surface area of agglomerate,

D = Dissolved oxygen diffusivity in Nafion coating,

E_r = The catalyst effectiveness factor,

H = Henry's law constant,

k_c = Electrochemical reaction rate constant for oxygen reduction reaction,

δ = The thickness of electrolyte coating on the agglomerate,

r_{agg} = Agglomerate radius, and

R_{o_2} = Oxygen consumption in oxygen reduction reaction,

and where

$$\nabla \cdot \mathbf{N}_{o_2} = -\frac{1}{4F} \nabla \cdot \mathbf{i}_{\text{cl}}, \qquad \text{(Note: In the cathode CL, } \nabla \cdot \mathbf{i}_{\text{p}} = \text{-} \nabla \cdot \mathbf{i}_{\text{cl}} \text{)}$$

$$R_{o_2} = \frac{P_{o_2}}{H} \left(\frac{1}{E_r k_c (1-\varepsilon_{\text{CAT}})} + \frac{(r_{agg}+\delta)\delta}{a_{agg} r_{agg} D} \right)^{-1}$$

$$k_c = \left(\frac{\varepsilon_l m_{\mathrm{Pt}} S_{ac}}{4Ft_{cl}(1-\varepsilon_{\mathrm{CAT}})} \right) \cdot \left[\frac{i_0^{ref}}{C_{\mathrm{O}_2}^{ref}} \right] \cdot \left[\exp\left(\frac{-\alpha_c F}{RT} \eta \right) - \exp\left(\frac{(1-\alpha_c)F}{RT} \eta \right) \right]$$

$$E_r = \frac{1}{\phi_L} \left(\frac{1}{\tanh(3\phi_L)} - \frac{1}{3\phi_L} \right)$$

and ϕ_L = Thiele's modulus, $\phi_L = \frac{r_{agg}}{3} \sqrt{\frac{k_c}{D_{\mathrm{eff}}}}$.

B.1.3 Charge Transport and Conservation

Electrolyte phase proton migration and solid phase electron transport in the cathode, given by a simple Ohm's law, are as follows:

$$\mathbf{i}_{\mathrm{p}} = -\kappa_l^{\mathrm{eff}} \nabla \Phi_l \qquad \text{(B.6)}$$

$$\mathbf{i}_{\mathrm{e,C}} = -\kappa_s^{\mathrm{eff}} \nabla \Phi_s \qquad \text{(B.7)}$$

Conservation of charge in the catalyst layer based on the assumption of electroneutrality can be expressed as follows:

$$\nabla \cdot \mathbf{i}_{\mathrm{p}} + \nabla \cdot \mathbf{i}_{\mathrm{cl}} = 0 . \qquad \text{(B.8)}$$

In the gas diffusion layer, the charge transport is conserved by,

$$\nabla \cdot \mathbf{i}_{\mathrm{e,C}} = 0 , \qquad \text{(A.9)}$$

where subscripts, p, e, cl represent proton, electron, and catalyst layer respectively and subscripts *l* and *s* represent electrolyte and solid phases respectively.

Table B.1: Parameters used in Sun *et al.*, (2005b) agglomerate cathode model

Parameter	Value	Reference
Porosity of PTL, ε_{PTL}	0.4	a
Porosity of catalyst layer, ε_{CAT}	0.1	a
Radius of agglomerate surface area, a_{agg}	1.0 [μm]	a
Conductivity of PTL, κ_s	1.0 [S/cm]	a
Catalyst layer thickness, t_{cl}	15 [μm]	a
O_2 diffusivity in Nafion (at 80°C)	8.45×10^{-10} [m^2/s]	a
Henry's constant, H	0.3125 [atm m^3/mol]	a
Thickness of electrolyte coating of each agglomerate	80 [nm]	a
Electrolyte fraction in agglomerate, ε_{agg}	0.5	a
Reference O_2 concentration, $C_{o_2}^{\mathrm{ref}}$	0.85 [mol/m^3]	a
Effective Pt surface ratio, ε_l	0.75	a
Binary diffusivities		
PD_{O_2,H_2O}	3.70×10^{-5} [atm m^2/s]	
PD_{O_2,N_2}	2.79×10^{-5} [atm m^2/s]	b
PD_{N_2,H_2O}	3.87×10^{-5} [atm m^2/s]	

a: Sun *et al.* (2005b)

b: Bird *et al.* (2002)

APPENDIX C – BLOCK UNIFORM GRIDS FOR DISCRETISATION

Block uniform grids are a set of uniform grids in the domain. This sought of grid spacing, illustrated in Figure C.1, shows a two-dimensional PEM domain that has been divided into various sub domains. Each of these domains has a uniform set of control volumes, which are defined based on the parameters affecting the dimensions of the PEM. The dimensions of the control volumes in each of these sub domains also change with the average local water content $\hat{\lambda}_{local}$ of the sub domain. Hence, during simulation, the control volumes in each of the sub domain adapt the dimensions based on the local hydration state. The principal reason for arranging this sought of grid is to investigate the anisotropy in membrane swelling by water uptake.

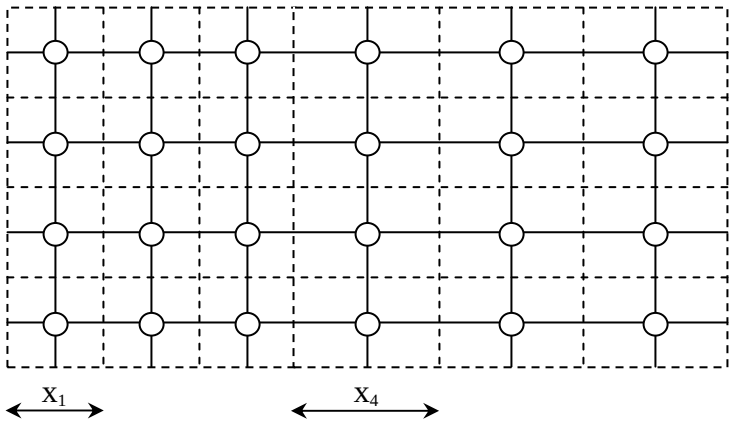

Figure C.1: Block Uniform Grid Scheme

In the case of uniform computational grids, the interfacial transport properties can be approximated with arithmetic mean of the surrounding nodes in the row. When block uniform grids are used; the interfacial properties can be computed using a

scheme given by Patankar (1980). Figure C.2 illustrates that interfacial membrane ionic conductivity κ_e between nodes *P* and *E* can be expressed as,

$$\kappa_e = f_e \kappa_P + (1 - f_e)\kappa_E \tag{3.61}$$

where

$$f_e = \frac{(\delta x)_{e+}}{(\delta x)_e}$$

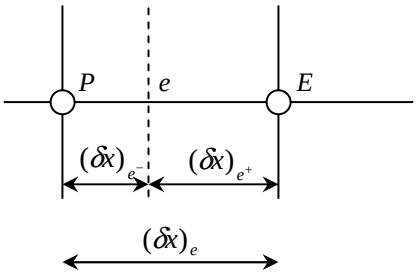

Figure C.2: Interfacial parameter approximation scheme (Patankar, 1980)

The computational framework discussed in earlier sections has been set to be grid-independent. Refining the grid sizing in the computational domain gives better illustration of the computed dependent variables and the membrane transport properties. The model can be simulated with a 2-D domain of any $n \times m$ control volumes. This can be achieved at the expense of computation times, which increase with the model grid sizing.